POLITECNICO DI TORINO
Repository ISTITUZIONALE

Molecular modelling of high-entropy alloys: from quantum to atomistic, and machine learning

Original
Molecular modelling of high-entropy alloys: from quantum to atomistic, and machine learning / Pellegrino, M., Ganjali Koli, M., Tarulli, F., Arnold, J.E., Mitrica, D., Bergamasco, L., García Fuentes, G., Piticescu, R., Gurrutxaga-Lerma, B., Fasano, M.. - In: NPJ COMPUTATIONAL MATERIALS. - ISSN 2057-3960. - ELETTRONICO. - (2026). [10.1038/s41524-026-02319-z]

Availability:
This version is available at: 11583/3017395 since: 2026-11-02T12:13:05Z

Publisher:
Springer Nature

Published
DOI:10.1038/s41524-026-02319-z

Terms of use:

This article is made available under terms and conditions as specified in the corresponding bibliographic description in the repository

Publisher copyright

(Article begins on next page)

15 November 2026

npj | computational materials

Review

Published in partnership with the Shanghai Institute of Ceramics of the Chinese Academy of Sciences

Article in Press

https://doi.org/10.1038/s41524-026-02319-z

Molecular modelling of high-entropy alloys: from quantum to atomistic, and machine learning

Check for updates

Michele Pellegrino [1,5], Mokhtar Ganjali Koli[1,5], Fabiano Tarulli [1], Joseph E. Arnold[2], Dumitru Mitrica[3], Luca Bergamasco[1], Gonzalo García Fuentes[4] ✉, Radu Piticescu[3] ✉, Beñat Gurrutxaga-Lerma [2] ✉ & Matteo Fasano [1] ✉

High-entropy alloys (HEAs), characterized by complex multielement compositions, offer broad opportunities to tune mechanical, corrosion, thermal, wetting, and functional properties, while their vast configurational space makes molecular modelling essential. This review evaluates progress across computational thermodynamics, density functional theory, atomistic simulations, and machine learning approaches, highlighting multiscale integration, methodological advances, current challenges, validation needs, and future directions for predictive HEA modelling and materials design across industrial applications and engineering practice.

High-entropy materials (HEMs) describe a materials-design paradigm in which multiple principal constituents are combined so that configurational entropy becomes an explicit lever for phase formation and functionality. Although initially articulated for metallic alloys, the concept now spans ceramics, oxides/chalcogenides, polymers, and electrode materials, where chemically complex sublattices can stabilize disordered single phases, frustrate conventional ordering, and generate locally diverse bonding environments that are advantageous for energy, electronic, and electrochemical applications[1–4]. In this broader framing, "high entropy" is not a guarantee of single-phase stability; rather, it signals that entropic, enthalpic, and kinetic contributions can be comparable and that disorder itself can be a functional feature.

Within metallic HEMs, high-entropy alloys (HEAs) emerged from the seminal 2004 studies by Yeh et al. and Cantor et al., which demonstrated that multicomponent metallic systems can form comparatively simple parent lattices (FCC/BCC/HCP) despite lacking a single dominant element[5,6]. Subsequent work established that equiatomicity is not essential: many useful compositions are non-equiatomic complex concentrated alloys that retain high mixing entropy while enabling deliberate microstructure engineering (e.g., precipitation strengthening or dual-phase architectures)[7,8]. HEAs are now being developed for structural performance in extreme environments (high temperature, cryogenic conditions, wear, irradiation, corrosion) and for functional roles where disorder-tuned surfaces and transport are beneficial (e.g., protective coatings and catalysis)[9–11].

The central advantage of HEAs is the ability to tune multiple strengthening and functional mechanisms through chemistry while often maintaining a limited set of recurring crystal structures. Even when the average lattice remains FCC or BCC, local chemical fluctuations and short-range order (SRO) can substantially modulate defect energetics (e.g., stacking-fault energy and vacancy formation), lattice friction, and scattering processes, enabling design routes that are difficult to access in dilute alloys[7,12]. The high-entropy effect, lattice distortion, sluggish diffusion, and cocktail effect remain useful as qualitative heuristics[13], but modern evidence emphasizes that the physically controlling variables are often local order, local strain, and the hierarchy of defects and interfaces created during processing.

HEAs pose an intrinsically high-dimensional design problem: phase constitution and segregation tendencies can change sharply with small composition shifts; synthesis routes often yield metastable states; and direct experimental access to thermodynamic and kinetic quantities (chemical potentials, interfacial energies, diffusion mobilities) is limited in multi-component spaces. Predictive modelling is therefore needed to screen candidate compositions, rationalize transformation pathways, connect measured properties to microscopic mechanisms, and reduce experimental iteration[14,15]. At the same time, modelling HEAs is challenging because it must represent chemical disorder (often with finite supercells or mean-field disorder treatments), incorporate finite-temperature effects (vibrational and magnetic), and remain transferable across composition space and microstructural states. These constraints are especially acute for data-driven

[1]Department of Energy, Politecnico di Torino, Torino, Italy. [2]School of Metallurgy and Materials, University of Birmingham, Birmingham, UK. [3]National Research and Development Institute for Nonferrous and Rare Metals—IMNR, Pantelimon, Romania. [4]Tecnologias de Superficies y Materiales Avanzados, Asociacion de la Industria Navarra, Pamplona, Spain. [5]These authors contributed equally: Michele Pellegrino, Mokhtar Ganjali Koli. ✉e-mail: gfuentes@ain.es; rpiticescu@imnr.ro; b.gurrutxagalerma.1@bham.ac.uk; matteo.fasano@polito.it

models and interatomic potentials, where extrapolation beyond the training domain can be difficult to detect without uncertainty-aware validation.

A useful way to organize the computational landscape is to map method families to the questions they answer. Thermodynamic frameworks, most prominently CALPHAD, enable rapid predictions of equilibrium phase fractions, chemical potentials, and driving forces, and (when coupled to mobility descriptions) diffusion-controlled kinetics; their reliability depends on assessed databases and controlled extrapolation to higher-order systems[16,17]. First-principles density functional theory (DFT) calculations, combined with statistical-mechanics methods and chemical-disorder models such as special quasirandom structures (SQS) and the coherent potential approximation (CPA), provide enthalpies, elastic constants, defect energetics, and ordering tendencies that underpin both mechanistic interpretation and database improvement[15,18]. Atomistic simulations access finite-temperature dynamics, diffusion, deformation mechanisms, and interfaces; their predictive power is tied to the fidelity and transferability of interatomic interactions, motivating the rapid growth of machine-learned interatomic potentials[19]. Mesoscale models (phase-field, kinetic Monte Carlo, crystal plasticity) translate thermodynamic and kinetic inputs into microstructure evolution and property response, and are increasingly used as the bridge between CALculation of PHAse Diagrams (CALPHAD)/atomistic and processing-scale predictions[20]. Finally, machine learning (ML) is now widely used for high-throughput screening and inverse design, but its effectiveness depends on data curation, representation of uncertainty, and robust validation against physics-based simulations and experiments[21,22].

Recent reviews have surveyed key elements of the HEA modelling ecosystem, including thermodynamic and statistical descriptions of chemically complex alloys[14,15], CALPHAD strategies and database limitations[16,17], ab initio foundations for phase stability and mechanical descriptors[18], atomistic simulation frontiers[19], and broad computational treatments of structure–property correlations and process-aware design[23,24]. This review is distinct in two ways. First, it adopts a property-driven organization that maps modelling choices to measurable quantities and simulation protocols (including transport and interfacial observables that are often treated only briefly in method-centric surveys). Second, it treats structural and functional questions on equal footing: after introducing key computational techniques, we connect them to phase stability and structure, heat transfer, wetting, mechanical response, and electronic properties, while explicitly highlighting validation, transferability, and uncertainty as the central bottlenecks for predictive HEA modelling. Ultimately, this review intends to support future work in computational HEA modelling by delineating essential tools and strategies that translate modelling insights into model-driven guidelines for experimental and engineering practice.

Computational techniques and theoretical underpinnings

This section provides an overview of computational models for HEAs. After a brief theoretical introduction, the methods are presented in ascending order of coarse-graining. We first discuss ab initio approaches, which are rooted in quantum chemistry. We then present atomistic Molecular Dynamics methods based on semi-empirical and data-driven force fields, which sacrifice explicit electronic degrees of freedom in exchange for improved time and system-size scaling capabilities. Finally, we briefly discuss Monte Carlo methods, which can be regarded either as alternatives to Molecular Dynamics or as a further level of coarse-graining. Figure 1 provides an overview of the computational models discussed in this section. We remark that a review of the intrinsic qualities of each model per se is beyond the scope of this review; instead, we restrict our discussion to their effectiveness, either demonstrated or hypothesised, in the context of HEA modelling.

High-entropy alloys thermodynamics

Thermodynamics provides the first-level rationale for why compositionally complex alloys can form relatively simple solid-solution matrices, and it also clarifies when this expectation fails. In equilibrium, phase selection is governed by minimization of the Gibbs free energy of mixing, ($\Delta G_{\mathrm{mix}} = \Delta H_{\mathrm{mix}} - T\Delta S_{\mathrm{mix}}$), so that entropic stabilization competes

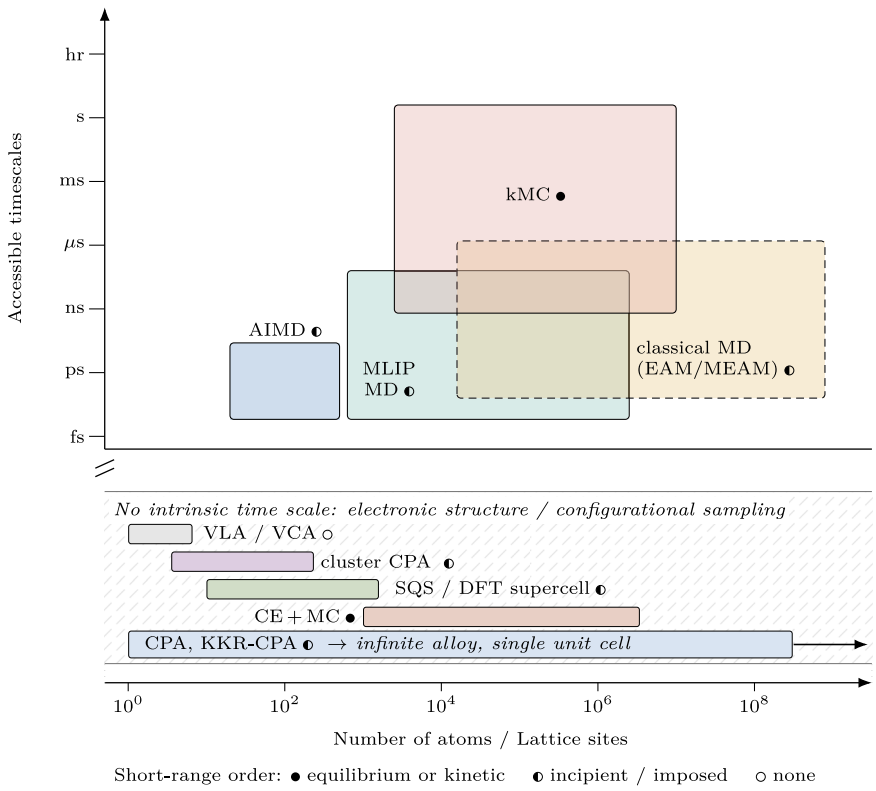


Fig. 1 | Accessible system size and timescale for methods used to model chemical disorder in HEAs. Methods that evolve a system in physical time (upper panel) are shown as size–time envelopes; those with no intrinsic time scale (lower panel, hatched) are shown by accessible size alone, the CPA extending to an arbitrarily large alloy from a single unit cell. Circles denote short-range order resolved at equilibrium or kinetically (filled), only as an incipient or imposed correlation (half-filled), or not at all (open). Envelopes are indicative and depend on chemistry, implementation and hardware. The abbreviations appearing in this figure are introduced and discussed in the "Computational techniques and theoretical underpinnings" section.

directly against enthalpic preferences for chemical ordering and compound formation. The "high-entropy effect" therefore refers to the possibility that, at sufficiently high temperature, a large configurational entropy term ($-T\Delta S_{\mathrm{mix}}$) can lower ($\Delta G_{\mathrm{mix}}$) enough to make disordered FCC/BCC/HCP solid solutions competitive with intermetallics and multiphase mixtures[25,26]. In practice, whether a given HEA forms a single phase, decomposes into multiple phases, or orders depends not only on ΔS_{mix} and ΔH_{mix} but also on additional entropy contributions (vibrational and magnetic), local chemical order, and kinetic accessibility during processing[2,7,27].

Because the "high-entropy" label is used both conceptually and operationally, it is useful to state common definitions explicitly. In the composition-based definition, HEAs typically contain five or more elements with concentrations between 5% and 35%[28]. In the entropy-based definition, HEAs are characterized by ($\Delta S_{\mathrm{mix}} > 1.5R$) (with R the gas constant), while alloys with ($1R < \Delta S_{\mathrm{mix}} \leq 1.5R$) are often termed medium-entropy alloys[29]. These thresholds are not fundamental constants; rather, they provide convenient taxonomies that reflect the role of configurational entropy in phase competition.

The standard expression for configurational (mixing) entropy follows from the probabilistic interpretation of entropy (Boltzmann–Planck)[30]:

$$\Delta S = k_B \ln (w) \tag{1}$$

where w denotes the number (or probability) of accessible microstates and k_B is Boltzmann's constant. For a random substitutional solution with n chemical species, this leads to the familiar configurational entropy,

$$\Delta S_{\mathrm{conf}} = -R \sum_{i=1}^{n} X_i \ln X_i \tag{2}$$

where X_i is the atomic fraction of element i. In the equiatomic limit $X_i = 1/n$, the expression simplifies to

$$\Delta S_{\mathrm{conf}} = -R \ln (1/n) \tag{3}$$

so that $n = 5, 6, 7$ corresponds to $1.61R$, $1.79R$, and $1.95R$, respectively. Early discussions highlighted that these values, when multiplied by temperature, yield a free-energy contribution ($-T\Delta S_{\mathrm{conf}}$) comparable in magnitude to the formation enthalpies (ΔH_f) invoked for stabilizing ordered intermetallics such as NiAl and TiAl, motivating the hypothesis that a sufficiently large entropic contribution could offset such enthalpies and instead stabilize disordered solid solutions[5].

On this basis, a variety of semi-empirical descriptors have been proposed to screen multicomponent compositions for their tendency to form solid solutions and to distinguish FCC/BCC preferences. These criteria are typically grouped into thermodynamic, Hume–Rothery, and mixed descriptors. Thermodynamic screening often imposes empirical windows for ΔS_{mix} and ΔH_{mix}; for example, ΔS_{mix} is frequently required to lie between 11 and 19.5 $\mathrm{J mol^{-1} K^{-1}}$, and ΔH_{mix} between -11.6 and 3.2 $\mathrm{kJ\ mol^{-1}}$ to favour solid solutions[31–33]. An explicit combination of entropy and enthalpy is provided by the Ω parameter introduced by Yang and Zhang[34],

$$\Omega = \frac{T_m \Delta S_{\mathrm{mix}}}{|\Delta H_{\mathrm{mix}}|} \tag{4}$$

where T_m is an average melting temperature, often approximated as $T_m = \sum_i c_i T_{mi}$, with c_i mole percent of component i. The enthalpy of mixing is commonly estimated from binary interaction enthalpies using

$$\Delta H_{\mathrm{mix}} = \sum 4 X_i X_j \Delta H_{ij}, \tag{5}$$

where ΔH_{ij} is the binary enthalpy of mixing between elements i and j. More elaborate thermodynamic screening has been proposed by Senkov and Miracle[35] following Troparevsky et al.[36], where a correlation factor k_1^{cr} relates the stability of solid solutions to enthalpic ratios,

$$k_1^{cr} \equiv 1 - \frac{T_A \Delta S_{mix}}{\Delta H_{mix}} \left(1 - \frac{\Delta S_{IM}}{\Delta S_{mix}}\right) > \frac{\Delta H_{IM}}{\Delta H_{mix}} \tag{6}$$

with ΔS_{IM} and ΔH_{IM} representing entropy and enthalpy contributions associated with intermetallic formation and T_A a characteristic temperature in the criterion.

Hume–Rothery-type descriptors quantify geometric and electronic mismatch. The atomic size difference δ[37] is commonly required to be small to promote solid-solution formation (typically $\delta < 6.6\%$ for predominant solid solutions and $\delta < 3\%$ for single-phase solid solutions[35]),

$$\delta = 100 \sqrt{\sum X_i \left(1 - \frac{r_i}{\bar{r}}\right)^2} \tag{7}$$

where r_i is the atomic radius of element i and $\bar{r}$ is the average radius. An electronegativity mismatch parameter $\Delta\chi$ is used to avoid strong chemical driving forces for ordering and compound formation[36,38,39],

$$\Delta\chi = 100 \sqrt{\sum X_i \left(1 - \frac{\chi_i}{\bar{\chi}}\right)^2} \tag{8}$$

where χ_i and $\bar{\chi}$ are the elemental and average electronegativities. Electronic structure trends are frequently summarized by the valence electron concentration (VEC), which correlates empirically with FCC/BCC preferences in many HEA families[40],

$$\mathrm{VEC} = \sum c_i \mathrm{VEC}_i \tag{9}$$

where VEC_i is the elemental valence electron concentration. Mixed descriptors combine thermodynamic and mismatch measures; for example, the geometrical parameter Λ proposed by Singh[41] normalizes mixing entropy by size mismatch,

$$\Lambda = \frac{\Delta S_{\mathrm{mix}}}{\delta^2} \tag{10}$$

and is used with empirical thresholds to favour single-phase solid solutions.

These screening metrics are attractive because they are inexpensive and can be evaluated at scale; they have been implemented in automated tools such as HEAPS[42]. Their main limitation is that they compress a multiphysics, temperature-dependent problem into a few scalar descriptors. In particular, they do not explicitly represent chemical short-range order, vibrational and magnetic entropies, or kinetic trapping during processing, and they can therefore misclassify alloys whose stability is controlled by these effects[7,27]. As a result, semi-empirical thermodynamic screening is best viewed as a first-pass filter that should be complemented by CALPHAD, first-principles thermodynamics, and validation against experimental phase constitution and property trends.

Ab initio and density functional theory calculations for high-entropy materials

In principle, ab initio modelling of high-entropy alloys serves the same dual purpose as in the study of other crystalline systems: it provides a means to understand fundamental properties at the atomic level, and it serves as a predictive tool for guiding material design. However, unlike most crystalline systems, which are typically ordered, HEAs are characterised by significant chemical and structural disorder. Order in crystalline systems confers distinct advantages for ab initio modelling. The periodicity inherent to ordered structures allows for the use of relatively small computational cells, as the behaviour of atoms in the bulk material can be effectively extrapolated from a single unit cell or a modest supercell. This periodicity simplifies the

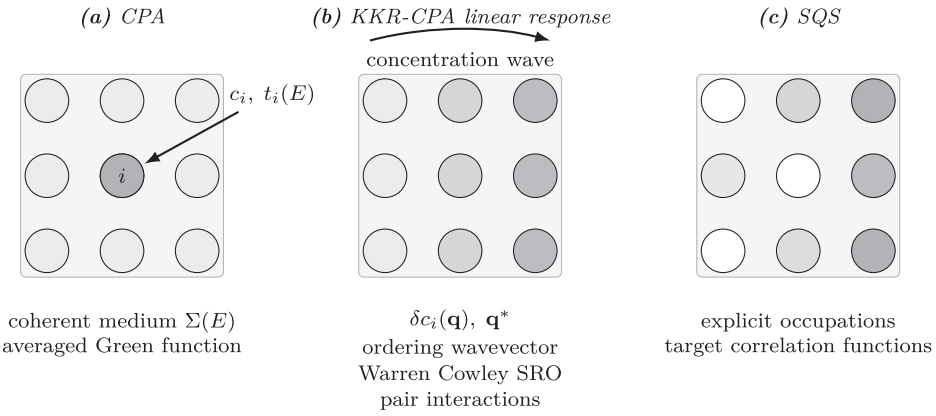


Fig. 2 | Schematic distinction between CPA, KKR-CPA and SQS. a In CPA, the chemically disordered lattice is replaced by a coherent effective medium in which a real species i, with concentration c_i and scattering matrix $t_i(E)$, is embedded self-consistently. **b** In KKR-CPA linear response, this coherent medium is perturbed by a concentration wave $\delta c_i(\mathbf{q})$, yielding the preferred ordering wavevector $\mathbf{q}^*$, Warren–Cowley SRO parameters and effective pair interactions. **c** In SQS, the alloy is represented by an explicit periodic supercell whose pair and multisite correlation functions are optimised to a random or short-range ordered target state, retaining local relaxation and chemically specific neighbourhoods at the cost of finite size and configuration selection errors.

calculation of electronic, vibrational, and mechanical properties, as well as phase stability, enabling highly efficient and precise simulations.

In contrast, the disordered nature of HEAs introduces complexity that challenges traditional ab initio approaches. The lack of periodicity means that large supercells would be required to capture the stochastic collective behaviour of atoms and to accurately represent the local variations in atomic environments. This need to sample the vast configurational space not only increases the computational cost but also complicates the extraction of meaningful averages for properties like elastic moduli, thermal conductivity, or phase stability. The interplay of these factors makes ab initio exploration of HEAs particularly demanding, necessitating innovative approaches to model their disordered atomic landscapes effectively.

Broadly speaking, three distinct techniques (represented in Fig. 2) are commonly used to tackle these challenges: (1) the Virtual Lattice Approximation (VLA); (2) the Coherent Potential Approximation; (3) Supercell methods. The salient aspects of each approach is reviewed in the next sections.

Virtual lattice approximation. The VLA is a computational strategy employed to model disordered systems within the framework of density functional theory[43]. It simplifies the problem of chemical disorder by approximating the material as an ordered structure where each atomic site is assigned an averaged or 'virtual' potential, representing a weighted mean of the constituent elements' potentials. This approach preserves the computational efficiency of periodic boundary conditions while offering a first-order approximation of the effects of chemical disorder.

The literature uses Virtual Lattice Approximation and Virtual Crystal Approximation (VCA) with different degrees of strictness. In the strict VCA, each disordered site is replaced by a fictitious atom whose pseudopotential, scattering potential or on site parameter is obtained by concentration averaging over the constituent elements[44–46]. In the broader VLA usage adopted in this review, the same idea is applied at the level of an averaged lattice or averaged effective potential, without requiring the construction of an explicit virtual pseudo atom. Both descriptions remove the site occupation variable before the electronic problem is solved. In general, averaged potential schemes can be useful for smooth trends in lattice parameter, cohesive energy or bulk modulus when the constituent elements are chemically and size similar, but they cannot describe charge transfer, local relaxation, magnetic moment distributions, defect neighbourhoods or chemical short-range order. In the hierarchy used below, VLA should therefore be read as a low cost reference medium, not as a quantitative description of observables controlled by the local environment.

Consider an alloy with N constituent elements, each with atomic fraction c_i, $i = 1, \ldots, N$. In the VLA, the potential $V_{\mathrm{VLA}}(\mathbf{r})$ at a given lattice site is defined as the weighted average of the potentials of the constituent elements:

$$V_{\mathrm{VLA}}(\mathbf{r}) = \sum_{i=1}^{N} c_i V_i(\mathbf{r}) \tag{11}$$

where $V_i(\mathbf{r})$ is the effective potential of element i. This averaging assumes that the contributions of different atomic species to the electronic structure are linearly additive, neglecting local environmental effects such as charge transfer and atomic size mismatch, which in HEAs can be considerable. As we discuss below, this is a fundamental limitation of the approach.

Having defined the VLA potential $V_{\mathrm{VLA}}(\mathbf{r})$ as above, the VLA requires solving the Kohn–Sham equations in DFT for a system under it:

$$\left[-\frac{\hbar^2}{2m}\nabla^2 + V_{\mathrm{VLA}}(\mathbf{r}) + V_{\mathrm{H}}(\mathbf{r}) + V_{\mathrm{XC}}(\mathbf{r})\right]\psi_{n\mathbf{k}}(\mathbf{r}) = \epsilon_{n\mathbf{k}}\psi_{n\mathbf{k}}(\mathbf{r}), \tag{12}$$

where $V_{\mathrm{H}}(\mathbf{r})$ is the Hartree potential, $V_{\mathrm{XC}}(\mathbf{r})$ the exchange-correlation potential, $\psi_{n\mathbf{k}}$ and $\epsilon_{n\mathbf{k}}$ are the Kohn–Sham orbitals and their eigenenergies with $\rho(\mathbf{r}) = \sum_i^N |\psi_i(\mathbf{r})|^2$ the electron density, and $V_{\mathrm{VLA}}(\mathbf{r})$ the external potential due to nuclei and applied fields.

Solving the Kohn–Sham equations under $V_{\mathrm{VLA}}(\mathbf{r})$ enables the system be treated as if it was perfectly ordered, allowing for computationally efficient calculations with small supercells. This however comes at the cost of neglecting the local atomic environments, as the averaging process ignores the stochastic nature of local atomic arrangements, which can significantly affect electronic and mechanical properties. Likewise, the VLA is unable to capture lattice distortion, which in HEAs can be significant, and it leads to an oversimplified electronic structure in which subtle effects such as charge transfer, hybridisation, and local magnetic moments are averaged out, potentially leading to inaccuracies in predicting properties sensitive to these features; given that HEAs are often made of magnetic elements, this is likewise a considerable limitation to the approach.

Despite its limitations, the VLA provides valuable first-order insights, particularly for properties that are less sensitive to local disorder, such as bulk modulus and approximate phase stability. Indeed, many examples have shown that the VLA can be used to study alloys composed of refractory elements[47–50], thermodynamic properties[50,51], as well as for some fundamental elastic properties of specific non-magnetic systems[52,53]. In such systems, it can reproduce trends in equilibrium lattice parameters and elastic constants with modest computational cost. The method performs significantly less well when the constituent elements exhibit large differences in atomic radius or electronic character. Under those conditions the neglect of local chemical environments and lattice distortion leads to appreciable errors, and more explicit treatments of configurational disorder are generally required[54].

Coherent potential approximation. The CPA is a mean-field method used to model disorder in materials; it was originally proposed by Soven in 1967 to model the electronic structure of random alloys, thereby anticipating the discovery of high-entropy alloys by decades[55]. The CPA arises to address the fact that the random distribution of atoms in a disordered alloy induces local variations in the interatomic energy landscape, resulting in significant electronic scattering effects. It addresses this complexity by substituting the disordered lattice with an effective medium. This effective medium is self-consistently constructed to capture the average scattering behaviour of the system, enabling the modelling of electronic properties without the need to explicitly consider each individual atomic configuration. Thus, the CPA determines an average medium that ensures the scattering matrix for any constituent atom embedded in the medium averages to zero. This is achieved through self-consistent solutions of the electronic Green's function.

In its stand-alone form, the CPA is used to compute the electronic structure of disordered alloys through the Green's function formalism. The coherent Green's function $G_c(E)$ is defined as

$$G_c(E) = \left[E - H_0 - \Sigma(E)\right]^{-1}, \tag{13}$$

where E is the energy, H_0 is the Hamiltonian of the underlying periodic lattice, and $\Sigma(E)$ is the coherent self energy. In stand-alone implementations, $G_c(E)$ is typically evaluated using a simplified Hamiltonian, for example within a free-electron or tight-binding description of a fixed periodic lattice, without explicit lattice relaxation.

Given an initial guess for $\Sigma(E)$, the impurity Green's function associated with species i embedded in the coherent medium is obtained from the Dyson equation

$$G_i(E) = G_c(E) + G_c(E)\left[V_i - \Sigma(E)\right]G_i(E), \tag{14}$$

where V_i is the single-site potential for species i. The CPA condition requires that the coherent Green's function equal the configurational average,

$$G_c(E) = \sum_{i=1}^{N} c_i\, G_i(E), \tag{15}$$

or equivalently that the configurationally averaged excess scattering vanish,

$$\sum_{i=1}^{N} c_i\, t_i(E) = 0, \tag{16}$$

with

$$t_i(E) = \left[V_i - \Sigma(E)\right]\left[1 - G_c(E)\left(V_i - \Sigma(E)\right)\right]^{-1}. \tag{17}$$

Here c_i is the concentration of species i, $t_i(E)$ is the excess single-site scattering matrix of species i relative to the coherent medium, and $G_c(E)$ is the Green's function of the coherent effective medium. Self-consistency is attained when the above CPA condition is satisfied.

The stand-alone form of the CPA is computationally efficient due to its simplicity, making it suitable for first-order studies of the density of states and scattering effects in disordered alloys. However, its accuracy is inherently limited by its mean-field nature, which assumes a completely random distribution of atomic species. This assumption disregards SRO—the propensity for certain atomic arrangements to occur more frequently due to local bonding preferences or thermodynamic influences. Consequently, the CPA fails to capture fluctuations in the local atomic environment, resulting in notable inaccuracies when predicting physical properties in systems where SRO significantly impacts electronic, mechanical, or magnetic behaviours. This lack of consideration for SRO also means that the CPA cannot capture local lattice distortions caused by differences in atomic sizes or bonding strengths. Consequently, it poorly represents properties that depend on these distortions, including elastic moduli, phonon dispersion, and defect energetics. The oversimplification arises from the CPA's reliance on linear additivity of scattering potentials, which inadequately models electronic interactions in systems with strong hybridisation, such as d-band metals or complex oxides. Additionally, while the CPA can, in principle, handle magnetic disorder, stand-alone implementations often lack explicit treatment of key phenomena such as spin-orbit coupling, spin fluctuations, and magnetic exchange interactions. Without such extensions, the CPA is typically insufficient for studying magnetic properties in alloys containing elements like Fe, Co, or Ni, where magnetism plays a central role in determining material behaviour.

The fact that the effective medium in the CPA is determined self-consistently from the average scattering properties of the disordered system allows the method to be combined naturally with the Korringa-Kohn-Rostoker (KKR) formalism, which provides a more rigorous multiple-scattering representation of the Green's function. In the KKR-CPA approach, the electronic Green's function $G(\mathbf{r}, \mathbf{r}', E)$ satisfies

$$[E - H]G(\mathbf{r}, \mathbf{r}', E) = \delta(\mathbf{r} - \mathbf{r}'), \tag{18}$$

where H is the Hamiltonian of the system. Within KKR, multiple scattering between sites is described by the scattering path operator

$$\boldsymbol{\tau}(E) = \left[\mathbf{t}(E)^{-1} - \mathbf{G}^0(E)\right]^{-1}, \tag{19}$$

where $\mathbf{t}(E)$ is the site-space matrix of single-site scattering matrices and $\mathbf{G}^0(E)$ is the matrix of KKR structure constants describing propagation between lattice sites. For periodic systems, one may schematically write the corresponding Bloch-resolved Green's function as

$$G(\mathbf{k}, E) = \left[E - H_0(\mathbf{k}) - \Sigma(E)\right]^{-1}, \tag{20}$$

where $H_0(\mathbf{k})$ is the Hamiltonian of the underlying periodic lattice and $\Sigma(E)$ is the coherent self energy. The Hamiltonian is typically defined based on spherical muffin-tin potentials[56] $V_{\mathrm{MT}}(\mathbf{r})$, defined as

$$V_{\mathrm{MT}}(\mathbf{r}) = \begin{cases} V_T(r), & r \le R_{\mathrm{MT}}, \\ V_{\mathrm{interstitial}}, & r > R_{\mathrm{MT}}, \end{cases} \tag{21}$$

where R_{MT} is the muffin-tin radius, $V_{\mathrm{interstitial}}$ is a constant interstitial potential, and $V_T(r)$ is a spherically symmetric potential inside the muffin-tin sphere. The corresponding Hamiltonian is

$$H = -\frac{\hbar^2}{2m}\nabla^2 + V_{\mathrm{MT}}(\mathbf{r}), \tag{22}$$

and the wavefunction may be written in multiple-scattering form as

$$\psi(\mathbf{r}) = \psi_{\mathrm{inc}}(\mathbf{r}) + \sum_j t_j^{\mathrm{site}}(E)\, G_0(\mathbf{r}, \mathbf{R}_j; E)\, \psi_j(\mathbf{r}), \tag{23}$$

where $\psi_{\mathrm{inc}}(\mathbf{r})$ is the incident wavefunction, $t_j^{\mathrm{site}}(E)$ is the single-site scattering matrix for the atom at site $\mathbf{R}_j$, and $G_0(\mathbf{r}, \mathbf{R}_j; E)$ is the free-space Green's function describing propagation between sites. Thus, the Hamiltonian defined by the muffin-tin potential underpins the scattering matrices t_j, which describe how electrons scatter from individual atomic sites. The muffin-tin approximation is highly efficient and accurate for metals and alloys, making it ideal for the multiple scattering formalism underpinning KKR. For systems with significant non-spherical features (e.g., ionic or covalent crystals), full-potential approaches may be required to improve accuracy.

With this account of the Green's function, the KKR-CPA approach proceeds analogously to the stand-alone CPA, but now incorporates multiple scattering between lattice sites explicitly through $\boldsymbol{\tau}(E)$. The coherent self energy $\Sigma(E)$ determines the effective medium, while the corresponding single-site scattering matrices enter the multiple-scattering construction of

the Green's function. In this way, the electronic structure reflects both the average disorder treated by the CPA and the intersite propagation described by KKR. This also allows a natural extension to spin-polarised Green's functions, making the method well suited to the study of magnetic alloys.

Finally, the CPA, and in particular its KKR-CPA implementation, can be combined with density functional theory to treat substitutional disorder within an ab initio framework. In this setting, one does not insert the coherent self energy as an additional local term in the Kohn–Sham equation. Rather, the DFT effective potential for each alloy component is used to construct the corresponding single-site scattering matrices, and chemical disorder enters through the CPA self-consistency condition imposed on the configurationally averaged Green's function[55–58].

The DFT effective potential retains its usual form,

$$V_{\mathrm{eff}}(\mathbf{r}) = V_{\mathrm{ext}}(\mathbf{r}) + V_{\mathrm{H}}(\mathbf{r}) + V_{\mathrm{XC}}(\mathbf{r}), \tag{24}$$

and defines the single-site scattering problem for each species occupying a given lattice site. In the Green's function formulation,

$$G(E) = \left[E - H_{\mathrm{eff}}\right]^{-1}, \tag{25}$$

where H_{eff} is the effective Hamiltonian constructed from $V_{\mathrm{eff}}(\mathbf{r})$.

For a substitutionally disordered alloy, the CPA replaces the true random medium by a coherent effective medium whose Green's function $G_c(E)$ is determined self-consistently. For each atomic species i, the impurity Green's function associated with embedding that species into the coherent medium is

$$G_i(E) = G_c(E) + G_c(E)\left[V_i - \Sigma(E)\right]G_i(E), \tag{26}$$

and the CPA condition requires that

$$G_c(E) = \sum_{i=1}^{N} c_i\, G_i(E), \tag{27}$$

or equivalently

$$\sum_{i=1}^{N} c_i\, t_i(E) = 0, \tag{28}$$

with

$$t_i(E) = \left[V_i - \Sigma(E)\right]\left[1 - G_c(E)\left(V_i - \Sigma(E)\right)\right]^{-1}. \tag{29}$$

Chemical disorder therefore enters through the self-consistent scattering properties of the coherent medium rather than through an explicit disorder-averaged local term in the Kohn–Sham equation[55,57,58].

This formulation allows DFT calculations to treat chemically disordered alloys without constructing large explicit supercells, while retaining direct access to averaged electronic, magnetic, and transport properties. At the same time, the single-site CPA remains a mean field approximation and therefore does not capture local lattice relaxation or short-range order unless further extensions are introduced[56–58].

This limitation concerns the homogeneous single site CPA itself. A single site CPA calculation represents the random alloy through a coherent medium and contains no explicit pair or higher cluster occupation variables. The same random alloy reference state can nevertheless be used to predict incipient chemical order by linear response. In the KKR-CPA concentration wave approach, the coherent medium is perturbed by a chemical modulation and the response of the electronic free energy is evaluated. The resulting stability matrix gives the dominant ordering wavevector, the chemical species involved in the instability and the short-range order parameters of the disordered phase[59–61]. The practical workflow is therefore to solve the random alloy by KKR-CPA, compute the concentration wave response or the corresponding pair interactions, identify the likely ordering mode, and then pass the resulting Hamiltonian to Monte Carlo, nested sampling or kinetic modelling when finite temperature structures are required. This route has been applied to FCC and BCC HEAs, including Al_xCrFeCoNi, NbMoTa, NbMoTaW, VNbMoTaW, Ti_xNbMoTaW, AlTiVNb and AlTiCrMo[61–64].

Cluster generalisations address the locality of the single site approximation more directly. The nonlocal CPA and the closely related dynamical cluster approximation embed a finite cluster in the effective medium, rather than one site, and recover the single site CPA as the cluster size tends to one[65,66]. In combination with KKR DFT, these approaches introduce local environment and short-range order corrections into the electronic structure of disordered alloys from first principles[67]. A separate but related line of work replaces the arithmetic average by a typical, or geometric, average of the local spectral function. The typical medium dynamical cluster approximation uses the typical density of states as an order parameter for Anderson localisation, which an ordinary average medium cannot detect because the mean density of states may remain finite while the most probable local value collapses[68]. For lattice vibrations, this framework has been developed for mass disorder[68], combined mass and force constant disorder[69], short ranged spatial correlations[70], and multibranch phonons[71]. Although they share the 'cluster' name, this approach concerns a *cluster effective medium* and localisation methods, not a HEA thermodynamic short-range order methodology as we discuss below in relation to special quasirandom structures. They complement SQS and cluster expansion (CE) calculations by improving the treatment of nonlocal scattering, localisation and spectral transport in the thermodynamic limit, while explicit supercells remain more appropriate for relaxed defect energetics, local lattice distortion and chemically specific neighbourhoods.

The KKR-CPA-DFT approach provides access to a wide range of electronic properties, such as density of states, band structure, magnetic moments, and Fermi surface characteristics, in a manner consistent with quantum mechanical principles. This is particularly advantageous as it allows to capitalise on the spin-polarised capabilities of DFT to use the CPA to model magnetic disorder, such as spin fluctuations, and study magnetic properties in alloys containing elements like Fe, Co, or Ni which are difficult to achieve with stand-alone CPA. However, the mean-field nature of the CPA and its consequent neglect of short-range order and lattice distortions remain inherent limitations. While the embedding in DFT improves accuracy, CPA-DFT may still struggle with strongly correlated systems and properties influenced by local environmental effects. These limitations highlight the need for complementary methods to fully capture the complexity of disordered materials.

The CPA approach has proved effective for computing several average structural and electronic properties of HEAs, including equilibrium lattice parameters, Wigner-Seitz radii, elastic constants, mixing enthalpies, and transport related quantities[72,73]. For the prototypical fcc NiCoFeCr alloy, single-site CPA calculations have been shown to give equilibrium Wigner-Seitz radii and elastic properties that are broadly consistent with much more expensive supercell calculations; for $CuNiCoFeCrTi_x$ ($x = 0.0$–$0.5,\ 1.0$) and NiCoFeCrTi alloys, CPA-based calculations reproduce experimental trends in Wigner-Seitz radius rather well, whereas the agreement for elastic properties is more mixed, with a tendency to overestimate the Young modulus in some compositions[74]. These results indicate that CPA is often reliable for averaged equilibrium structural descriptors, but can be less robust for mechanical observables that remain sensitive to local chemical environment and lattice distortion[72,73].

A particularly important development has been the use of KKR-CPA-based workflows to access phase stability and chemical ordering in multi-component alloys at modest computational cost. Within this framework one can compute the electronic density of states, equilibrium lattice parameters, chemical short-range order parameters, and temperature dependent thermodynamic quantities such as heat capacity, so that incipient ordering and phase transformations can be inferred from anomalies in the heat capacity together with the evolution of short-range order. This strategy has been applied across a broad range of binary, ternary, and higher order

HEAs, including NiCo, NiFe, NiCoCr, NiCoMn, NiCoMnCr, NiCoFeCr, AlTiVNb, CrCoNi, CrFeCoNi, CrMnFeCoNi, NbMoTa, NbMoTaW, VNbMoTaW, and Al_xCrFeCoNi[61,62,75–77]. Related KKR-CPA calculations have also been used to generate first-principles training data for machine learned interatomic potentials in chemically disordered alloys, including Fe_7Cr_2Ni[78].

Supercell-based approaches and the special quasirandom structures. Unlike methods like the VLA and the CPA, which treat disorder in a mean-field manner, SQS and other supercell-based approaches provide a real-space representation of disorder. These methods are widely used for their ability to capture local atomic configurations, SRO, and their effects on material properties, but come at considerably heightened computational cost.

In supercell-based methods, one constructs a large periodic unit cell ('supercell') containing a sufficiently large number of atomic sites. These sites are then randomly populated by the constituent elements according to the HEA's specified compositions. The resulting supercell is used as the fundamental unit for subsequent DFT computations. This approach relies on the ergodic hypothesis: that a sufficiently large snapshot of a random alloy configuration can statistically represent the ensemble average of the alloy's properties. Once a suitable supercell is chosen, DFT calculations can be carried out to obtain ground-state properties such as total energies, equilibrium volumes, and elastic constants, as well as response properties like phonon spectra, electronic densities of states, diffusion barriers, etc., or thermodynamic quantities such as formation enthalpies or free energies. By averaging these results over multiple random or specially designed configurations, one approximates the true properties of the HEA.

In practice, this poses several challenges, as the number of distinct supercells afforded by N distinct atomic species on a $n \times n \times n$ roughly equiatomic supercell is potentially vast, as given by Burnside's lemma[79]. For a supercell with S sites, species occupations $n_1, \ldots, n_N$ satisfying $\sum_i n_i = S$, and supercell symmetry group G, the count is

$$\mathcal{N}(n_1, \ldots, n_N; G) = \frac{1}{|G|} \sum_{g \in G} [x_1^{n_1} \cdots x_N^{n_N}] \prod_{\ell \geq 1} \left(x_1^{\ell} + \cdots + x_N^{\ell}\right)^{m_\ell(g)}, \tag{30}$$

where $m_\ell(g)$ is the number of cycles of length ℓ in the permutation of lattice sites induced by g. An estimate of the number of symmetry-inequivalent configurations may be obtained by dividing the multinomial count by the order of the supercell symmetry group, $\mathcal{N}_{\text{est}} \approx \frac{S!}{n_1! \cdots n_N! \, |G|}$, although the exact count is given by Eq. (30), since different configurations can possess different stabiliser subgroups. What this reveals is the vast configurational space of the problem of enumeration. For instance, consider a $2 \times 2 \times 2$ BCC supercell, which contains $S = 16$ lattice sites. For a five component alloy with the nearest possible equiatomic occupations $(n_1, n_2, n_3, n_4, n_5) = (3, 3, 3, 3, 4)$, the supercell symmetry group G consists of the operations of the cubic space group that map the $2 \times 2 \times 2$ supercell onto itself. Evaluating Burnside's sum for this group yields 875,875 symmetry-inequivalent occupational configurations. Thus, even for this relatively small supercell, the number of distinct arrangements that could in principle contribute to a configurational average already approaches one million. It is for this reason that practical enumeration algorithms for crystalline alloys based on this formalism have been developed in the context of cluster expansion methods[80–82].

Equation (30) shows that exhaustive enumeration rapidly ceases to be a usable thermodynamic strategy in multicomponent alloys. The count therefore serves as a workflow decision point: if the target is a random solid solution property, one constructs an SQS or a small ensemble of random supercells and checks convergence with respect to cell size and correlation functions[80,82–84]. If the target is equilibrium chemical order or configurational thermodynamics, the enumeration problem is instead compressed into a lattice Hamiltonian, which is then sampled statistically. If the target is the rate at which order, precipitation or diffusion develops, the static enumeration must be replaced by an event catalogue with kinetic rates, which leads to kinetic Monte Carlo (kMC). The Burnside calculation is thus directly connected to practical HEA modelling because it explains why representative structures, surrogate Hamiltonians and statistical sampling are required.

This vastness makes the supercell approach doubly challenging. On the one hand, the supercell must be large enough to capture the statistical nature of chemical disorder and to minimise finite-size effects: a too small cell may introduce artificial periodicity and fail to represent the true random nature of the alloy, whereas excessively large cells can be computationally prohibitive. On the other hand, the larger the supercell, the more distinct configurations that are available, so configurational averaging reliant on performing statistical sampling of multiple independent configurations can become extremely expensive unless one employs special optimisation strategies able to reduce the number of configurations needed.

The random assignment of species on lattice sites often necessitates the averaging of many configurations. SQS offers an elegant and widely used solution to this. The SQS approach, originally developed by Zunger et al.[85], aims to construct a single small supercell that replicates the most relevant pair and multisite correlation functions of an ideal random alloy.

The idea behind the SQS method is to systematically select atomic arrangements within a single supercell so that their structural correlations match, as closely as possible, those of an infinite random solution. By doing so, one can achieve a computationally tractable model that closely reproduces the average properties of the random alloy without the need for extensive configurational averaging. In practice, the construction of an SQS involves:

1. Defining target correlation functions for the random alloy, typically pair and triplet correlations at various neighbour distances.
2. Using combinatorial optimisation or heuristic algorithms (such as Monte Carlo or genetic algorithms) to identify a specific arrangement of atoms in a supercell that best matches these target correlations.
3. Once constructed, this SQS serves as a single representative configuration that mimics the random alloy's structural and electronic properties with high fidelity.

SQSs are designed to reflect the statistical nature of disorder within a significantly smaller number of atoms than would be required for brute-force sampling of random supercells. Consequently, the approach substantially reduces the computational cost associated with configurational averaging in supercell-based calculations. Density functional theory calculations performed on an SQS typically reproduce many of the averaged structural, electronic, and magnetic properties of the underlying random HEA with good accuracy, allowing physical properties to be extracted with far fewer calculations[85–91]. The SQS framework has therefore been widely employed to evaluate a range of properties of high-entropy alloys, including lattice parameters, enthalpies of formation, average magnetic moments, elastic properties, defect energetics, and tendencies toward sublattice ordering[92–94].

A conventional SQS should not be identified with an equilibrium chemically ordered state. It is constructed to reproduce the correlation functions of the ideal random alloy at a chosen composition, usually for a selected set of pair and multisite shells[85]. It is therefore well suited to random solution reference properties, including average formation energies, relaxed lattice parameters[95], elastic constants[96,97], magnetic moments, defect energetics and phonons, provided that finite size effects and configuration scatter are tested[83,85]. Finite temperature short-range order requires correlations that differ from the random limit and that depend on temperature, magnetic state and vibrational contributions. Such correlations can be imposed in deliberately ordered supercells, but they must first be generated from a thermodynamic model, such as cluster expansion plus Monte Carlo, KKR-CPA linear response plus Monte Carlo, or Monte Carlo and molecular dynamics with a validated interatomic potential[62,98,99]. A random SQS and an SRO-bearing supercell therefore concern different questions: the former represents a random reference state, the latter represents a sampled thermodynamic state. Direct comparisons between CPA and SQS, for example

in elastic calculations, are useful because they indicate when an averaged description is adequate and when explicit local environments are needed[96,97].

Comparative studies of mean-field disorder treatments and explicit supercell approaches indicate that supercell-based models generally provide a more faithful description of properties that depend strongly on local atomic environments, such as formation enthalpies, while mean-field approaches such as the CPA offer a substantial reduction in computational cost[18,36,95,100,101]. In practice, the choice between CPA-based methods and supercell-based approaches therefore depends on the available computational resources and the objectives of the calculation. CPA-based approaches are often advantageous when exploring wide compositional spaces, whereas supercell-based methods are typically preferred when detailed properties of a specific composition are required[95].

Further, it must be borne in mind that even when numerical convergence is carefully controlled, the predictive accuracy of SQS calculations based on ab initio modelling via e.g. DFT remains limited by the approximate nature of the exchange-correlation functional in DFT itself. Systematic benchmarks comparing DFT predictions with experimental thermochemistry indicate typical uncertainties in formation and decomposition energies on the order of several tens of meV per atom, which is comparable to the energy scale separating competing phases in many alloys[102–104]. Consequently, phase stability predictions based purely on DFT total energies must generally be interpreted with caution, and must often be complemented by thermodynamic modelling or experimental validation.

Finally, the supercells discussed above are static. Finite temperature dynamics can be obtained from the same electronic structure by ab initio molecular dynamics (AIMD), in which the forces driving Newtonian motion are computed on the fly from DFT at each timestep, either through the extended Lagrangian scheme of Car and Parrinello[105] or by direct Born–Oppenheimer propagation on the relaxed ground state[106,107]. Cost restricts AIMD to roughly 10^2 atoms and 100 ps[108], which excludes chemical equilibration, since reordering proceeds by diffusive rare events. Within those limits, AIMD has been used in HEAs for finite temperature free energies of CoCrFeMnNi, establishing that vibrational, electronic and magnetic entropy contribute on the same footing as the configurational term[109]; for local lattice distortion and the resulting finite-temperature resistivity[110]; and for the liquid state, where picosecond relaxation times fall inside the accessible window, yielding self-diffusion coefficients, partial pair distribution functions and SRO in melts of the Cantor alloy and its derivatives[111]. Chemical order is recovered by interleaving Monte Carlo species swaps with AIMD, which equilibrates configurations that conventional dynamics cannot reach, and which predicts *B2* ordering between mixed (Nb,Ta) and (Mo,W) sites in MoNbTaW at 300 K[112]. AIMD now serves chiefly as the reference generator for the machine-learned potentials discussed in the "Machine-Learned Force Fields" section, whose training sets often include datapoints assembled from AIMD snapshots sampled across temperature[108,113].

Cluster expansion, Monte Carlo and nested sampling. Establishing a chemically representative SRO is one of the central difficulties of atomistic HEA modelling. The methods surveyed above differ precisely in how they treat it (Fig. 1): the VLA/VCA discards it by construction, the KKR-CPA recovers only its incipient form by linear response, and an SQS represents order faithfully but must be given it, since a random SQS or a DFT-minimised supercell reproduces the random limit rather than the equilibrium state. Order that is sampled rather than imposed requires a thermodynamic model, and the cluster expansion supplies exactly this configurational-thermodynamics layer, absent from a purely SQS-based treatment: fitted to first principles energies, it is sampled by Monte Carlo to generate equilibrium SRO at a given temperature.

In a CE, the occupational energy on a fixed parent lattice is expanded in point, pair, triplet and higher cluster functions,

$$E(\sigma) = J_0 + \sum_{\alpha} m_\alpha J_\alpha \langle \Phi_\alpha(\sigma) \rangle, \tag{31}$$

where σ denotes the site occupation configuration, J_α are effective cluster interactions, m_α are cluster multiplicities and $\langle \Phi_\alpha \rangle$ are cluster correlation functions[114]. Once the interactions are fitted to first principles energies and the derivative structure enumeration is controlled by established algorithms[80,81], the energy of large numbers of configurations can be evaluated In HEAs, this CE plus sampling route has been used to compute Warren–Cowley short-range order in Mo Nb Ta V W[115], A2 to B2 order disorder transitions in MoNbTaW[116], temperature dependent configurational entropy and persistent short-range order in refractory alloys such as NbTiVZr, HfNbTaTiZr and AlHfNbTaTiZr[117], and competing ordered or segregating states by KKR-CPA-derived Hamiltonians combined with nested sampling in Al_xCrFeCoNi[62]. These workflows are now supported by widely used tools such as ATAT and `icet`[82–84].

This layer is essential for HEAs because the ideal entropy of mixing is a high temperature limiting value, not evidence that the alloy remains random at the temperatures of interest. Cluster expansion and Monte Carlo studies of refractory systems such as NbTiVZr, HfNbTaTiZr and AlHfNbTaTiZr show that configurational entropy can remain strongly temperature dependent and that appreciable short-range order may survive to very high temperature[117]. In Mo Nb Ta V W and CrCoNi, cluster expansion or on lattice machine learned Hamiltonians resolve temperature dependent correlation structures that are inaccessible to a single random SQS[98,115]. The CrCoNi case is particularly instructive because canonical Monte Carlo predicts ordering into a $Cr(Ni,Co)_2$ phase near 975 K[98]. The principal limitation is transferability: a cluster expansion is reliable only on the parent lattice, chemical space and relaxation regime represented in its training data. Energy cross validation should therefore be supplemented by property level tests, including ordering temperatures, short-range order parameters, elastic constants, defect energies and phase stability.

Nested sampling is a promising development in this regard. Originally introduced as a Bayesian evidence algorithm[118], nested sampling was adapted to atomistic configurational sampling[119], and can be used to estimate the partition function from a sequence of constrained ensembles and can thus recover thermodynamic observables over a range of temperatures[120]. The approach is useful for alloy Hamiltonians with several ordered, segregated or partially ordered basins close in free energy because it explores the energy landscape without requiring a preselected order parameter [121,122]. In HEAs, nested sampling has so far appeared mainly as an enhanced sampling option for alloy Hamiltonians rather than as a routine component of CE workflows. In Al_xCrFeCoNi, a KKR-CPA derived pair Hamiltonian was sampled to analyse competing FCC and BCC ordering tendencies[62]. More generally, the BraWl code implements nested sampling, Metropolis Hastings sampling and Wang Landau sampling for multi-component alloy Hamiltonians, including HEA applications[123].

Atomistic molecular dynamics simulations

Ab initio calculations predict energies and forces very accurately. However, AIMD techniques cannot scale past a very small number of atoms (1 ÷ 100) and very short time scales (10 ÷ 100 ps), due to their computational cost. Hence, their employment in the study of *dynamic* properties or thermo-mechanical response at finite temperature is very limited. Atomistic molecular dynamics (MD) simulations are used to bridge the gap between the atomistic description of HEAs and their macroscopic response. In MD simulation, atoms are treated as classical particles, interacting with each other via an empirical force field. This simplified description, which does not explicitly include electronic degrees of freedom, allows to extend the number of simulated atoms to the tens of thousands and the time scale to hundreds of nanoseconds (Fig. 1).

A limited number of studies have utilized classical MD simulations to investigate the bulk and interfacial properties specific to HEAs, largely drawing from well-established models for bulk pure metals and alloys. Some studies have also focused on modelling and simulating water-metal interfaces. This section provides an overview of these approaches and discusses potential extensions to HEAs.

Table 1 | Selected examples of EAM and MEAM potentials found in the scientific literature, applied to the simulation of Medium-Entropy Alloys (MEAs) and "Cantor-like" HEAs (3 elements to 5 elements)

Elements	Model	Ab-initio verification	Exp. validation	Notes	Ref.
CuFeNi	EAM	✓	✓	Defect binding energies within ±0.08 eV of DFT. Qualitative agreement with CALPHAD and experimental thermodynamics results.	364
CrFeNi	EAM	×	×	Comparison between EAM[365] and Average-Atom model. Mismatch of stacking fault energies within ~10 mJ/m^2 between the two methods.	366
CoCrNi	EAM & MEAM	×	✓	EAM underpredicts C_{11} and unstable stacking fault energy of FCC/HCP, compared to MEAM. Agreement with TEM experiments.	367
AlNiTi	MEAM	✓	✓	Comparison with DFT[368] and experiments (formation heat and bulk modulus within ~0.1 eV and ~10 GPa). Qualitative agreement with CALPHAD phase diagram.	369
CoFeNi	MEAM	×	✓	Lattice thermal conductivity and thermal expansion coefficient in the range found in the experimental literature[370,371].	372
CoFeNiTi & CrFeNiTi	EAM	×	✓	Simulation of physical vapour deposition on Ni. Agreement with X-ray diffraction on the effect of Ti on phase stability.	373
CoCrCuFeNi	EAM	×	×	"Toy model" for quinary alloy, showing lower heat of mixing compared to binary mixtures ($\Delta H \simeq 0.7$ kJ/mol) and resolving lattice stresses and distortions.	374
AlCoCrFeNi	EAM	×	✓	Calculation of lattice parameter, stacking fault and cohesive energies as a function of Al content.	375
CoCrFeMnNi	MEAM	×	✓	Lattice parameter in agreement with experiments[376]. Investigation of sluggish diffusion and micro-twining at cryogenic temperatures.	377

We report whether the studies from which the potentials are taken include numerical validation against ab initio methods and experimental validation.

Embedded atom models. One of the most successful force fields for metals and metal alloys is the Embedded Atom Model (EAM)[124] by Daw and Baskes. The modelling effort that led to EAM stemmed from the phenomenological observation that mechanical properties of metals cannot emerge from a simple pair interaction potential, hence requiring a potential that captures many-body interactions. The form of the potential is inspired by the physics of metals and bears similarities with DFT. Essentially, the per-atom energy of the metal is obtained by combining two terms, one embedding the atom into the local electron density provided by the remaining atoms of the system, and one describing electrostatic pair interactions with neighbours:

$$E_i^{\mathrm{EAM}} = F(\bar{\rho}_i) + \frac{1}{2}\sum_{i\neq j}\phi(r_{ij})\,, \tag{32}$$

where $\bar{\rho}_i$ is the sum over the spherically-averaged atomic electron densities of the atoms neighbouring atom i (originally first nearest-neighbours only), F is an embedding energy functional and ϕ is a pair interaction potential depending on the distance r_{ij} between atom i and atom j. The derivation of the potential and examples of application can be found in the review by Daw, Foiles and Baskes[125].

The original formulation of EAM works best for the metals with completely empty or filled d bands, and it has been refined and extended to incorporate a wider chemical space. Finnis and Sinclair specified a particular embedding energy function, based on the second-order approximation of tight-binding theory, which simplified the form of the potential at the cost of becoming less flexible[126]. Baskes observed that the overlap of spherically-averaged electron densities did not accurately captured the directionality of chemical bonds in covalent solids. A more refined model was proposed by including an angle-dependent term in the host electron density, thus obtaining the so-called Modified Embedded Atom Model (MEAM). MEAM has shown to accurately reproduce the bulk, surface and defects energetics of silicon[127,128]. MEAM was further extended by Lee et al. to partially include second nearest-neighbour interactions (in addition to the first nearest-neighbours), the so-called "2NN MEAM". Including second nearest-neighbours provided better phase stability and interface structure of BCC metals such as iron[129], and improved the descriptions of surface relaxations, point defects, thermal expansion and amorphous structure of pure germanium and metal-silicon/germanium systems[130].

Since their birth, EAM force fields have proved capable of describing multicomponent systems, such as binary alloys or intermetallics. Foiles et al. determined the coefficients of a multicomponent EAM by fitting the heats of solution of the binary alloys of Cu, Ag, Au, Ni, Pd and Pt[131]. Johnson proposed a form for the pair potential (ϕ in Eq. (32)) which is invariant under linear transformation of the electron density in monoatomic models and is parameter-free, allowing the formulation of an EAM potential for virtually any pair of metals[57]. Table 1 lists selected examples of metal alloys, up to 5 elements, modelled by EAM or MEAM.

Bond order and reactive potentials. Nonmetallic elements can be introduced into HEAs to improve their thermomechanical properties. Typically, elements such as nitrogen, carbon, or boron alter the crystal structure of the base alloy. For example, HCP and BCC alloys may transform into a NaCl-type FCC structure, in which metal and nonmetal atoms alternate in an ordered arrangement. Nitrides[132,133], carbides[8], borides[134], and graphene-enhanced medium- and high-entropy alloys[135] have been characterized experimentally. Atomistic models for such materials require interaction potentials capable of describing covalent bonds in solids. In some cases, a simple solution consists in adding a non-bonded angle term that accounts for the directionality of covalent bonds. The MEAM potentials discussed in the "Embedded Atom Models" section have been used to simulate oxides, carbides and nitrates[136–138]. Other angle-dependent potentials, like the Stillinger-Weber potential[139] or the Vashishta potential[140], can be used to model solids with covalent bonds, such as silica[141]. These potentials however do not include any description

of the valency of covalent bonds and its dependence on the chemical environment. Furthermore, they are not capable of modelling the dynamics of electric charges and the formation or breakage of bonds.

Bond Order potentials incorporate an approximation for the effect of the local local environment on the coordination of atomic bonds. The general expression for the per-atom energy is:

$$E_i^{\mathrm{BO}} = \frac{1}{2}\sum_{i\neq j}\left[V_R(r_{ij}) + bV_A(r_{ij})\right], \tag{33}$$

where V_R and V_A are respectively a repulsive and an attractive potential, possibly dependent on the local electronic density; b is the bond order parameter, controlling the strength of the covalent bond, i.e. scales with the valency of the bond. The bond order parameter depends on the number of nearest neighbours Z. For instance, Abell derived an empirical relation of the form $b \sim Z^{-1/2}$ [142], consistently with the idea that bond strength should decrease with the number of nearest neighbours. Important examples of bond order potentials are the Tersoff potential[143] and the AIREBO potential[144].

While providing a way to describe valency, bond order potentials do not describe systems which are undergoing bonding changes accurately. For example, they cannot capture changes in atomic charges in response to the local environment. *Reactive* potentials such as ReaxFF[145] and COMB[146] incorporate these additional complexities in the potential form. For example, per-atom bonding energy of COMB reads:

$$E_i^{\mathrm{RP}} = \frac{1}{2}\sum_{i\neq j}\left[V_R(r_{ij}, q_i, q_j) + \overline{b}V_A(r_{ij}, q_i, q_j)\right], \tag{34}$$

where the attractive and repulsive energies depend on the atomic charges q, and $\overline{b}$ is a sum of bond-order terms reflecting the different aspects of a bond, including multibody contributions (e.g. angles, dihedrals). A self energy term reflecting the change in atomic energy with the dynamic change in the atomic charge is included to produce a self-consistent set of charges. While reactive force fields achieve great flexibility, it is important to stress that they are also significantly more expensive to evaluate compared to more 'static' potentials such as (M)EAM and bond order.

Bond order and reactive potential have been combined with EAM to simulate heterogeneous systems[147,148]. Typically, the interactions between metals and covalent solids are described with a tuned Lennard-Jones potential; this choice is sometimes motivated by the relative weakness of these interactions with respect to metal-metal or covalent-covalent ones. To the best of the authors' knowledge, there exist only few attempts to parametrize reactive potential for metals with the aim of describing heterogeneous systems in the same framework[149,150]. Finding good atomistic models for the interactions between HEAs and carbon, silicon, nitrogen and oxygen, either as dispersed atoms or substrates, is therefore still a mostly open scientific question. In this regard, Neural Network Potentials discussed in the "Machine-Learned Force Fields" section may represent a viable line of attack.

Potentials for metal-liquid interfaces. Understanding the physics of liquid-metal interfaces is of primary interest for many industrial applications, such as corrosion prevention, lubrication, catalysis, electrochemistry, surface cleaning and heat transfer[151–153]. HEAs represent new target materials for the coating industry, and thus accurate molecular models for the interactions between HEA substrates and polar or non-polar liquids is desirable. Modelling interfaces between liquid metals and solid metals is relatively easy owing to the availability of liquid-solid interaction potentials. For instance, multicomponent EAM has been used to simulate wetting of pure molten metals droplets onto solid pure metals[154,155], metal droplets onto alloy substrates[156,157], or alloy droplets onto pure metal substrates[158]. Interfaces between heterogeneous materials are much more challenging to model and simulate. We will focus specifically on interfaces between metals and water. Water is a very common liquid and it is important for life and for many industrial processes (e.g. anti-icing surfaces[159] and green H_2 production[160]). Some of the following considerations extend to other simple molecular liquids.

A common measure for the affinity of a solid surface with a liquid is the angle that a liquid droplet forms upon being deposited on the surface (equilibrium contact angle; see the "Static and dynamic wettability" section). A simple way to reproduce experimentally observed contact angles in Molecular Dynamics simulations relies on adjusting the van der Waals pair interaction parameters. This approach has been used to study wetting over heterogeneous metal surfaces[161] or film boiling[162]. Interface models that are limited to arbitrarily tuned solid-liquid van der Waals interactions may effectively reproduce some macroscopic observables, but are ultimately inconsistent with the physics of water-metal interfaces. Experiments and DFT calculations show that water adsorption on metal surfaces cannot be trivially captured by a pair potential[163]. Spohr and Heinzinger treated the water-metal interface as a dielectric discontinuity between a vacuum with embedded point charges and a homogeneous dielectric medium and solved the electrostatic boundary-value problem using the method of image charges[164]. Shortly afterwards, a new model was developed, where the dipole orientation and the chemisorption of interfacial water was biased to reproduce electronic structure calculation results[165]. This later model proved effective in simulating adsorption and electrochemistry on noble metals and on iron[166–168].

More recently, Antony et al. used the reactive COMB3 potential[169] to simulate dynamic spreading of water droplets on Pt and Cu surfaces[170]. Not only the layering and orientation of water on the metal surface was captured very accurately, but qualitative differences in the wetting behaviour of the metals were observed. Gim et al. employed a QM/MM-like approach to study the wettability and the surface diffusion of water on clean metal surfaces[171]. In their study, DFT is used to simulate the metal surface while the liquid is treated as an explicit solvent[172]. This approach captures the water-metal interactions naturally. However, it bears the computational complexity of electronic structure calculations. The combination of the accuracy of ab initio simulations with the speed of MD simulations could be achieved by a Neural-Network potentials, as discussed in the "Machine-Learned Force Fields" section. Already in 2016 Natarajan and Behler used a Neural-Network potential to study the physical-chemistry of water on Cu crystal surfaces[173]. Non-trivial results were found concerning the structural ordering of water on the surface depending on the crystal plane orientation, suggesting this method could be relevant in the study of water-metal interfaces.

Machine-learned force fields

Machine-Learned Interatomic Potentials (MLIPs) represent one of the forefront lines of research in Molecular Dynamics simulations. Instead of relying on empirical force fields, MLIPs determine the per-atom energy in a molecular system as a learnable function of the atomic position $\boldsymbol{x}_i$, atomic number Z_i, and a descriptor of the local chemical environment $\mathcal{E}_i$:

$$E_i^{\mathrm{ML}} = \mathcal{F}(\boldsymbol{x}_i, Z_i, \mathcal{E}_i), \quad i = 1, \ldots, N_{\mathrm{atoms}}. \tag{35}$$

The promise of this approach is to provide accurate energies by learning on electronic structure calculations, while keeping the description of the system atomistic (i.e. without considering electronic degrees of freedom). This section presents a brief overview of the building blocks and the variants of deep-learning potential, with a focus on Neural-Network Potentials (NNPs) used in material science and HEAs modelling. The review by Unke et al.[174] provides a more complete summary of the seminal work on ML force fields.

Depending on the underlying model, training MLIPs may necessitate an extensive amount of data acquired from electronic structure calculations. In order for the model to be able to generalize, it is important that the training dataset encompasses a vast chemical space and different thermodynamic conditions. The process of creating such datasets is computationally demanding, as it can easily require $\mathcal{O}$(100K) or even $\mathcal{O}$(1M) single-point DFT calculations. Luckily, many publicly-available dataset exist,

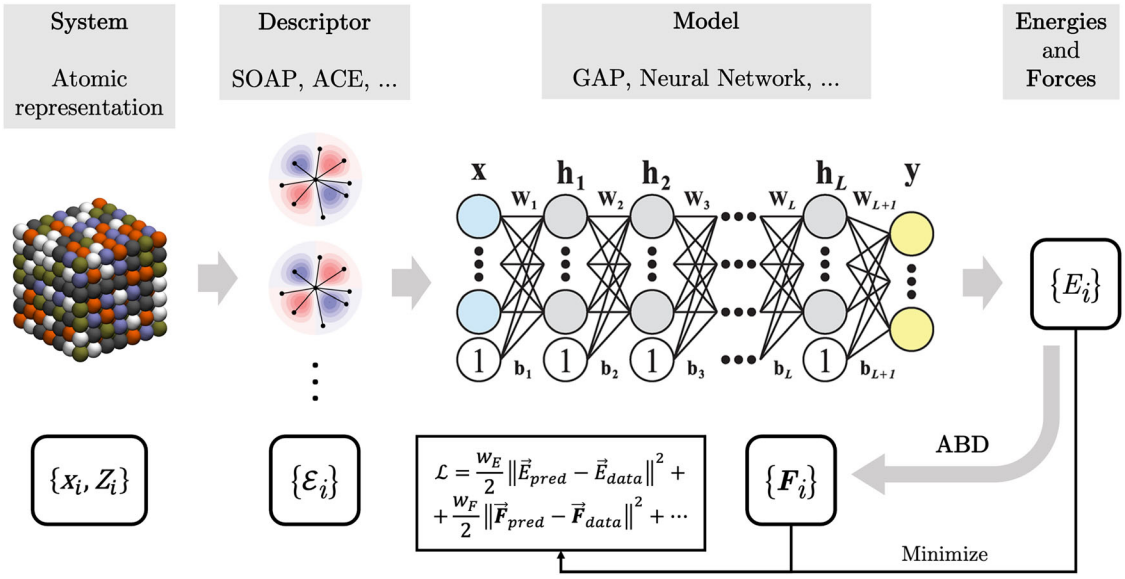


Fig. 3 | Schematic representation of a machine-learned force field. Local chemical environments are encoded by descriptors, as a function of atomic coordinates and atomic numbers. The information is then passed to a ML model (e.g. a Neural Network), which predicts energies. Forces are computed via backward differentiation (w.r.t. atomic coordinates), similarly to how gradients are computed in Physics Informed Neural Networks. Training minimizes a cost function usually defined as the quadratic error between energies or forces in the dataset and predicted ones. Figures adapted from ref. 185 (under APS reuse and permissions license) and ref. 174 (under CC-BY-NC-ND 4.0).

which can be readily utilized for model training. In the context of material science, we refer to the Material Project[175] (and in particular the MPtrj trajectory dataset[176]), JARVIS[177], NOMAD[178], QMOF[179], Open Materials[180], and Open Catalyst[181].

ML force field models comprise of two connected elements: a descriptor and an architecture. Descriptors aggregate information on the local chemical environment in which a given atom is embedded ($\mathcal{E}$ in Eq. (35)), and are introduced to facilitate the transferability of the model and eliminate rotational and permutation redundancies. From a mathematical point of view, descriptors can be viewed as a similarity metric between chemical environments. Initially, descriptors were expressed in terms of local radial and angular correlation functions[182], or bond-order parameters[183]. The Smooth Overlap of Atomic Positions (SOAP[184]) is possibly the most commonly used descriptor, owing to its accuracy and its natural interpretation. More recently, the Atomic Cluster Expansion (ACE[185]) has emerged as the most advanced and promising descriptor. ACE is a generalization of SOAP and its calculation scales linearly with the number of neighbouring atoms. In the training and evaluation of MLIPs, descriptors are computed for each atom in the system and passed to a model that predicts per-atom energies. It is also worth highlighting that descriptors are instrumental in making the input to the ML model invariant or equivariant under specific transformations of the frame of reference.

The types of model architecture ultimately determine the efficiency and expressiveness of the force field. Kernel-based methods used for MLIPs, such as Gaussian Approximation Potentials (GAP[186–188]), are very predictive on small datasets, but are not very data-efficient and thus difficult to scale to larger chemical spaces. NNPs scale more easily to large datasets and are more expressive than kernel methods[182], but generally inferior in accurately predicting energies from small molecular datasets. Equivariant graph message-passing NNPs are able to achieve the best of the two worlds by including a non-local representation of atomic interactions in terms of connected graphs, but are more computationally expensive and challenging to parallelize[189,190]. While the output of NNPs is usually the per-atom energy, forces can be obtained by Automatic Backward Differentiation (ABD). Figure 3 depicts the typical flow of information occurring in the forward evaluation of an NNP. It is worth remarking that there are also several examples of neural networks being used to directly predict material properties, "bypassing" the calculation of an interatomic potential.

The first prominent application of MLIPs to HEAs are Low Rank Potentials (LRPs)[191,192]. In LRPs, the energy is expressed as a sum of contributions from local neighbourhood interactions. Its main strength lies in compressing the number of parameters required to describe multi-element interactions while retaining the ability to capture local chemical ordering. LRPs have been shown to achieve deviations in cohesive energies of the order of 1 meV with respect to ab initio cluster expansion calculations, while qualitatively reproducing heat capacities and local ordering in MEAs and HEAs. In a similar spirit, the Atomistic Line Graph Neural Network (ALIGNN[193]) has been trained to predict local ordering of HEAs crystals (≥4 elements, ~100 atoms) containing Cr, Mn, Fe, Co, Ni, Cu and Al (ref. 194, Fig. 4a). ALIGNN shows errors on the order of 0.1 eV on cohesive energies on out-of-distribution data even when trained on subsets of MEAs (≤3 elements) and small crystals (~20 atoms).

Another architecture that has recently attracted considerable interest for HEAs is MACE, an equivariant message-passing NNP that combines the favourable scaling properties of ACE with the accuracy and expressiveness of graph neural networks. MACE builds upon this framework by constructing efficient high-order messages that express many-body atomic interactions[195,196]. The recent commentary by Bernstein[197] briefly recollects the advancements of this potential with respect to the previously available models. MACE has been trained on 150k inorganic crystals taken from the Material Project database, and recently a multi-head version trained on the Open Material dataset has been released. The result of this extensive training, named MACE-MP0, has been proposed as a *foundation model* for material chemistry, with the ambitious goal of being able to model any atomistic system[198]. MACE-MP0 has been applied to the 20-component Cantor alloy, with the aim to test its scaling properties on a multicomponent system. MACE-MP0 is able to achieve 1 ns/day for a 10^4-atom system by distributing the work on multiple GPUs (Fig. 4b). This benchmark shows the capabilities of MACE in terms of time-to-solution, although the results have not been directly verified against *ab inito* simulations due to the system size.

As a final example of modelling approach at the intersection between Molecular Dynamics and Machine learning, we mention *alchemical compression*, which tackles the vastness of the configurational space of HEA. Essentially, alchemical compression amounts to a learnable mapping of the chemical elements to a smaller number of pseudo-elements (Fig. 4c). This

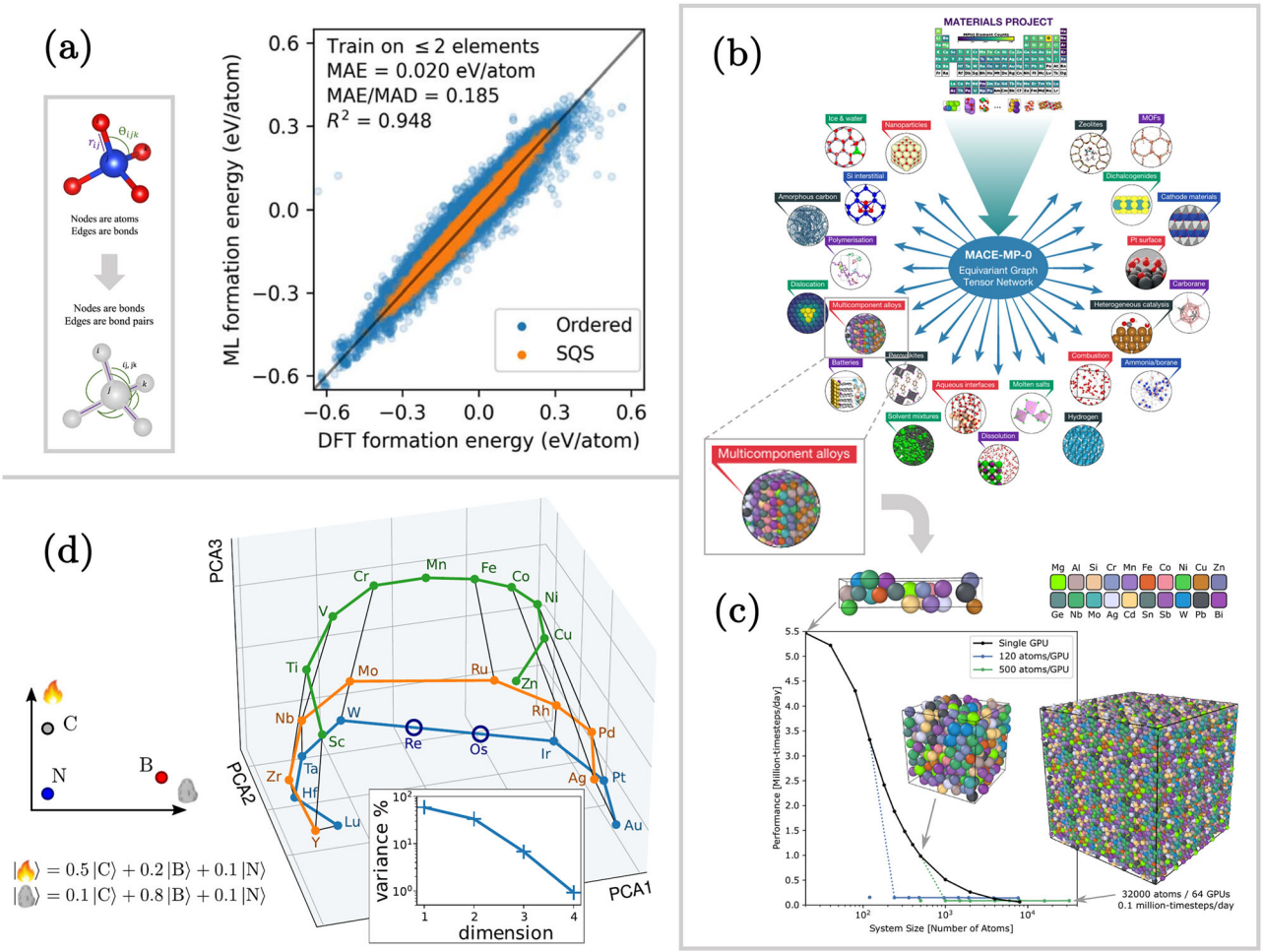


Fig. 4 | Overview of ML and NNP applications to HEAs. a Parity plot of ALIGNN predictions on the formation energy of alloys with ≥3 elements, obtained by training on binary alloys only; inset: schematic representation of the line graph architecture of ALIGNN (figures adapted from ref. 193, Creative Commons CC BY, and ref. 194, republished under STM guidelines under RSC license). **b** Modelling capabilities of the MACE-MP0 foundation model. **c** Weak-scaling curve for the simulation of a Cantor alloy with MACE on GPUs (panels b and c are adapted from ref. 198, Creative Commons Attribution CC BY 4.0). **d** Representation of the alchemical compression of three elements into two pseudo-elements and example of dimensionality reduction based on alchemical compression for some transition metals, highlighting periods, indicated by different colours, and groups, indicated by the connecting black lines (figures adapted from ref. 199, APS reuse and permissions license).

lower-dimensional representation, which can be further compressed with traditional methods such as Principal Component Analysis (PCA), has been shown to reduce the computational cost of MLIPs with negligible loss of accuracy. Alchemical compression has been used in combination with a fully-connected neural network based on three-body features to study bulk and surface properties of HEAs[199,200].

Despite their impressive capabilities, MLIPs present some important limitations. While being orders of magnitude faster than DFT calculations, deep-learning potentials still remain significantly slower than classical force field, owing to the need of evaluating a possibly very complex neural network to update energies and performing ABD to update forces. In the spirit of Quantum Mechanics/Molecular Mechanics methods, hybrid Machine Learning/Molecular Mechanics methods have been proposed, whereby only a limited part of the system is simulated with an ML or NN potential, while the rest is simulated using faster classical Molecular Dynamics[201–205]. Furthermore, deep-learning potentials do not naturally include long-range interaction, owing to the locality of descriptors. While some attempts of including electrostatics have been made[206–208], this problem remains devoid of an univocal solution, as long-range electrostatics is usually not considered in reference DFT calculations. Another challenge is represented by the vastness of the training datasets needed to ensure the potential is able to generalize. This issue has been softened by employing active learning approaches[209].

Popular Molecular Dynamics codes support the integration of NNPs. LAMMPS can run NNPs via a set of modules, mostly maintained by the community. OpenMM natively supports NNPs in its most recent versions. The support for NNPs has also been included in the 2026 release of GROMACS.

Monte Carlo methods

In this last section on computational methods, we briefly illustrate examples of Monte Carlo (MC) approaches for studying HEAs. Equilibrium canonical MC simulations are often employed, either alone or in combination with MD, to explore the configurational space of HEAs and identify free-energy minima. MC methods have also been coupled with genetic optimisation algorithms (e.g. cuckoo search) to accelerate the exploration of the chemical space of HEAs[210].

Equilibrium MC samples configurations with the correct thermodynamic weights, but does not attach a physical time to the sampled sequence. Kinetic Monte Carlo (kMC) supplies that time by assigning rates to discrete activated events, most often vacancy jumps, atom exchanges or interstitial hops[211–213]. It is therefore appropriate for slow diffusional

processes that are inaccessible to direct molecular dynamics[213], including vacancy-mediated diffusion, chemical SRO formation, ordering relaxation, precipitation, segregation and radiation driven defect evolution[214]. The central difficulty in HEAs is that migration barriers are local environment dependent. A single barrier cannot represent a vacancy jump in CrCoNi, MoNbTa or related concentrated solid solutions, since both the initial state and the saddle environment vary with local chemistry. Practical kMC workflows therefore require one of three barrier descriptions: transition state cluster expansions fitted to first principles saddle energies[215,216]; on-the-fly saddle catalogues, such as the kinetic activation relaxation technique and selective active volume kMC[217,218]; or machine learned barrier predictors trained on local chemical environments[219]. MD and kMC simulations of concentrated FCC alloys show that slow diffusion need not be attributed directly to configurational entropy[220,221]. In NiFe, NiCo and NiCoCr, preferential diffusion follows from composition dependent vacancy migration barriers and from the percolation of fast and slow diffusion pathways[221,222]. The diffusivity can therefore pass through a minimum near the site percolation threshold, rather than decreasing monotonically with the number of alloying elements[221,223]. For chemical ordering, kMC supplies the kinetic information that equilibrium Monte Carlo lacks. It has been used to follow chemical short-range order formation in FCC CrCoNi and BCC MoNbTa[224]; to show that established short-range order can reduce and localise vacancy-mediated diffusion by increasing migration barriers and backward jump correlations[225]; to map path dependent migration barrier spectra and the temperature dependence of B2 ordering in refractory NbMoTa[219]; and to show that vacancy and interstitial diffusivities in CrCoNi can be tuned by changing the degree of chemical order[226]. Whereas kMC is powerful when the event catalogue and barrier distribution are physically representative, missing events, poor saddle sampling or a barrier model trained outside its local chemistry domain will produce a precise trajectory with little predictive value.

Structure, functional properties and applications

Phase stability and structure

Phase stability is the organizing principle that links composition and processing to microstructure and, ultimately, to properties. In HEAs, the central challenge is that small changes in composition and thermal history can switch the stable (or metastable) set of phases, alter ordering tendencies, and promote segregation or topologically close-packed phases. Computational phase-stability tools therefore aim to quantify which phases are thermodynamically competitive, how their driving forces vary with temperature and composition, and how processing pathways can bias the realized microstructure.

CALPHAD as a framework for multicomponent equilibria. The CALPHAD method provides a phenomenological framework for thermodynamic and kinetic calculations by representing the Gibbs free energies of individual phases (and, when available, phase mobilities) as functions of composition, temperature, and pressure[227]. From these constitutive models, CALPHAD yields equilibrium phase fractions and compositions, phase boundaries, chemical potentials, and driving forces for transformations; when coupled to assessed mobility descriptions, it also enables diffusion-controlled precipitation, homogenization, and process-relevant heat treatment simulations. In the HEA context, this role is particularly valuable because CALPHAD offers a systematic way to compress a high-dimensional composition space into actionable predictions that can be interrogated against experiments and then iteratively refined.

A key strength of CALPHAD is that it enforces thermodynamic consistency across subsystems through physically motivated functional forms (e.g., sublattice and compound-energy models) and parameter assessment strategies, which makes extrapolation from lower-order systems toward higher-order compositions feasible[228]. This extrapolation logic is also the source of a central caveat for HEAs: multicomponent predictions are only as reliable as the assessed description of the underlying binaries and ternaries, and they remain sensitive to which higher-order interactions are included (or neglected) when data are sparse. In many HEA-relevant systems, higher-order (quaternary and beyond) interaction parameters are unavailable and early database constructions therefore rely on lower-order descriptions as a first approximation[229]. This is often sufficient to capture broad phase trends, but it can miss subtle ordering tendencies and narrow stability fields that are crucial for microstructure control.

The practical limitation for HEAs is thus not the CALPHAD formalism itself, but database coverage and validation. Interaction parameters are assessed from a mix of experimental thermochemical/phase-equilibria data and computational inputs, and the element sets and phase models included in HEA-focused databases cannot span the full chemical space of multi-principal element alloys. Widely used options include TCHEA (Thermo-Calc) and PANHEA (CompuTherm), which provide useful guidance when applied within their validated compositional and temperature ranges[230,231]. For compositions that fall outside the validated domain, CALPHAD should be interpreted as a hypothesis generator whose predictions require targeted verification, rather than as a fully predictive oracle.

Databases, validation, and high-throughput CALPHAD workflows. Since the introduction of the HEA concept, CALPHAD predictions have been increasingly benchmarked against experimentally observed phase constitutions and microstructures across a broad range of alloy families[229,232–239]. A representative example is the AlCoCrFeNi family, where database development and subsequent phase-stability analysis highlighted the importance of obtaining reliable descriptions of lower-order subsystems before trusting higher-order extrapolations[229]. In that work, higher-order interaction parameters were not introduced in the first approximation, yet CALPHAD still captured the principal composition-driven trend that the primary solidification mode changes from FCC-dominant at low Al content ($x < 0.75$) to BCC/B2-dominant at higher Al content ($x > 0.75$), consistent with experimental observations[229]. This illustrates both the utility of CALPHAD for rapid trend prediction and its sensitivity to database completeness when phase competition is tight.

Database development for HEAs has also been discussed explicitly as a methodological problem. Chen et al. outlined challenges and strategies for constructing multicomponent descriptions, including the need to reconcile scarce multicomponent experimental data with physically consistent extrapolation, and presented an early TCHEA database framework spanning 15 elements[232]. Importantly, that effort highlighted how high-throughput DFT can be used to augment missing thermochemical information (e.g., mixing enthalpies in higher-order systems) to improve parameterization and reduce ambiguity in phase stability predictions[232]. This interplay between experiment, CALPHAD optimisation, and first-principles inputs is increasingly central for HEAs, where traditional reliance on equilibrated phase-diagram measurements alone is often impractical.

Application-driven CALPHAD studies have reinforced an additional HEA-specific complication: validation is frequently confounded by metastability and processing path dependence. For example, critical assessments of CALPHAD-guided HEA design emphasize that alloys produced by conventional routes may retain metastable phase assemblages, and that long annealing treatments are often required to approach equilibrium before comparisons to CALPHAD can be meaningfully interpreted[234]. This makes it essential to report processing history alongside computed equilibrium predictions, and, where possible, to complement equilibrium calculations with kinetic simulations and microstructural characterization.

A practical bottleneck in HEA design is that "one-at-a-time" CALPHAD calculations do not match the scale of the composition space. This has motivated high-throughput CALPHAD workflows that automate phase-diagram evaluation, solidification (including Scheil-type approximations where appropriate), and precipitation calculations through scripting and Python-based interfaces. CAROUSEL, for instance, provides

an open-access, GUI-assisted high-throughput interface to MatCalc and supports solidification and solid-state precipitation screening[235]. High-throughput pipelines can then be coupled to application-relevant filters. In ref. 236, for example, CALPHAD-based high-throughput solidification calculations were used to process 11,235 compositions in the CrCoNiAlTi system under prescribed boundary conditions and to down-select candidates forming targeted FCC+L12 microstructures; the study further linked thermodynamic screening to simplified strength models (solid-solution and precipitation contributions) and reported agreement with experimental trials[236]. Similarly, eutectic HEAs—attractive for casting and energy-efficient processing because of reduced melting temperatures—have been explored through high-throughput CALPHAD frameworks, with predicted eutectic-forming domains showing strong correspondence with experiments[237]. These examples illustrate a general pattern: CALPHAD is most impactful when used not merely to compute phase fractions, but to define design constraints and to interface with downstream property models and synthesis routes[233].

Emerging workflows increasingly couple CALPHAD with machine learning and atomistic simulations. One motivation is to reduce the cost of supplying high-fidelity thermochemical inputs (traditionally from DFT) by using transferable machine-learned interatomic potentials together with statistically meaningful sampling of chemical disorder (e.g., SQS)[238]. Such hybrid pipelines can accelerate database refinement, enable uncertainty-aware screening, and provide a structured pathway from thermodynamic descriptors to microstructure evolution. In parallel, CALPHAD has been integrated with rapid experimental platforms for coatings and multi-component deposition, where composition libraries, modelling, and auxiliary criteria calculations are combined to establish composition–microstructure–property relationships at scale[239].

Overall, CALPHAD remains indispensable for establishing thermodynamic baselines and navigating composition space, but predictive HEA modelling increasingly depends on (i) database expansion beyond transition-metal-centric element sets, (ii) systematic incorporation of computational thermochemistry and uncertainty quantification, and (iii) tighter coupling to kinetic and microstructure models so that equilibrium predictions can be translated into process-aware guidance and experimentally testable hypotheses.

Structural stability beyond equilibrium: ordering, nucleation, and defect energetics. Equilibrium phase diagrams are necessary but not sufficient for HEAs because local chemical order and kinetic pathways can decisively affect which phases are realized and how they transform. Atomistic simulations and hybrid sampling techniques complement CALPHAD by directly probing finite-temperature stability, chemical short-range order (CSRO), nucleation conditions, and defect energetics in chemically complex matrices.

Using MD and hybrid Monte Carlo/MD (MC/MD), Salloom et al. analysed the relative stability of γ-FCC and ε-HCP in $Fe_{40}Co_{20}Cr_{15}Mn_{20}Si_5$[240]. Pure MD sampling suggested marginal HCP preference at room temperature and a large negative stacking-fault energy (SFE), whereas hybrid MC/MD sampling—which allows chemically driven rearrangements—stabilized the FCC phase and yielded a smaller (still negative) SFE. This difference was attributed to CSRO: MC/MD produced distinct 1NN CSRO signatures in FCC versus HCP that were not sampled by MD alone (Fig. 5). Such results highlight that structural stability in HEAs can depend sensitively on whether the simulation protocol can equilibrate chemical order on the relevant length scale.

Meesa et al. used MD to examine how nucleation conditions influence phase selection during cooling (solidification) in $Fe_{50}Mn_{30}Cr_{10}Co_{10}$[241]. Homogeneous nucleation produced predominantly BCC with a substantial amorphous fraction at 300 K, whereas heterogeneous nucleation with an FCC seed yielded a dual-phase FCC/HCP microstructure with reduced amorphous content (Fig. 6a). Subsequent annealing preserved the respective phase fractions, demonstrating that processing path and initial nuclei can kinetically select different metastable endpoints even at fixed composition.

Defect-related metrics such as lattice parameter trends and SFE provide an additional bridge between phase stability and mechanical response. For FeNiCrCoAl, MD-based analyses show that lattice parameters decrease with increasing Ni/Cr/Co content and increase with Al addition, reflecting atomic-size effects and providing a route to tune local strain fields (Fig. 6b, c)[242]. The same work reported systematic SFE trends with composition and demonstrated that non-equiatomic alloying can be used to engineer stacking-fault energetics (Fig. 6d), which in turn modulate deformation pathways.

Point-defect energetics provide a complementary defect metric to stacking-fault energetics. Roy et al.[243] investigated vacancy formation and migration in the refractory BCC MPEA $(Mo_{0.95}W_{0.05})_{0.85}Ta_{0.10}(TiZr)_{0.05}$ using DFT calculations on chemically disordered supercells and cNEB migration-barrier calculations. They showed that vacancy formation energies and migration barriers are strongly controlled by local chemical environments, charge-transfer-driven lattice distortion, and migration direction. In particular, the Zr-vacancy migration barrier changes from 0.48 to 1.63 eV between two local environments, while migration along $\langle 100 \rangle$ is 2–3 times more difficult than along $\frac{1}{2}\langle 111 \rangle$. This example shows that point-defect stability and vacancy-mediated diffusion in refractory MPEAs are local-environment-resolved quantities rather than simple averaged elemental descriptors.

CALPHAD remains indispensable for establishing thermodynamic baselines and screening broad composition ranges, while atomistic and data-driven approaches are increasingly required to capture CSRO, nucleation pathways, and defect energetics that govern structural stability in practice. Future progress will depend on expanding and validating multi-component databases, integrating uncertainty quantification, and strengthening couplings between CALPHAD, atomistic simulations, and mesoscale microstructure models.

Bayesian optimisation for improving CALPHAD predictions. For high-entropy and other complex concentrated alloys, CALPHAD predictions should be interpreted together with their uncertainty rather than as deterministic phase maps[244]. These systems occupy high-dimensional composition spaces where empirical limitations are sparse, extrapolation from binary and ternary assessments is common, and small differences in Gibbs-energy parameters can change predicted phase boundaries, ordering tendencies, or minor-phase fractions. Uncertainty-aware databases, therefore, associate thermodynamic parameters with probability distributions and propagate those distributions to quantities relevant to alloy selection, including phase-stability probabilities, solvus temperatures, driving forces, and equilibrium phase fractions[245].

Bayesian thermodynamic assessments provide a practical route for constructing such databases. Experimental equilibria, calorimetry, first-principles calculations, and their respective measurement or model errors can be combined through a likelihood-based calibration of Gibbs-energy parameters. The resulting posterior parameter ensemble preserves parameter correlations and enables the distinction between well-supported predictions and extrapolations. For high-entropy alloy design, this enables robust screening: candidate compositions can be ranked by the probability of meeting a phase-stability criterion across the intended processing window, rather than by a single nominal prediction[16].

It also supports targeted experimentation, since sensitivity analysis or expected information gain can identify the measurements most likely to reduce uncertainty in the composition-temperature regions that govern design decisions. This approach should complement, not replace, validation experiments—particularly where short-range order, metastable phases, magnetic effects, or kinetic limitations are important. Uncertainty-aware CALPHAD databases and Bayesian thermodynamic assessments address the combinatorial complexity and data gaps of HEAs. These frameworks use probabilistic confidence intervals for phase-equilibrium predictions, enabling advanced extrapolation into unexplored, multiprincipal-element chemical spaces[246–248].

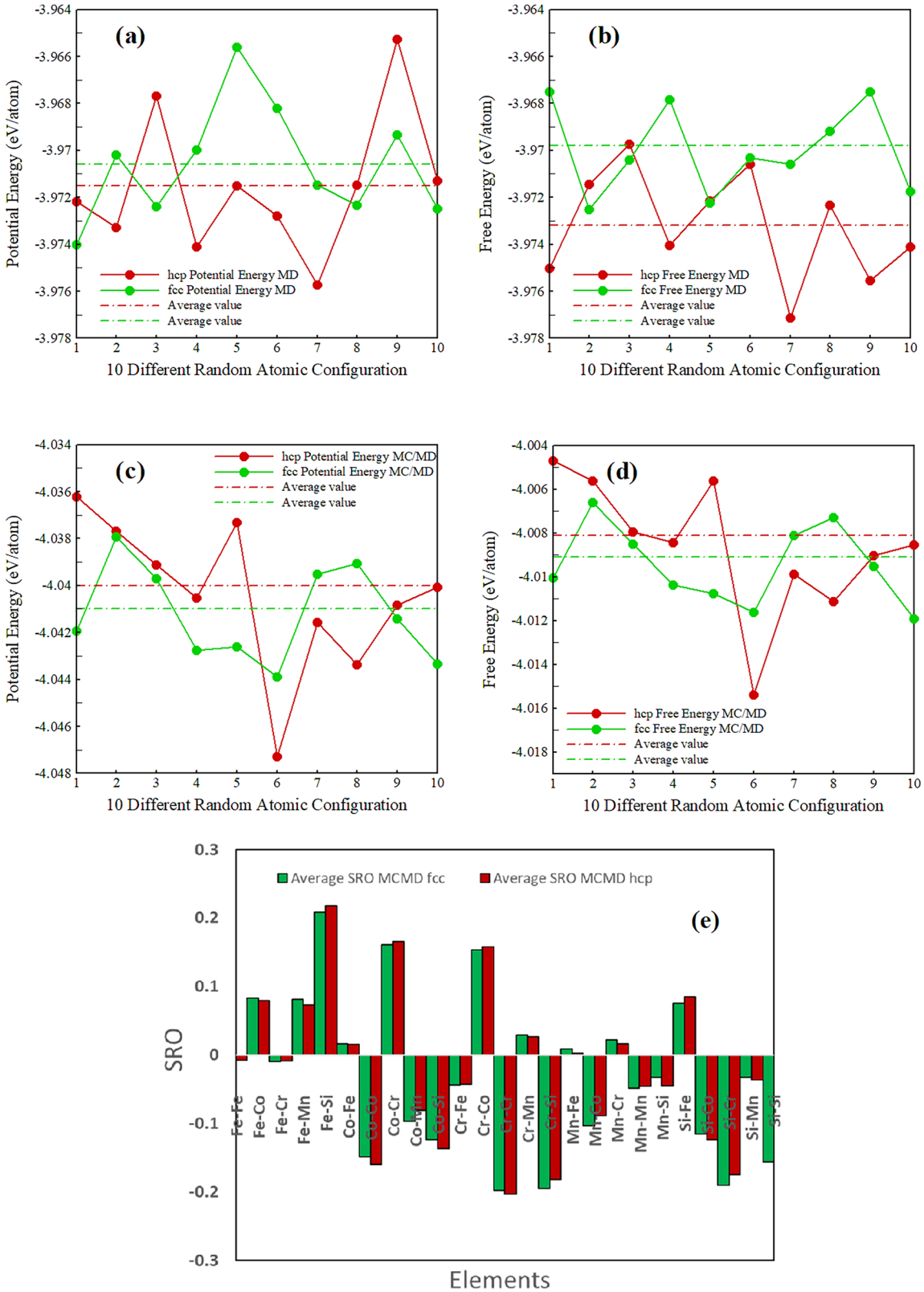


Fig. 5 | Structural stability of HEA. Potential and free energies of ten initial random configurations after MD (**a**, **b**) and MC/MD (**c**, **d**) simulations. The 1NN CSRO values obtained after MC/MD (**e**) reveal non-random, phase-dependent local chemical preferences in the FCC and HCP phases. These CSRO patterns indicate that chemical short-range order is linked to the energetic stabilization of competing crystal structures, rather than being only a structural descriptor. Panels (**a**–**d**) were redrawn using data from Figs. 3 and 5, and panel (**e**) was reproduced from Fig. 4 of ref. 240 https://doi.org/10.1088/1361-651X/ac860d. © IOP Publishing. Reproduced with permission. All rights reserved.

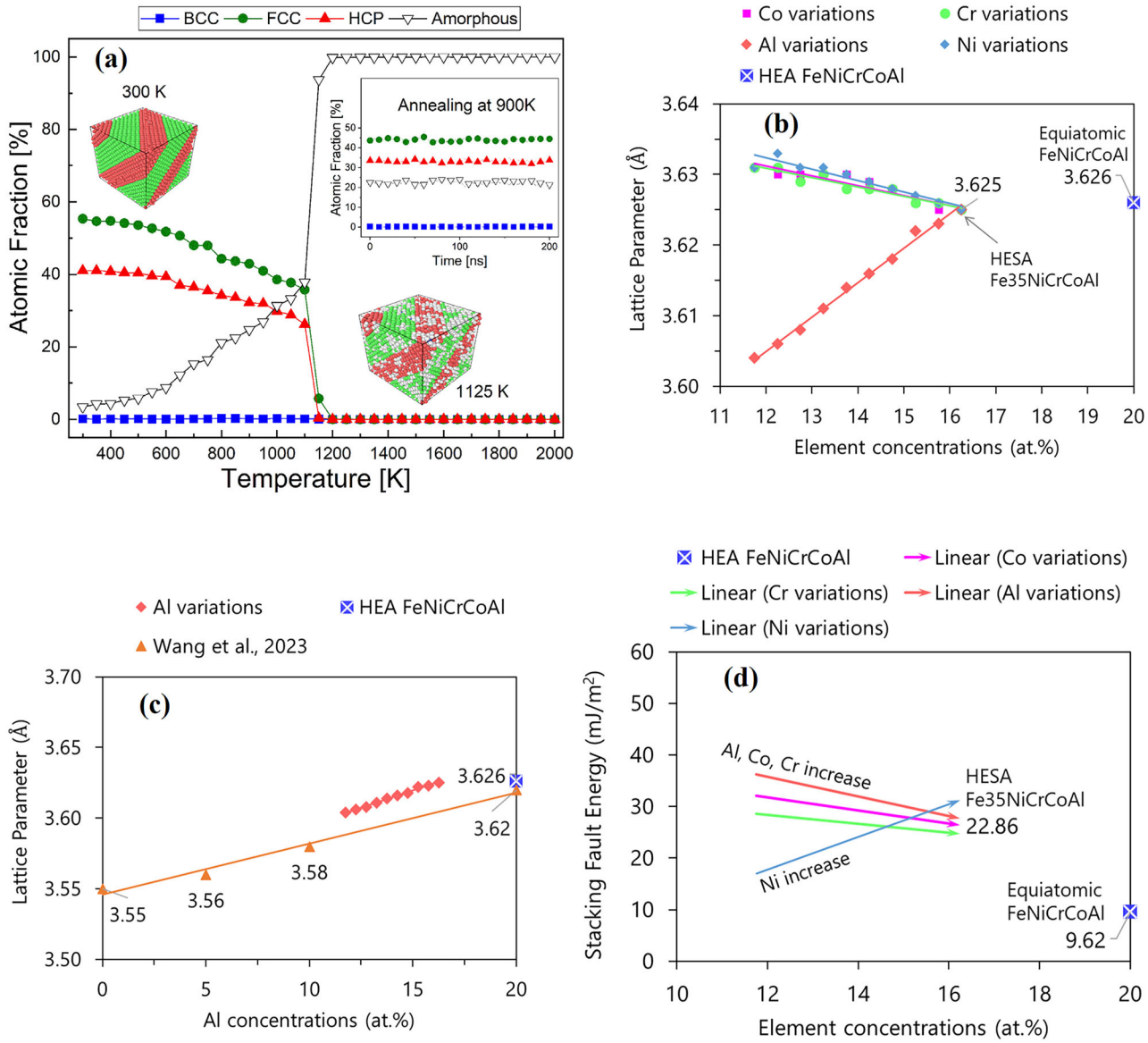


Fig. 6 | Phase evolution during cooling under heterogeneous nucleation conditions. The inset plot shows the phase fractions during annealing at 900 K. The colour of the symbols in the line plots and the colour of the atoms in the sample insets follow the legend shown in panel (**a**). The calculated lattice parameter as a function of alloying element concentration obtained from molecular dynamics simulations (**b**), with comparison to the experimental data reported by Wang et al. **c** The calculated stacking fault energy (SFE) as a function of alloying element concentration obtained from molecular dynamics simulations (**d**). Panel (**a**) reprinted from ref. 241. Panels (**b**–**d**) reprinted from ref. 242 with permission from Elsevier.

Uncertainty-aware methodologies tackle this through: ensemble modelling, building multiple thermodynamic models (e.g., combining Bayesian neural networks) to calculate the spread in possible phase equilibria[246]; configurational entropy calibration, moving beyond ideal mixing models to statistically constrain vibrational, magnetic, and short-range ordering contributions to the Gibbs free energy[249]; and commercial advancements, with dedicated HEA databases, such as Thermo-Calc's TCHEA Databases, that are continually updated with higher-order systems (e.g., TCHEA9, incorporating 27 elements).

Bayesian inference allows to quantify parameter uncertainty by treating thermodynamic model coefficients (such as Redlich-Kister interaction parameters) as probability distributions rather than fixed values[246,250,251]. Tools like ESPEI (Extensible Self-optimising Phase Equilibrium Infrastructure) utilise Bayesian parameter estimation to simultaneously fit ab initio data (e.g., Density Functional Theory) and experimental phase boundaries, generating usable uncertainty limits[250,252]. By quantifying uncertainty, one can map the vast HEA compositional space to identify the most unexplored or highly uncertain intervals. This permits the pruning of millions of candidate compositions into high-confidence targets for experimental synthesis[246,248,253]. When evaluating mechanical properties (e.g., yield strength, hardness) or microstructural stability (e.g., avoiding brittle sigma-phase formation), Bayesian optimisation balances exploitation (focusing on known-good alloys) with exploration (testing unmapped regions where the algorithm predicts high property potential)[254,255].

Bayesian Optimisation (BO) coupled with CALPHAD accelerates materials discovery by combining the predictive power of thermodynamic databases with intelligent, uncertainty-aware machine learning. This hybrid approach guides experimental synthesis and processing, drastically reducing the time and cost required to discover and optimise complex alloys by targeting specific phase equilibria[256]. Recent research uses BO approach to link processing parameters (e.g., cooling rates, heat treatments) to final microstructure states and mechanical properties[257].

Table 2 | Comprehensive comparison of Equilibrium (EMD/Green–Kubo) and Non-Equilibrium (NEMD) techniques for thermal conductivity (k) calculation in molecular dynamics simulations

Aspect	EMD method (Green–Kubo)	NEMD technique
Type of method	Equilibrium	Non-equilibrium
Principle	Linear response theory (Fluctuation–Dissipation)	Fourier's law (steady-state transport)
Formula	$k = \frac{1}{3k_B T^2 V}\int_0^\infty \langle \mathbf{J}(0)\cdot\mathbf{J}(t)\rangle\, dt$	$k_\parallel = -\frac{J_\parallel}{(\nabla T)_\parallel}$
Tensor/isotropy	For isotropic systems: $k = \frac{1}{3k_B T^2 V}\int_0^\infty \langle \mathbf{J}(0)\cdot\mathbf{J}(t)\rangle\, dt$ In general, k is a tensor $k_{\alpha\beta}$: $k_{\alpha\beta} = \frac{1}{k_B T^2 V}\int_0^\infty \langle J_\alpha(0) J_\beta(t)\rangle\, dt$	For anisotropic systems, k is direction-dependent; J and ∇T must be taken along the same direction (e.g., $\parallel$)
Input	Heat current autocorrelation function (HCACF) computed from equilibrium fluctuations	Either: imposed ΔT (measure J) *or* imposed heat flux, e.g., Müller–Plathe method (measure ∇T)
System setup	Equilibrate in NVT/NPT; production run preferably in NVE (or with very weak thermostat) to avoid bias in HCACF; PBC typically used	Hot/cold thermostat regions or momentum/energy-exchange layers; establish steady state; fit ∇T in the interior, away from these boundary/exchange regions (exclude boundary layers and temperature jumps)
Best for	- Bulk systems under PBC where fluctuation-based k is desired	- Complex disordered systems (e.g., amorphous solids, liquids)
	- Avoiding explicit thermal boundary layers	- Situations where controlled driving (ΔT or J) is useful
	- Cases where imposing/maintaining a well-defined steady-state gradient is nontrivial	- Studying length dependence $k(L)$ and extrapolation to bulk
		- Crystalline and ordered structures with well-defined phonon transport
		- Probing nonlinearity beyond linear response (when intentional)
Advantages	- No imposed temperature gradient	- Intuitive physical picture (direct Fourier law)
	- Direct link to equilibrium statistical mechanics	- Explicit control of driving (ΔT or J)
	- No thermostat boundary artifacts during production (NVE)	- Direct access to temperature profile
	- Single simulation setup sufficient	- Can reveal interfacial/Kapitza resistances
Limitations	- Convergence slow when HCACF has long-time tails	- Strong finite-size/length effects when phonon MFP $\gtrsim$ system length
	- Statistical noise in small systems	- Boundary artifacts near thermostats (temperature jumps, non-physical scattering)
	- Finite-size effects: restricted long-wavelength modes and phonon MFP truncation	- Must remain in linear-response regime to extract k (unless nonlinearity is intentionally studied)
	- Heat current definition must be consistent with the employed interatomic potential	- Requires extrapolation to $L \to \infty$ for bulk k
Convergence challenges	Requires long trajectories and careful choice of HCACF integration cutoff to avoid noise-dominated tails; block-averaging or multiple replicas often needed	Requires reaching steady state and robust gradient fitting in the interior; typically needs simulations at multiple lengths and extrapolation ($1/L \to 0$) to obtain bulk k
Size sensitivity	- Statistical noise decreases with system size	- Affected when phonon MFP is comparable to box length (especially in crystals and high-k materials)
	- Finite-size affects long-wavelength phonon contributionsb	- Often strong $k(L)$ dependence due to ballistic-to-diffusive crossover in small cells
		- Systematic extrapolation with several system lengths commonly required
Boundary effects	- Typically PBC with no explicit thermal boundary layers	- Thermostat/exchange regions create boundary layers and temperature jumps
	- Finite-size effects via phonon spectrum truncation remain	- Gradient must be fitted in the bulk interior; boundary-region design and separation length critically matter

Heat transfer properties

Thermal conductivity (k) is a critical property for materials used in high-temperature and thermal management applications[258,259]. Because of their unique atomic configurations and multi-element compositions, which result in remarkable thermal properties, HEAs have become attractive prospects in this field[260,261]. MD simulations have become reliable for investigating these properties at the atomic level, allowing researchers to explore phonon scattering, atomic disorder, and other intricate mechanisms that govern thermal conductivity in HEAs[262,263]. HEAs often have lower heat conductivity than traditional alloys, mostly because of increased phonon scattering brought on by differences in atomic mass and size between their constituent elements[264,265]. Advanced MD simulation approaches, such as the equilibrium (EMD, e.g. Green–Kubo) method and non-equilibrium molecular dynamics (NEMD), are frequently employed to quantify heat flux and analyse temperature gradients, respectively[266,267]. These two primary methods offer complementary insights into atomic-scale thermal transport properties. A detailed comparison of the EMD and NEMD methods, including their underlying theories, formulas, benefits, and drawbacks, is provided in Table 2[268–293] to aid in understanding these approaches.

The thorough examination of NEMD and Green–Kubo methods provides a solid foundation for comprehending the atomic-scale mechanisms controlling thermal transport in HEAs. As discussed in the next sections, this information is essential for customizing the thermal characteristics of HEAs to particular applications. In particular, the concept of the interaction of atomic disorder, phonon scattering, and defect

structures is presented in HEAs and how these factors may impact thermal conductivity in high-temperature environments.

Atomic disorder and phonon scattering. One characteristic of HEAs is atomic disorder, which is made up of several primary constituents without a dominant component. Randomness at the atomic level, caused by this compositional complexity, significantly affects phonon behaviour and lowers thermal conductivity[294,295]. Because the individual atoms in HEAs differ in size and mass, atomic-scale disorder introduces a high degree of phonon scattering [296,297].

More recently, Cheng et al.[264] investigated phonon heat transport in $CrFeCoNiCu_x$ at finite temperatures and showed that chemical disorder and lattice distortion strongly affect phonon-mediated thermal transport. Their results indicated that lattice thermal conductivity is dominated by long-wavelength phonons, with the contribution of long-wavelength LA phonons exceeding that of short-wavelength LA phonons by about one order of magnitude. This contrast was mainly attributed to the long-wavelength behaviour associated with impurity scattering near the Brillouin-zone centre and the strong anharmonic scattering of short-wavelength, high-frequency LA phonons. The latter leads to enhanced linewidth broadening and reduced phonon lifetimes, while impurity scattering caused by strong chemical disorder and lattice distortion contributes to the overall low lattice thermal conductivity. At 100 K, the lattice thermal conductivity of CrFeCoNiCu was reported to be only 9.8 W m^{-1} K^{-1}, less than one quarter of that of pure Cu.

A study by Sun et al.[298] on $Al_{0.3}CoCrFeNi$ HEA using MD simulations, revealed a significant reduction in thermal conductivity compared to traditional alloys. This reduction arises from the order-disorder transitions and the nanoscale precipitations that occur within the alloy structure. These structural features lead to phonon scattering, which disrupts phonon transport and impedes thermal conductivity. This reduction in thermal conductivity is especially pronounced due to the atomic-scale segregation and changes in the material's internal structure as a result of the compositional complexity of HEAs. The inclusion of aluminium in $Al_xCoCrFeNi$ HEAs significantly reduces phonon conductivity due to the large atomic mass mismatch, even at low Al concentrations ($0 \le X_{Al} \le 2$). This reduction in phonon conductivity is not strongly temperature-dependent, indicating minimal inter-phonon scattering, Fig. 7[299].

A recent study by Wang et al.[300] further demonstrated how severe lattice distortion and atomic mass variation can suppress phonon transport in a distorted B2 HEA. Combining experiments with atomistic simulations, they investigated single-phase $(CoNi)_{0.5}(TiZrHf)_{0.5}$, an ordered B2 structure with pronounced chemical and lattice disorder within its two sublattices, and reported an exceptionally low lattice thermal conductivity below 1 W m^{-1} K^{-1}, remaining nearly temperature-insensitive between 300 and 900 K. At 300 K, the lattice contribution was only 0.6W m^{-1} K^{-1}, substantially lower than those of several FCC HEAs. Phonon density-of-states analysis, participation ratios, group velocities, and mean-free-path calculations showed that the distorted B2 alloy exhibits localized vibrational modes, reduced phonon group velocities, and phonon mean free paths approximately one order of magnitude shorter than those in FeCoNiCrMn. These results indicate that strong lattice distortion and large atomic mass contrast can act together to disrupt coherent phonon transport and strongly suppress phonon-mediated heat conduction in HEAs.

Mechanisms of phonon-defect interactions. Beyond chemical-disorder effects associated with mass disorder, force-constant fluctuations, and local strain fields arising from atomic-size mismatch, point and extended lattice defects, including vacancies, dislocations, and grain boundaries, can introduce additional phonon-scattering channels and thereby further suppress lattice thermal transport in HEAs[301–304]. These mechanisms collectively reduce lattice thermal conductivity by enhancing phonon scattering and have been extensively investigated using both atomistic simulations[263,305,306] and experimental lattice-dynamical techniques[307].

In FCC FeCoCrMnNi, inelastic neutron and X-ray scattering revealed that acoustic phonons remain well defined throughout the Brillouin zone, extending to energies of ~20–30 meV and wavevectors above 1 $Å^{-1}$ despite pronounced attenuation arising predominantly from force-constant fluctuations rather than mass disorder. The measured phonon linewidths were reproduced using an average force-constant fluctuation of ~20%, whereas the contribution from mass fluctuations was estimated to be below 0.2 meV[307]. In BCC HfNbTaTiZr, Monte Carlo simulations were first employed to generate different degrees of chemical SRO, followed by MD simulations using an EAM potential together with Warren–Cowley analysis, vibrational density of states (VDOS) calculations, and NEMD[308]. The results showed that increasing SRO promotes the formation of nm-sized HfTi and TiZr B2-like clusters, which undergo a percolation transition, reduce lattice-distortion-related atomic displacements by ~12.5%, modify the high-frequency region of the VDOS, and increase the lattice thermal conductivity by ~12%. These studies demonstrate that local chemical environments and short-range atomic ordering play a central role in governing phonon scattering and lattice thermal transport in high-entropy alloys.

As complementary experimental evidence linking chemical complexity, lattice distortion, and heat transport suppression in FCC HEAs, Lee et al.[309] investigated single-phase FCC solid solutions ranging from Ni to NiCoFeCrMn and found that increasing the number of principal elements (NPEs) markedly reduces the total thermal conductivity, from 83.0 W m^{-1} K^{-1} in Ni to 11.7 W m^{-1} K^{-1} in NiCoFeCrMn at room temperature. Decomposition of κ via the Wiedemann–Franz law revealed that both the electronic contribution (κ_e: 71.7 → 5.77 W m^{-1} K^{-1}) and the lattice contribution (κ_l: 11.3 → 5.93 W m^{-1} K^{-1}) decrease with increasing NPEs, although the reduction in κ_e is dominant. This behaviour was associated with enhanced compositional complexity and severe lattice distortion in the FCC solid solution, providing an experimental indication of how chemical complexity can suppress heat transport in metallic HEAs.

Temperature-dependent heat transfer. Temperature affects thermal transport in refractory high-entropy alloys (RHEAs) through its influence on carrier relaxation times and phonon-related scattering processes, with Singh et al.[310] showing temperature-dependent transport behaviour in TiCrMoWVNbTa RHEAs using DFT-based calculations, CALPHAD predictions, Slack-model lattice thermal conductivity estimates, and experimental validation.

MD simulation of CoCrFeNiCu HEA revealed that its lattice thermal conductivity is strongly reduced with temperature, following the power-law relationship (k) $\propto T^{-0.419}$. From about 2.5 W/m·K at 300 K, the value drops below 1.5 W/m·K at 800 K. This trend is caused by intensified anharmonic phonon-phonon interactions, which reduce phonon lifetimes and shorten mean free paths[262].

Zhang et al.[311] investigated the lattice thermal conductivity of NbMoTaW RHEAs using EMD simulations with a machine-learning interatomic potential. The lattice thermal conductivity was calculated over the range of 300–1500 K, after NPT and NVT equilibration followed by NVE production runs for heat current autocorrelation analysis. Their results showed that k_L decreases with increasing temperature and exhibits an approximately linear relationship with the reciprocal of temperature. At high temperatures, the lattice thermal conductivity was found to fall below the fitted $1/T$-type trend, which was attributed to enhanced anharmonic effects. These results indicate a significant effect of temperature-driven anharmonicity on the lattice thermal conductivity of NbMoTaW RHEAs.

Similarly, Zhang et al.[312] studied the temperature dependence of lattice thermal conductivity in the MoWTaTiZr RHEA using EMD simulations with an EAM potential. The calculations were performed from 300 to 1500 K, and the lattice thermal conductivity was found to decrease monotonically with increasing temperature, showing an approximately linear dependence on $1/T$. This trend was rationalized using the high-temperature phonon transport picture: as temperature increases, the average phonon population rises, phonon–phonon

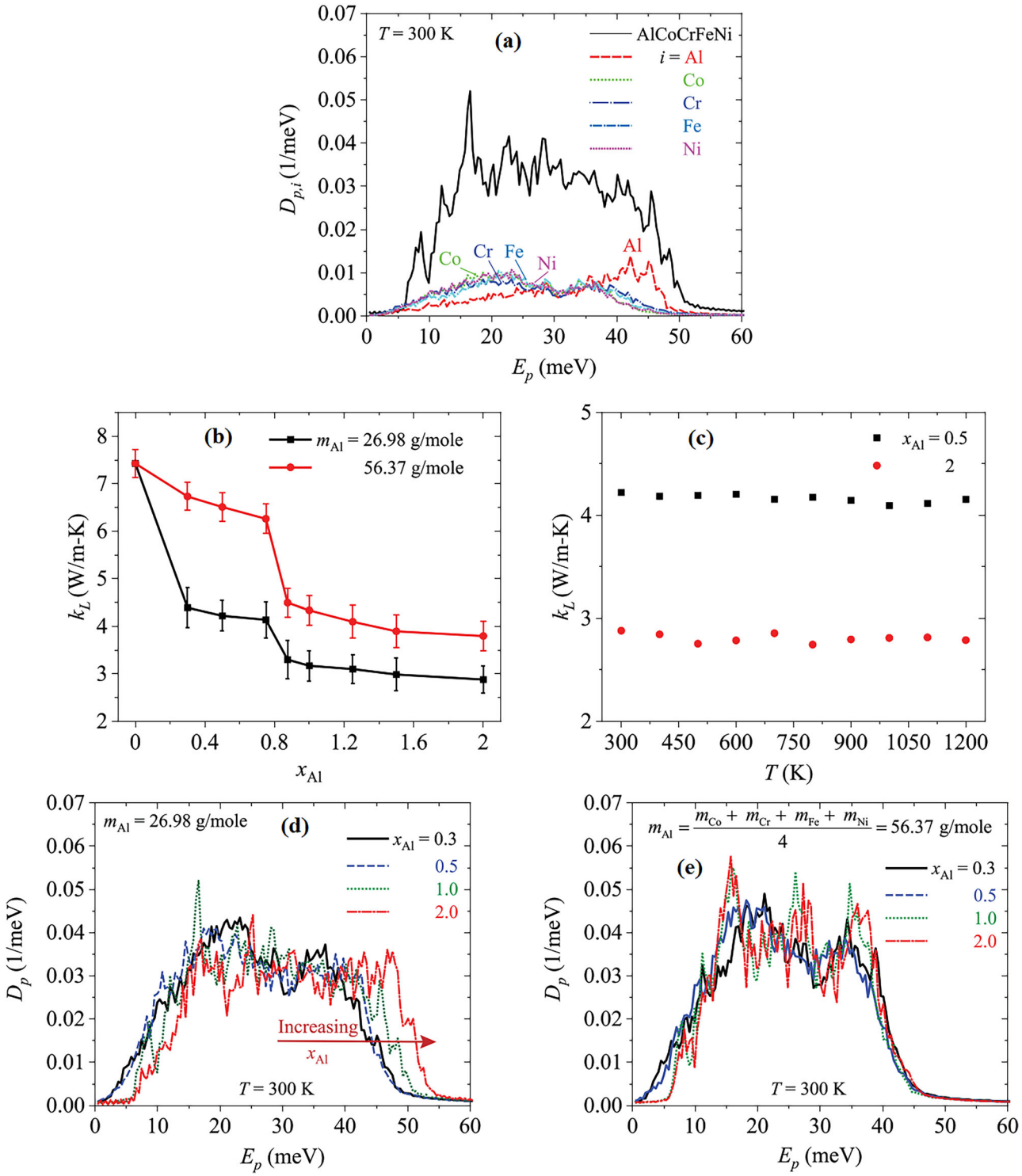


Fig. 7 | Thermal properties of HEA. a Partial D_p of the constituent elements (Al, Co, Cr, Fe, and Ni) of the AlCoCrFeNi HEA. **b** Lattice thermal conductivity (k_L) with respect to the Al content (x_{Al}) calculated using non-equilibrium MD with and without consideration of Al mass mismatch. **c** Lattice thermal conductivity (k_L) with respect to temperature for FCC (x_{Al} = 0.5) and BCC (x_{Al} = 2.0) cases. **d** D_p of $Al_xCoCrFeNi$ (x_{Al} = 0.3, 0.5, 1, and 2) with consideration of Al mass mismatch and **e** those without Al mass mismatch at 300 K from MD simulations. Reprinted from ref. 299 with permission from Elsevier.

collision probability increases, and the phonon mean free path decreases. The authors further associated the reduction in k_L with strong chemical disorder, shortened phonon lifetimes, and enhanced anharmonic scattering of high-frequency phonons. These results indicate that temperature-dependent anharmonic scattering is an important mechanism affecting lattice heat transport in the studied MoWTaTiZr RHEA.

Influence of composition and microstructure. Chemical composition and microstructural features strongly influence the thermal conductivity of HEAs. For instance, in NbMoTaW HEAs, increasing the Mo content raises the lattice thermal conductivity from 1.72 W/m·K to 2.16 W/m·K, which is a 25.6% improvement. This behaviour is attributed to a blue-shift in phonon density of states, that enhances phonon mode participation at specific frequencies[311].

The composition and microstructure of $Al_xCoCrFeNi$ HEAs have a significant effect on their thermal conductivity. The addition of Al reduces the thermal conductivity by causing more lattice distortion and chemical disorder, which increases phonon scattering and reduces phonon mean free paths. The thermal conductivity due to phonons, which is the main mode of heat transfer in HEAs, decreases significantly with increasing Al content, especially between 0 and 5% and 10 and 20%, but remains constant between 5 and 10%. The prolonged thermal spike during displacement cascades is prolonged due to the decrease in thermal conductivity, which helps to promote defect recombination[313].

Microstructural characteristics, such as grain size and orientation, further modulate thermal transport. For the thermal conductivity dependence on grain size, nanocrystalline HEAs exhibit a power law of $L^{1/4}$ opposed to the linear behaviour often seen in non-alloyed nanograined materials. This is attributed to intensified disorder scattering within the nanocrystalline boundaries[314].

The electronic thermal conductivity (k_e) in CrFeCoNi-based random solid solutions is shown to change with temperature and constituent ratios[306]. For example, decreasing the Cr content reduces the electron-phonon coupling factor (G_{e-ph}) and the electronic specific heat (C_e), which impairs defect recombination and enhances defect clustering, while the addition of Al increases k_e and G_{e-ph} by up to two times due to enhanced phonon coupling mechanisms. While adding Cu increases thermal conductivity by about 1.5 times without significantly affecting C_e, Mn has little impact on the electronic and thermal conductivity properties[306].

Interface properties

Static and dynamic wettability. Wetting refers to the study of how a liquid interacts with a solid surface at the atomic or molecular scale, and how these interactions affect macroscopic interfacial statics and hydrodynamics. It has important implications in many industrial fields, as discussed in the "Potentials for metal-liquid interfaces" section. To understand wetting in the context of HEAs, it is essential to first consider some fundamental concepts that apply regardless of the specific liquid-solid combination. The wettability of a solid surface with respect to a given liquid is usually determined by the interplay of interfacial energies: the solid-vapour (γ_{SV}), solid-liquid (γ_{SL}), and liquid-vapour (γ_{LV}, or simply γ) interfacial tensions. When a sessile liquid droplet deposited on a metal surface forms a spherical cap, its equilibirum contact angle θ_0 is given by the Young-Dupré equation:

$$\cos\theta_0 = \frac{\gamma_{SV} - \gamma_{SL}}{\gamma}\,. \tag{36}$$

Adhesion (force between liquid and solid) and cohesion (force within the liquid) play critical roles in determining both the equilibrium wetting state and wetting dynamics or relaxation. In MD simulations contact angles are determined by identifying interfaces (liquid-vapour and liquid-solid) as regions with steep density gradients. Once the droplet surface is extracted, the contact angle can be calculated with different approaches, depending on the wetting state: at equilibrium, it is found by fitting a spherical or cylindrical cap to the droplet interface, while in non-equilibrium conditions, the dynamic contact angle is estimated by locally fitting a plane or line to the interface close to the three-phase contact line. Interface capturing approaches allow for the determination of the contact angle, but do not provide any quantitative information on surface energies γ, γ_{SL} and γ_{SV}. The liquid/vapour surface tension γ can be easily computed from the interface-parallel and interface-perpendicular stresses via the Kirkwood–Buff formula[315]. The energies related to the solid surface are on the other hand much more challenging to quantify. The solid-vapour interface tension γ_{SV} is essentially impossible to compute directly, and needs to be extracted from equation (36) by knowing all the other parameters. The solid-liquid interface tension γ_{SL} can be determined via free-energy calculations[316,317].

Transport coefficients can be obtained both from equilibrium and non-equilibrium simulations. The reader should refer to the cited articles for a detail description of the methods. It suffices to say that the discussion of the advantages and the limitations for the calculation of thermal conductivity mostly apply here too (see the "Heat transfer properties" section and Table 2). Table 3 lists the mathematical formulas used to compute the coefficients using Linear Response Theory and non-equilibrium simulations. We remind that the equivalent Einstein formula can be obtained for each Green–Kubo formula using the following equality[318]:

$$\int_0^\infty d\tau \left\langle f(0)f(\tau)\right\rangle = \lim_{t\to\infty}\frac{1}{2}\frac{d}{dt}\left\langle F^2(t)\right\rangle,\ \text{with}\ F(t) = \int_0^t f(\tau)d\tau\,. \tag{37}$$

The shear viscosity coefficient η determines the stress response of a fluid to a shear deformation over time (shear rate). The viscosity coefficient can be extracted from equilibrium MD simulations using Green–Kubo or Einstein formulas[319,320]. The convergence of said formulas can be very slow, and sampling the autocorrelation function of the pressure tensor components requires frequent I/O operations, which may slow simulations substantially. Nonetheless, the challenges of computing the viscosity coefficient from linear response theory are well-known, and optimisation strategies have been proposed[321]. Alternatively, one can reproduce a rheology experiment in-silico, and impose a shear deformation to the molecular system by either adding a periodic acceleration field or by directly deforming the triclinic simulation box. The comparison of these approaches with equilibrium methods is discussed in ref. 322. While being easier to analyse and interpret, these approaches come with all the challenges of non-equilibrium MD, such as devise a way to properly thermalise the system and determining the best trade-off between minimizing the system perturbation and maximizing the response signal-to-noise ratio.

While viscosity is a very well-defined and common measure of energy dissipation in fluid flows, the description of the energy dissipation occurring at the interface between a liquid and a solid is not as straightforward. A liquid-solid friction coefficient (λ) can be determined both using equilibrium[323] and non-equilibrium[324] MD simulation. This coefficient can be interpreted in terms of a *slip length* (b), i.e. the distance from wall at which a wall-parallel linear velocity profile would extrapolate to zero. In terms of continuous hydrodynamics, $b = 0$ corresponds to a no-slip boundary conditions for Navier-Stokes equations. The friction coefficient provides a measurement of the energy dissipated by a flow at the liquid-solid interface. In wetting dynamics, a liquid-vapour interface (e.g. the one of a droplet) moves over a solid surface. The location where liquid, vapour and solid phases meet is called *three-phase contact line*. The increase of liquid slip near moving contact lines has been proposed theoretically[325] and shown via molecular dynamics simulations[326]. A measure of energy dissipation (or equivalently, mobility) of contact lines is the *contact line friction coefficient* (μ_f), defined by relating the speed of the moving contact line (u_{cl}) to the out-of-equilibirum Young stress. The contact line friction coefficient can be measured from MD simulations by correlating the velocity of a moving contact line an the microscopic dynamic contact angle[327,328].

The study of wetting properties of metals and metal alloys present a richer phenomenology that is usually absent in most systems, e.g. covalent solids. In the case of molten metal or alloy droplets wetting a metal or alloy surface, mutual diffusion between the wetting liquid and the wetted solid (*interdiffusion*) may be significant. This phenomenon can have important implications for metal casting and for coating production via sputtering. Addressing the effect of inter-diffusion and its dependence on alloy composition and plane orientation is of interest for many application, such as welding and heat transfer. Chen et al. studied the mutual diffusion of wetting Cu into an Inconel alloy (FeNiCr) and determined it to be the cause of the limited wettability of the surface (i.e. limited spreading of Cu droplets) during vacuum brazing[156]. Li et al. simulated AgCuTi spreading over Fe surfaces, and found qualitative differences in the formation of precursor films and in the spreading rates depending on mutual diffusivity: metals with high diffusivity in Fe (Cu, Ti) tend to spread less than metals with low diffusivity (Ag). The orientation of the crystal plane on the Fe surface also plays a role, with alloy droplets spreading faster on (101) than on (111)

Table 3 | Comprehensive Comparison of Equilibrium (EMD) and Non-Equilibrium (NEMD) techniques for determining liquid viscosity (η), liquid/solid friction (λ), interfacial thermal resistance (R_K), and contact line friction (μ_f) from molecular dynamics simulations

	EMD method	NEMD method
Principle	Linear response theory, Langevin formalism	Rheology, heat transfer law, Young-Dupré law
Shear viscosity		
Formula	$\eta = \frac{V}{3k_BT}\sum_{i\neq j}\int_0^\infty dt\langle P_{ij}(0)P_{ij}(t)\rangle$	$\eta = P_{ij}\frac{L_j}{u_i^g}$
Input	Volume (V), temperature (T), shear stresses ($\{P_{ij}\}_{i\neq j}$).	Deformation velocity (u_i^g), shear stress (P_{ij}), box length (L_j).
System setup	Box containing liquid molecules at equilibrium, preferably in the NVT or NVE ensemble.	Triclinic thermalised liquid box subject to a continuous shear deformation.
Solid-liquid friction		
Formula	$\lambda = \frac{1}{Ak_BT}\int_0^\infty dt\langle F_w(0)F_w(t)\rangle$	$\lambda = \eta\frac{\partial_\perp u_\parallel}{u_\parallel}\vert_w$
Input	Solid-liquid interface area (A), temperature (T), force between liquid and solid molecules (F_w).	Wall-parallel flow velocity ($u_\parallel$), wall-normal gradient of wall-parallel flow velocity ($\partial_\perp u_\parallel$).
System setup	Liquid molecules confined between two solid walls at equilibrium, in any ensemble which keeps the solid-liquid interface area fixed.	Single phase Couette or Poiseuille flow simulation (moving walls producing a shear flow profile).
Contact line friction		
Formula	$\mu_f = \frac{k_BT}{\sigma^2 L_\otimes}\int_0^\infty dt\frac{\langle x_{cl}(0)x_{cl}(t)\rangle}{\sigma^2}$	$\mu_f = \lim_{\theta\to\theta_0}\langle\frac{\gamma(\cos\theta_0-\cos\theta)}{u_{cl}}\rangle$
Input	Contact line position (x_{cl}), temperature (T), in-plane box length ($L_\otimes$), fluctuation of the c.l. (σ).	Equilibrium and dynamic contact angle (θ_0, θ), surface tension (γ), c.l. speed (u_{cl}).
System setup	Either a confined liquid meniscus or a still droplet deposited on a surface, in the NVT ensemble.	Either a two-phase Couette flow or spontaneous droplet spreading.
Kapitza resistance		(AEMD method)
Formula	$\frac{1}{R_K} = \frac{1}{Ak_BT^2}\int_0^\infty dt\langle q(0)q(t)\rangle$	$E(t) = E_0 - \frac{A}{R_K}\int_0^t dt\Delta T_{sl}(t)$
Input	Solid-liquid interface area (A), temperature (T), energy flux across the interface (q).	Solid-liquid interface area (A), total energy (E), solid-liquid temperature difference (ΔT_{sl}).
System setup	Two different substances, typically a liquid and a solid, maintained in thermal equilibrium at a uniform temperature within an NVE ensemble.	Two different substances (typically liquid/solid), initially at different temperatures, exchanging heat in an NVE ensemble while relaxing to thermal equilibrium.

planes[158]. Qu et al. studied the wettability of Al droplets on FeNi substrates and the formation of surface intermetallics emerging during the mutual diffusion process (Fe_2Al_5, NiAl and Ni_3Al)[157]. Other important factors affecting the wetting behaviour of surfaces are topography and chemical inhomogeneity. In the case of HEA, certain metal species tend to segregate at surfaces and at grain boundary interfaces (i.e. they have a substantially different concentration with respect to the bulk). Wynblatt and Chatain employed Monte Carlo/Molecular Dynamics simulations to study the segregation and layering at free and grain interfaces for the Cantor alloy (CoCrFeMnNi), with the aim of constructing a simple analytical model which would assist material screening[329]. Ferrari and Körmann calculated the surface segregation free energies for the elements of the Cantor alloy and found that Ni tends to segregate the most under vacuum, while Cr segregate the most in the presence of an oxygen layer[330]. Li et al. combined experimental techniques and thermodynamic modelling to study grain boundary segregation again in the Cantor alloy, and found that Ni and Mn tend to enrich grain boundaries while other elements depletes them[331].

Kapitza resistance. Kapitza resistance (or thermal boundary resistance) is the interfacial thermal resistance that arises because heat carriers – primarily phonons – are partially reflected at the interface between two dissimilar materials due to differences in their vibrational spectra, acoustic impedances, and interfacial bonding. This imperfect transmission leads to a finite temperature drop across the interface under a steady heat flux, even in the absence of interfacial thickness[332,333]. The acoustic mismatch model (AMM) explains this resistance in terms of differences in acoustic properties between materials, while the diffuse mismatch model (DMM) accounts for variations in phonon density of states and scattering mechanisms. For a simple one-dimensional heat transfer across an interface, Kapitza resistance is typically expressed as:

$$R_K = \frac{\Delta T}{Q}, \tag{38}$$

where ΔT represents the temperature difference at the boundary, and Q denotes the heat flux across it. Molecular dynamics simulations provide valuable tools to investigate this interface property at the atomic scale.

Three primary methods are commonly used[334]: Equilibrium Molecular Dynamics employs the Green–Kubo formalism to calculate thermal conductivity, which is inversely related to the Kapitza resistance. This approach leverages spontaneous heat flux fluctuations in an equilibrium system to extract several transport coefficients, such as interfacial thermal resistance. Non-Equilibrium Molecular Dynamics imposes an external temperature gradient across the system, enabling direct computation of the heat flux and corresponding temperature profiles. The Kapitza resistance is then determined from the interfacial temperature discontinuity and the applied heat flux. *Approach-to-Equilibrium Molecular Dynamics (AEMD)* initiates the system with a non-uniform temperature distribution and tracks the relaxation dynamics. The Kapitza resistance is determined by analysing the relaxation of the temperature gradient across the interface as well as the temporal evolution of the total energy in one of the media[335].

Mechanical properties

Mechanical performance is a primary driver for many high-entropy alloy applications, and it is also a stringent benchmark for simulation because it couples chemistry, microstructure, and defects across multiple length and time scales. From a modelling standpoint, it is useful to distinguish (i) *intrinsic* descriptors that primarily reflect bonding and lattice stability (elastic constants, moduli, Poisson's ratio, ideal strength, and defect energetics such as stacking-fault energies) from (ii) *microstructure- and pathway-dependent* responses (yield strength, strain hardening, ductility, hardness, and fracture), which depend on the activated mechanisms and on the processing-defined defect population. Consequently, the objective is not merely to reproduce stress–strain curves, but to identify which mechanisms dominate under given temperature, strain-rate, and microstructural conditions, and how these mechanisms can be tuned by composition and local chemical environments.

Elastic and strength response. Elastic properties quantify the small-strain mechanical response and are commonly extracted from calculated elastic constants or from the initial slope of stress–strain relations under minor deformations. In HEAs, elastic modulus and Poisson's ratio are especially informative because they provide a compact, transferable summary of lattice stiffness and lateral compliance that can be compared across compositions and used to parameterize higher-scale constitutive models. Atomistic simulations have been widely used to resolve composition trends in elastic moduli and to connect them to local bonding and lattice distortion. For example, molecular dynamics simulations of $CoCrFeNi(Al_{0.3}Ti_{0.2})_x$ indicate that alloying with Al and Ti increases both stiffness and strength: the Young's modulus rises from 171.9 GPa to 205.6 GPa and the tensile strength increases from 18.8 GPa to 21.6 GPa with increasing Al/Ti content, consistent with a strengthening effect associated with composition-driven changes in the resisting defect landscape[336]. Thermal effects can be comparably important: MD simulations for CoCrCuFeNi report a measurable reduction in modulus with increasing temperature (e.g., ~180 GPa at 77 K decreasing to below 170 GPa at 500 K), emphasizing that elastic descriptors used for screening or parameterization should be interpreted at the relevant service temperature rather than as composition-only constants[337].

Strength and yielding in HEAs reflect the competition between dislocation nucleation/motion, local order, and defect interactions. As a result, atomistic tensile/compression tests are often used to isolate the mechanistic origin of yield trends under controlled defect states. In V–Cr–Fe–Co–Ni systems, MD-guided exploration has shown that yield strength can vary strongly with composition. In particular, $V_5Cr_{16}Fe_9Co_{35}Ni_{35}$ exhibits a high yield strength of 18.28 GPa, attributed to increased resistance to dislocation nucleation and to the formation of a high density of stair-rod dislocations that promote strain hardening and elevated flow stress[338]. This illustrates a recurring HEA design theme: chemistry does not merely shift averaged lattice parameters, but can reorganize the hierarchy of dislocation reactions that controls strength.

For FeNiCrCoCu, MD simulations explicitly quantify how boundary conditions, defects, and loading parameters alter yield metrics[339]. The yield stress of an uncracked model is 22.53 GPa in the NVT ensemble and 19.11 GPa in the NPT ensemble, whereas the cracked model yields at 14.54 GPa (NVT) and 13.89 GPa (NPT), highlighting the strong weakening effect of cracks and the sensitivity to thermo-barostatic constraints. The same study reports systematic decreases in yield stress with increasing temperature (70–1500 K) for both cracked and uncracked configurations, increases in yield stress at higher strain rates, and a reduction of yield stress with increasing Cu content, consistent with thermally activated softening and composition-dependent changes in solid-solution strengthening[339]. These dependencies are summarized in Fig. 8. Collectively, such results underscore that meaningful strength predictions for HEAs require explicit specification of defect state (cracks/voids), ensemble/loading protocol, temperature, and strain rate, in addition to composition.

Plasticity and fracture mechanisms. Beyond elastic constants and yield stresses, the central mechanistic question is which defect processes accommodate plasticity—dislocation glide and reactions, twinning, shear localization, and stress-assisted phase transformations—and how these processes are biased by chemical disorder and microstructural constraints. MD simulations are particularly effective here because they provide direct access to evolving atomistic configurations, enabling classification of local structure (FCC/HCP/BCC/amorphous), identification of defect types, and mapping of where plasticity nucleates and localizes.

For $FeNiCrCoCu_x$ under uniaxial tension, MD simulations indicate that plastic deformation is mediated by coupled dislocation activity, phase transformation, and shear strain[340]. For $FeNiCrCoCu_1$ at 300 K and a strain rate of $1 \times 10^{10}\ s^{-1}$, the response is elastic up to a yield strain of 0.183, followed by a stress drop that marks the onset of plasticity. Structural analysis shows that the parent FCC lattice progressively converts into HCP, BCC, and amorphous regions during deformation, while twin boundaries and stacking faults emerge as key mesoscale signatures of the activated mechanism set (Fig. 9a–f)[340]. Dislocation analysis further indicates that Shockley partial dislocations dominate and that the dislocation density increases markedly with strain, from $7.85 \times 10^{16}\ m^{-2}$ at a strain of 0.183 to $1.20 \times 10^{19}\ m^{-2}$ at 0.88[340]. These observations make explicit the mechanistic link between local structural transitions and macroscopic flow: chemistry and disorder influence the relative accessibility of partial-dislocation-mediated slip, twinning, and transformation pathways rather than simply shifting a single "strength" parameter.

Architectured microstructures introduce an additional control variable: geometry can select deformation modes even at fixed composition. For equiatomic CoCrFeMnNi HEA foams, MD simulations reveal a three-stage response (elasticity, plasticity, fracture) in which both ultimate tensile strength (UTS) and elastic modulus decrease with increasing temperature and porosity[341]. Quantitatively, the UTS drops from 13.51 GPa at 0% porosity to 4.55 GPa at 30% porosity, reflecting the combined effects of reduced load-bearing area and stress concentration at pore surfaces[341]. Defect analysis again identifies Shockley partial dislocations as dominant, but shows a strong porosity dependence in dislocation density, dislocation length distributions, and crack initiation propensity (Fig. 9g)[341]. This example highlights a key modelling implication for HEAs: microstructural state variables (porosity, grain size, pre-existing cracks) can be as consequential as composition for the realized deformation pathway.

Crack initiation and propagation couple these plasticity processes to local stress intensification and, in some HEAs, to stress-induced structural transformations. In $Ta_{0.5}HfZrTi$, MD simulations of crack-free and edge-cracked configurations indicate that phase transformations near the crack tip play a central role: under tensile loading, BCC atoms transform locally to HCP (and, depending on local shear/stacking faults, can transiently form FCC regions), with the transformation pathway sensitive to crack geometry (e.g., crack angle) and stress state[342]. Figure 10a–g illustrates the associated stress–strain response and representative atomistic configurations.

In FCC CrMnFeCoNi, MD simulations further indicate that fracture resistance can be enhanced by a synergistic interaction between amorphization and dislocation activity near crack tips[343]. Amorphous regions form in highly stressed zones during plastic deformation, while surrounding dislocations confine these regions and relax local stress concentrations, delaying crack advance and promoting crack-tip blunting[343]. With increasing strain, dislocation-rich regions can progressively transform into amorphous structures, providing an additional dissipation channel. Dislocation analysis identifies Shockley partials with Burgers vectors $\frac{1}{6}\langle 112\rangle$ as the primary carriers in this mechanism set[343]. Representative deformation patterns and defect structures are shown in Fig. 10h–m. Atomistic mechanical simulations are therefore valuable for isolating how chemistry and local order shape defect processes, but their quantitative predictions remain constrained by the interatomic potential, accessible length/time scales, and the typically high strain rates required in MD. Recent PTA-MD work underscores this limitation. Conventional MD is restricted to

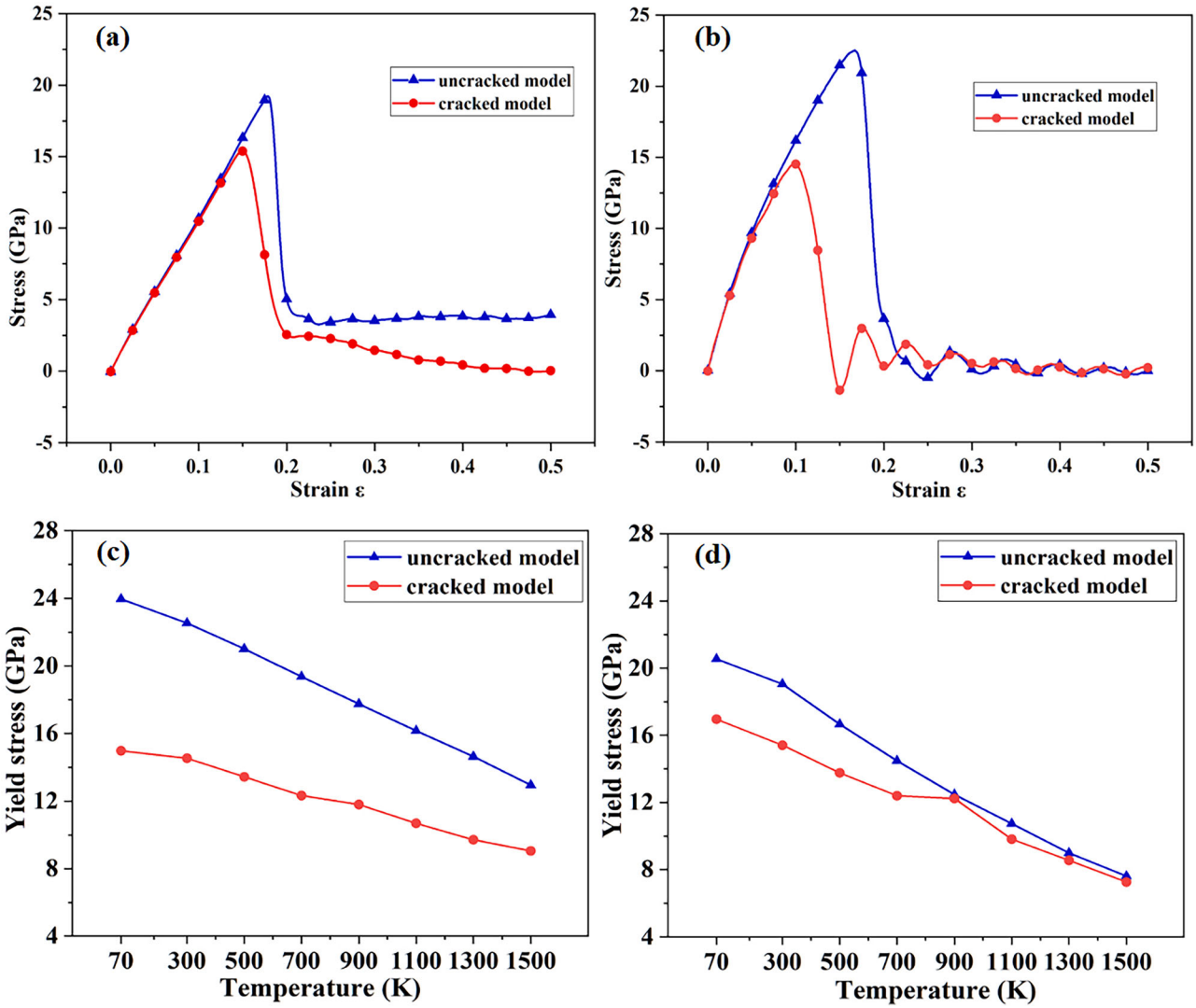


Fig. 8 | Mechanical response of HEA. Stress–strain curves of the uncracked and cracked models during tensile deformation under **a** NVT and **b** NPT ensembles. Variation of the yield stress with temperature for the cracked and uncracked models under **c** NVT and **d** NPT ensembles. Reprinted from ref. 339 with permission from Elsevier.

nanosecond- or microsecond-scale trajectories, forcing strain rates of about 10^8–10^{10} s^{-1}, whereas time-averaging of slow observables enabled fully atomistic metal deformation simulations at 10^{-4}–10^{-3} s^{-1} without modifying the potential-energy surface; this highlights why direct stress–strain comparisons require caution[344]. Bridging to experimentally relevant regimes requires (i) systematic validation of potentials against composition-dependent elastic constants and defect energetics, (ii) careful separation of intrinsic chemical effects from microstructural state variables (cracks, porosity, grain size), and (iii) coupling atomistic mechanism maps to mesoscale and continuum frameworks (e.g., crystal plasticity or damage models) that can represent heterogeneity and rate/temperature effects with experimentally consistent boundary conditions.

Electronic properties

Electronic and transport properties provide a complementary lens on chemical complexity in HEAs because charge transport is inherently sensitive to (i) the electronic structure near the Fermi level, (ii) configurational disorder and associated scattering, and (iii) magnetic state and spin disorder. Accordingly, modelling must connect chemically disordered atomic configurations to electronic descriptors (density of states, orbital character, bonding/charge transfer, magnetic moments) and then to measurable transport coefficients (conductivity/resistivity, Seebeck coefficient, magnetotransport, and thermoelectric figure of merit). A recurring practical complication is that electrical measurements also reflect extrinsic microstructural factors (grain boundaries, precipitates, segregation, cracks/porosity), so a predictive workflow should make explicit which part of the response is intrinsic to chemical disorder and which part is microstructure-controlled.

Density functional theory provides direct access to the electronic density of states (DOS), partial density of states (PDOS), bonding trends, and magnetic moments, and it supplies key inputs for transport modelling (e.g., carrier concentrations, effective masses, and scattering-relevant orbital character). For $AlCo_xCrFeNi$ ($0.25 \le x \le 2$), DFT analysis based on PDOS and electron density difference maps shows that *d*-states dominate the total DOS near the Fermi energy over a window of approximately −3.1 to 2.4 eV, whereas *s*- and *p*-orbital contributions are comparatively minor[345]. As shown in Fig. 11, increasing Co content from $x = 0.25$ to $x = 2$ reduces PDOS values near the Fermi level; notably, $AlCo_2CrFeNi$ exhibits the lowest PDOS in the reported set, consistent with increased electronic stability in the sense of a reduced density of available states at E_F[345]. Electron density difference maps on the (110) plane further indicate that charge redistribution intensifies with higher Co concentration, reflecting composition-dependent changes in local bonding and charge transfer[345]. In parallel, VEC estimates increase from 6.885 to 7.506 as Co content rises, providing a compact

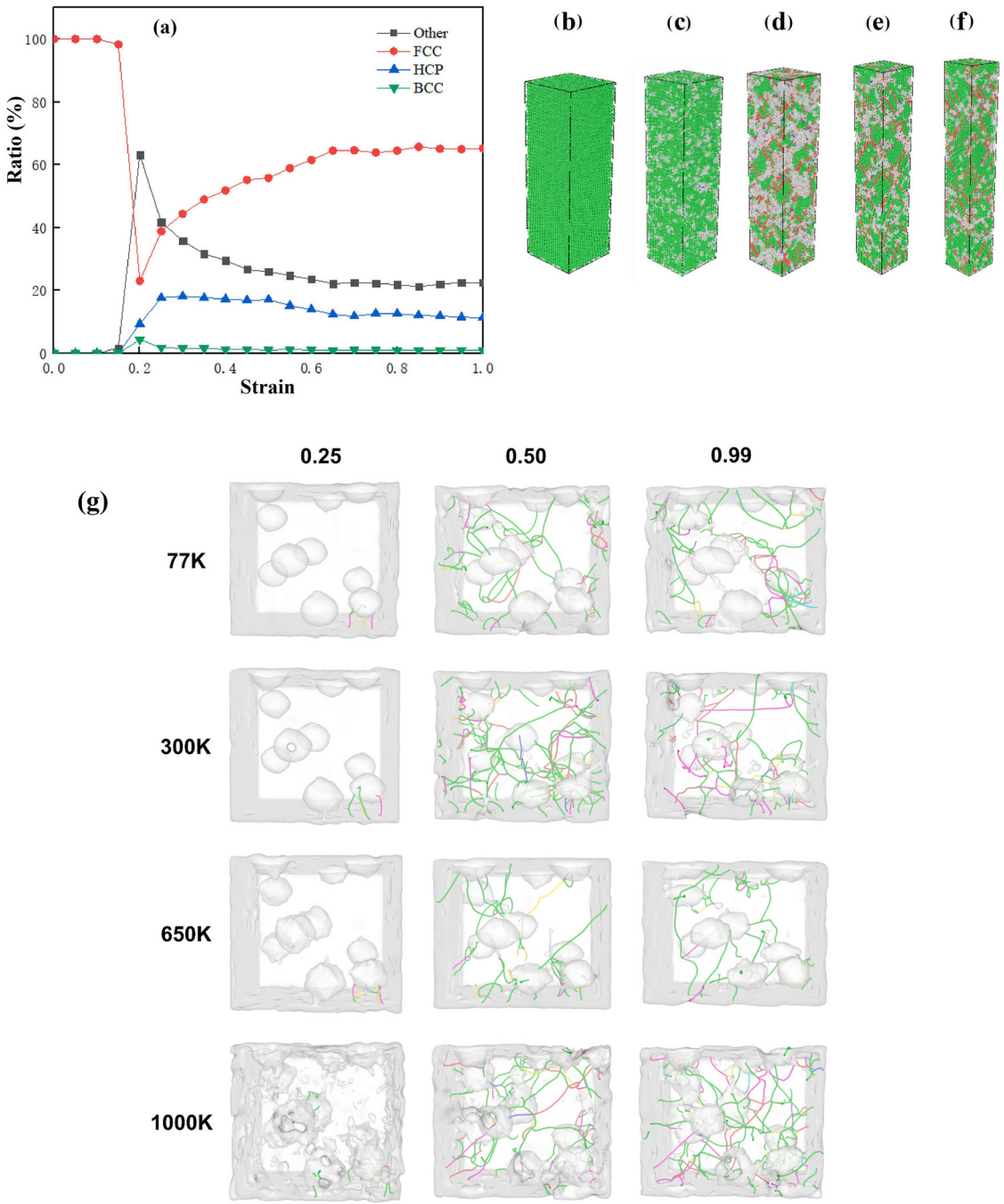


Fig. 9 | Lattice modification during simulated mechanical tests. Proportion of atoms with different lattice structures during uniaxial stretching (**a**). Microstructures of $FeNiCrCoCu_{1.0}$ at strains of **b** 0, **c** 0.183, **d** 0.24, **e** 0.88, and **f** 1.0; atoms are coloured by local structure (FCC: green; HCP: red; BCC: blue; amorphous: grey). Dislocation distributions in CoCrFeMnNi HEA foam under uniaxial tensile loading at low porosity (5%): snapshots of the defect network at 0.25, 0.50 and 0.99 fractions of the applied strain for 77 K, 300 K, 650 K, and 1000 K (**g**). Dislocation types are identified by Burgers vector: $\frac{1}{2}\langle 110\rangle$ perfect (blue), $\frac{1}{6}\langle 112\rangle$ Shockley partials (green), $\frac{1}{6}\langle 110\rangle$ stair-rod partials (pink), $\frac{1}{3}\langle 111\rangle$ Frank partials (cyan), and $\frac{1}{3}\langle 100\rangle$ Hirth partials (yellow). Panels (**a**–**f**) reprinted from ref. 340 with permission from Elsevier. Panel (**g**) reprinted from ref. 341 with permission from Elsevier.

descriptor for tracking systematic shifts in electronic filling and associated phase/transport tendencies[345]. These results emphasize a key point for HEAs: even when the average lattice remains a simple parent structure, the local electronic landscape can be strongly tuned by composition, with direct implications for scattering and magnetic response.

For conductivity, configurational disorder in HEAs introduces strong electron scattering that increases residual resistivity and can obscure intrinsic band-structure trends. In $Al_xCrFeCoNi$, first-principles calculations indicate that increasing Al content drives a structural transition from FCC to BCC, and that the resulting residual resistivity is dominated primarily by intrinsic chemical disorder rather than spin-polarization effects[346]. Theoretical residual resistivities span ~84 μΩ · cm for the FCC phase and about 135 μΩ · cm for the BCC phase at 0 K; when scaled to room temperature, these values correspond to roughly 100–164 μΩ · cm[346]. The predicted range is consistent with reported experimental values on the order of 100–200 μΩ · cm, supporting the interpretation that Al-driven disorder and structure selection jointly control electrical resistivity in this system[346]. More broadly, these examples illustrate how composition can modulate transport both indirectly (by changing crystal structure and ordering tendencies) and

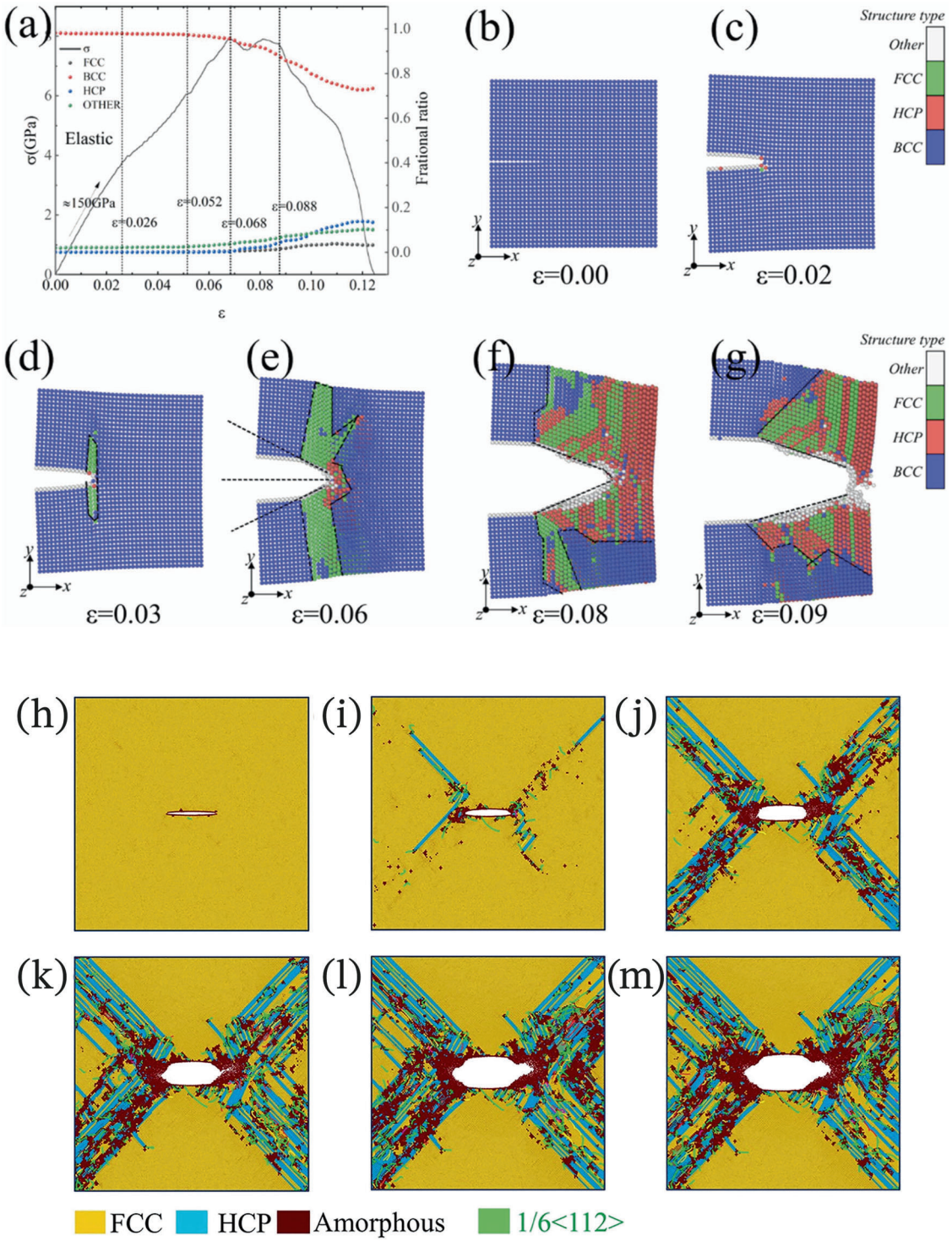


Fig. 10 | Crack propagation in HEAs. Crack-free stress–strain curve of $Ta_{0.5}HfZrTi$ under uniaxial tension, with the evolution of local structure fractions (**a**). Representative configurations at increasing strain (ε = 0, 0.02, 0.03, 0.06, 0.08, 0.09), coloured by local structure (BCC/FCC/HCP/other) (**b**–**g**). Deformation patterns of the CrMnFeCoNi HEA sample at different tensile strains: **h** ε = 2.5%, **i** ε = 5%, **j** ε = 7.5%, **k** ε = 10%, **l** ε = 12.5%, and **m** ε = 13.75%. Atoms in FCC, HCP, and amorphous structures are coloured yellow, blue, and red, respectively. Dislocation lines with Burgers vector $\frac{1}{6}\langle 112\rangle$ are coloured green. Panels (**a**–**g**) reprinted from ref. 342 with permission from Elsevier. Panels (**h**–**m**) reprinted from ref. 343 with permission from Elsevier.

directly (by changing the electronic states and the amplitude of disorder scattering), so conductivity trends should be interpreted together with phase/structure predictions. Carrier dynamics, including carrier density and scattering length scales, are central to electronic transport in metallic HEAs because they determine how efficiently charge carriers propagate through chemically disordered lattices.

In metallic concentrated solid solutions, the electron mean free path provides a direct descriptor of disorder-limited transport because the residual resistivity is directly related to the electron mean free path, or equivalently the lifetime, at the Fermi energy. In NiFeCoCrMn-derived concentrated solid solutions and high-entropy alloys, ab initio transport calculations show that the carrier density remains as high as in ordinary

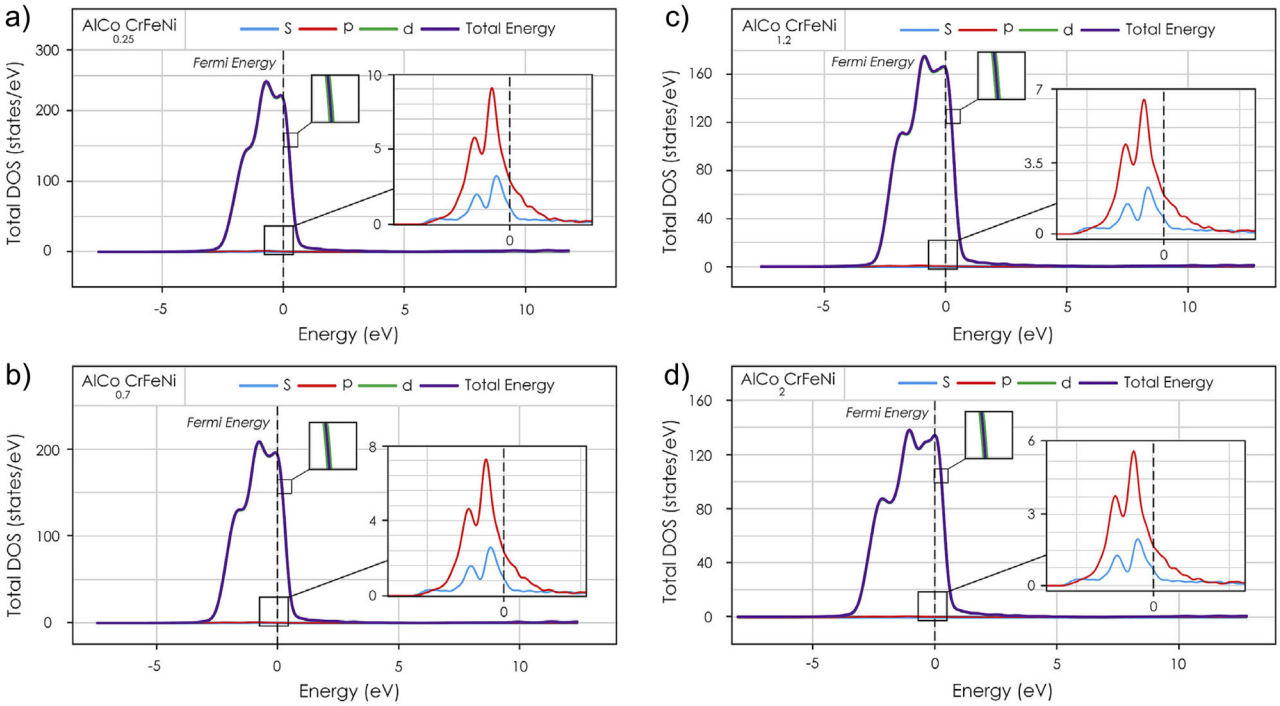


Fig. 11 | Electronic density of states of HEAs. Total and partial electronic density of states (PDOS) for $AlCo_xCrFeNi$ at $x = 0.25$, 0.7, 1.2, and 2 (**a**–**d**). Energies are shown relative to the Fermi level (set to $E_F = 0$ eV). The PDOS highlights the dominant *d*-states near E_F and their evolution with Co content. Panels (**a**–**d**) reprinted from ref. 345 with permission from Elsevier.

metals, while the electron mean free path varies strongly with alloy chemistry, ranging from ~10 Å in the strong-scattering limit to nearly 10^3 Å in weakly scattered alloys[347]. The dominant mechanism was identified as spin-dependent site-diagonal potential scattering. For alloys containing only Fe, Co, and Ni, the majority-spin channel experiences negligible disorder scattering and therefore acts as a high conductivity short-circuit channel. In contrast, Cr- and Mn-containing alloys exhibit strong disorder scattering in both spin channels due to electronic filling effects[347].

Because HEAs frequently include multiple transition metals, magnetic contributions are often inseparable from electronic/transport behaviour. Composition can tune both magnetic ordering and the underlying electronic structure, with consequences for spin-dependent scattering and magnetotransport. In CoFeMnNiX (X = Al, Cr, Ga, Sn), combined ab initio and experimental analysis shows that adding Al, Ga, or Sn promotes ordered phases associated with significant short-range ordering, corroborated by AIMD[348]. These compositions exhibit substantially higher saturation magnetism—reaching 147.86 A m^2 kg^{-1} for CoFeMnNiAl—relative to the base CoFeMnNi alloy[348]. DFT interpretation suggests that the antiferromagnetic ordering associated with Mn in FCC CoFeMnNi is suppressed in the BCC CoFeMnNiAl alloy, whereas CoFeMnNiCr is predicted to be paramagnetic[348]. Such results demonstrate that magnetic response can be engineered through composition-driven structural selection and local chemical order, not solely by adjusting the concentration of a nominally magnetic element.

Related trends are seen in $FeCoNiSi_{0.2}Cr_{0.2}$ and $FeCoNiSi_{0.2}Mn_{0.2}$, where DFT predicts a higher saturation magnetization for the Mn-containing alloy (118.49 emu/g) compared to the Cr-containing alloy (105.89 emu/g), in agreement with experimental data[349]. The presence of Mn is proposed to reduce the population of spin-down electrons, enabling Mn atoms to adopt a more ferromagnetic state, potentially mediated by coupling between Mn and the FeCoNi matrix[349]. In modelling terms, these examples highlight that a realistic description of magnetic and electronic properties in HEAs often requires treatment of finite-temperature spin disorder and its coupling to chemical disorder and local ordering—effects that are not fully captured by static, single-configuration DFT.

Across electronic, thermoelectric, and magnetic applications, the principal open issues are methodological: quantitative prediction of conductivity and thermoelectric coefficients requires consistent treatment of configurational disorder (configuration sampling or effective-medium approaches), magnetic disorder, and electron–phonon (and electron–magnon) scattering, followed by validation against experiments where microstructure and defect state are controlled and reported. Progress will therefore depend on disorder-aware electronic/transport formalisms integrated with finite-temperature sampling and on datasets that support uncertainty-aware extrapolation across composition space.

Discussion

In this section, we present research directions in the computational modelling of HEAs that remain unexplored or not completely investigated. The paragraphs are organized around three key aspects that we deem particularly important: model validation, uncertainty quantification, and multi-scale modelling.

Despite their enormous promise, most atomistic models are still unable to adequately encompass all HEAs compositions and lack definitive validation against ab initio methods. Almost all semi-empirical models have been constructed to reproduce local order and mechanical properties of "Cantor-like" alloys, based on Co, Fe, Ni and Cu. There are essentially no examples in the literature of atomistic models for alternative compositions that have been proposed as HEAs and could be of interest for wear-resistant coatings. This is the case for example of the refractory alloys proposed by Senkov et al.[350] or Gorr et al.[351]. The reason likely lies in the large atomic-size mismatch and the related lattice distortion introduced by elements such as Al, Ti, W, and Mo, which are difficult to capture with EAM or MEAM.

Regarding data-driven approaches, the few comparative studies of MLIPs that we could find in the literature are not entirely satisfactory. Gubaev et al. assessed the training efficiency and transferability of a Moment Tensor Potential (MTP)[352], which is similar in spirit to LRPs, and a Gaussian moment NNP[353] for TaVCrW; they concluded that the former is more data-efficient, whereas the latter is more accurate on out-of-distribution configurations. However interesting, this outcome is expected when comparing

"classical" ML approaches with NNPs. Maxson et al. performed a more comprehensive exploration of several MLIPs on an ad-hoc material dataset[354]; they concluded that HEAs is one of the few class of systems where a substantial spread of results between MLIPs can be observed, and where equivariant NNPs are superior to non-equivariant approaches. Nonetheless, the HEA dataset had been constructed from EAM simulations, which defeats the purpose of employing a NNP in the first place. To the best of our knowledge, there are essentially no comparative studies between state-of-the-art NNPs, such as MACE or DeePMD[355], trained on datasets generated entirely from ab initio calculations. Active learning methods are widely utilized. However, no well-established automated workflow or tool currently exists that can be readily integrated into the training process of MLIPs.

Interfaces remain largely unexplored. Despite the considerable interest in HEAs for catalytic applications and hydrogen-/oxygen-evolution reactions (particularly CoFeNi-based alloys), we could not identify any relevant studies. NNPs have been shown to accurately describe heterogeneous, reactive systems while maintaining good transferability to out-of-distribution configurations, making this a particularly promising area for their application.

A recurring characteristic of the methods reviewed here is their orientation towards configurational averages. The VLA removes occupational fluctuations at the outset, the CPA replaces them with an effective scattering medium, and an SQS or a finite supercell represents only a restricted sample of the accessible local environments. These approximations are often adequate for quantities that vary smoothly with composition, such as equilibrium volume or an averaged elastic modulus. Many properties governing the behaviour of HEAs, however, depend nonlinearly on local chemistry and strain. Vacancy formation and migration energies, solute interaction energies, Peierls barriers, dislocation core structures and local elastic responses are therefore distributions rather than single material constants. The same issue extends to dissipative and transport properties. Green–Kubo coefficients are determined by autocorrelation functions of fluctuating currents, stresses or forces, so their configurational dependence cannot generally be inferred from an averaged structure or averaged interaction. A recent treatment of dissipative dislocation motion showcases this[356]: dislocation drag in HEAs is quadratic in the disorder, so an averaged medium underestimates it systematically, since the square of the mean discards the variance that the mean of the square retains. The frequently reported "role of the local environment" should consequently be expressed in statistical terms, through identification of the moments that enter each observable, their rate of self averaging and quantitative criteria for the regime in which the mean is sufficient.

A second characteristic shared by every method reviewed here is that they are all adiabatic, resting on the Born–Oppenheimer separation with classical nuclei, so that electrons enter only through the ground state energy. This excludes electron-phonon coupling in concentrated disordered alloys, the electronic contributions to dislocation drag and damping, electronic stopping in displacement cascades, and any regime in which electrons and phonons are not in mutual equilibrium. The evidence that these channels are consequential is already in the transport data surveyed above: the Wiedemann–Franz decomposition of κ across Ni to NiCoFeCrMn assigns the dominant reduction to the electronic term[309], and the electron-phonon coupling factor in CrFeCoNi-based solid solutions varies by up to a factor of two with composition[306]. HEAs are a natural testbed for these effects, since disorder scattering and electron-phonon coupling act on comparable scales; nonequilibrium field theoretic treatments of such alloys are, at present, essentially unexplored.

Thus, uncertainty quantification is a methodological priority rather than an afterthought. The chain running from DFT through cluster expansions and machine learned potentials to kinetic Monte Carlo, molecular dynamics and, ultimately, continuum level modelling such as CFD or crystal plasticity is at present assembled without tracking how a few meV/atom in the underlying energetics propagate into a predicted yield strength, ordering temperature or diffusivity; systematic error propagation across the scale bridge is largely absent. Establishing it, and with it an explicit account of how much configurational information each stage discards, would let the modelling chain report calibrated distributions in place of isolated means. Computation can already sample properties across composition space faster than experiment can, and it is this capacity, once the tools are rebuilt around distributions rather than averages, that underwrites the move towards continuous, process scale models and computationally guided experiments considered next.

The natural endpoint of this programme is the transfer of atomistic and configurational information to experimental and material design protocols. Integrated Computational Materials Engineering (ICME) approaches[357] have already been employed in the study of HEAs[358–361]. However, these approaches typically employ data-driven models for rapid screening, empirical thermodynamic or mechanical models for scoring and experimental validation. Hence, they largely bypass first-principle characterization of the alloys, which would rely on atomistic models.

We believe the key to unlocking effective multiscale modelling lies in connecting microscale models with continuum models. Crystal-plasticity finite-element (CPFE), finite-element and extended finite-element methods (FEM/XFEM), and computational fluid dynamics (CFD) operate on lengthscales, thermal gradients and mechanical loads that are comparatively smooth at these scales, and they require lower scale input in a reduced but statistically faithful form: distributions of defect energetics and mobilities for the mechanical response, interfacial and surface energies for problems such as intermetallic formation and reactive wetting in soldering[362,363], and effective reaction and transport parameters for system scale models of catalysis. The tools needed to supply this input now exist. MLIPs deliver near DFT accuracy at molecular dynamics cost, bringing observables that were previously inaccessible across composition space within routine reach, among them stacking fault energy distributions, dislocation core structures and Peierls barriers, grain boundary energies, Green–Kubo thermal conductivities and complete elastic tensors. Combined with active learning and with fine tuned foundation models, this capability is mature enough to change the role of computation in alloy development: property screening across the compositional space can now be performed in silico ahead of synthesis, so that modelling guides experiment rather than rationalising it *post facto*.

High-entropy alloys have attracted significant attention because of their unique combination of several elements, leading to exceptional mechanical, thermal, and chemical properties. This review has explored various modelling approaches, from quantum-level calculations to atomistic simulations and machine learning techniques that aid in understanding and predicting the behaviour of HEAs.

Despite progress, several challenges remain. The vast compositional space of HEAs makes it difficult to identify optimal combinations for specific applications. Traditional experimental methods are time-consuming and resource-intensive when applied to such a broad range of possibilities. Moreover, accurately predicting the phase stability and mechanical properties across different compositions continues to be a complex task.

To address these issues, integrating machine learning with existing modelling techniques offers a promising path forward. Machine learning models can rapidly analyse large datasets to identify patterns and predict properties, thus narrowing down the most promising alloy compositions for experimental validation. Furthermore, developing machine learning-based reactive force fields that bridge different modelling scales can enhance the accuracy of simulations, providing more reliable guidance for experimental efforts. Collaboration between computational scientists and experimentalists is crucial. Modelling can inform experimental design by highlighting promising compositions and processing conditions, while experimental results can, in turn, refine and validate computational models. Establishing open-access databases of experimental and simulation data, protocols, and workflows will further support the development of robust machine learning models.

In summary, while HEAs present complex challenges due to their compositional diversity, the integration of advanced modelling techniques and collaborative efforts between computational and experimental domains

hold the key to unlocking their full potential. Continued research in this direction is essential for the efficient discovery and application of HEAs in various technological fields.

Data availability

No datasets were generated or analysed during the current study.

Received: 15 May 2026; Accepted: 2 September 2026;
Published online: 26 September 2026

References

1. Schweidler, S. et al. High-entropy materials for energy and electronic applications. *Nat. Rev. Mater.* **9**, 266–281 (2024).
2. Nisar, A., Zhang, C., Boesl, B. & Agarwal, A. A perspective on challenges and opportunities in developing high entropy-ultra high temperature ceramics. *Ceram. Int.* **46**, 25845–25853 (2020).
3. Huang Jr, Y., Yeh, J.-W. & Yang, A. C.-M. "High-entropy polymers": a new route of polymer mixing with suppressed phase separation. *Materialia* **15**, 100978 (2021).
4. Li, D. et al. High-entropy electrode materials: synthesis, properties and outlook. *Nano Micro Lett.* **17**, 22 (2025).
5. Yeh, J.-W. et al. Nanostructured high-entropy alloys with multiple principal elements: novel alloy design concepts and outcomes. *Adv. Eng. Mater.* **6**, 299–303 (2004).
6. Cantor, B., Chang, I., Knight, P. & Vincent, A. Microstructural development in equiatomic multicomponent alloys. *Mater. Sci. Eng. A* **375**, 213–218 (2004).
7. Miracle, D. B. & Senkov, O. N. A critical review of high entropy alloys and related concepts. *Acta Mater.* **122**, 448–511 (2017).
8. Ko, J. Y. & Hong, S. I. Microstructural evolution and mechanical performance of carbon-containing CoCrFeMnNi-C high entropy alloys. *J. Alloy. Compd.* **743**, 115–125 (2018).
9. Basu, I. & De Hosson, J. T. M. Strengthening mechanisms in high entropy alloys: fundamental issues. *Scr. Mater.* **187**, 148–156 (2020).
10. Boakye, G. O., Straume, E. O., Gunnarsson, B. G., Kovalov, D. & Karlsdottir, S. N. Corrosion behaviour of HVOF developed MO-based high entropy alloy coating and selected hard coatings for high temperature geothermal applications. *Mater. Des.* **235**, 112431 (2023).
11. Deng, C., Wang, T., Wu, P., Zhu, W. & Dai, S. High entropy materials for catalysis: a critical review of fundamental concepts and applications. *Nano Energy* **120**, 109153 https://doi.org/10.1016/j.nanoen.2023.109153 (2024).
12. Gawel, R., Rogal, Ł & Grzesik, Z. Behaviour of Al, Co, Cr, Ni-based high entropy alloys under high-temperature thermal shock oxidising conditions. *Corros. Sci.* **198**, 110116 (2022).
13. Gromov, V. E., Konovalov, S. V., Ivanov, Y. F. & Osintsev, K. A. Methods of manufacturing the high-entropy alloys. In *Structure and Properties of High-Entropy Alloys*, 1–31 (Springer, 2021).
14. Beyramali Kivy, M., Hong, Y. & Asle Zaeem, M. A review of multi-scale computational modeling tools for predicting structures and properties of multi-principal element alloys. *Metals* **9**, 254 (2019).
15. Widom, M. Modeling the structure and thermodynamics of high-entropy alloys. *J. Mater. Res.* **33**, 2881–2898 (2018).
16. Gorsse, S. & Tancret, F. Current and emerging practices of calphad toward the development of high entropy alloys and complex concentrated alloys. *J. Mater. Res.* **33**, 2899–2923 (2018).
17. Zhang, C. & Yang, Y. The calphad approach for heas: challenges and opportunities. *MRS Bull.* **47**, 158–167 (2022).
18. Ikeda, Y., Grabowski, B. & Körmann, F. Ab initio phase stabilities and mechanical properties of multicomponent alloys: a comprehensive review for high entropy alloys and compositionally complex alloys. *Mater. Charact.* **147**, 464–511 (2019).
19. Ferrari, A. et al. Frontiers in atomistic simulations of high entropy alloys. *J. Appl. Phys.* **128**, 150901 https://doi.org/10.1063/5.0025310 (2020).
20. Zhao, Y. Understanding and design of metallic alloys guided by phase-field simulations. *npj Comput. Mater.* **9**, 94 (2023).
21. Liu, X., Zhang, J. & Pei, Z. Machine learning for high-entropy alloys: progress, challenges and opportunities. *Prog. Mater. Sci.* **131**, 101018 (2023).
22. Jiang, D., Xie, L. & Wang, L. Current application status of multi-scale simulation and machine learning in research on high-entropy alloys. *J. Mater. Res. Technol.* **26**, 1341–1374 (2023).
23. Deshmukh, A. A. & Ranganathan, R. Recent advances in modelling structure-property correlations in high-entropy alloys. *J. Mater. Sci. Technol.* **204**, 127–151 (2025).
24. Toor, Z. S. et al. Computation-and process-based design for advanced structural high-entropy alloy development and analyses: a critical review. *Progr. Mater. Sci.* **155**, 101534 (2025).
25. Strumza, E., Ezersky, V., Brosh, E., Aizenshtein, M. & Hayun, S. A comprehensive study of phase transitions in Al0.5CoCrFeNi high-entropy alloy at intermediate temperatures (400≤T≤900◦C). *J. Alloy. Compd.* **898**, 162955 (2022).
26. Gambaro, S., Fenocchio, L., Valenza, F., Riani, P. & Cacciamani, G. Combined experimental and calphad investigation of equimolar AlCoCrFeNi-X (X = Mo, Ta, W) high-entropy alloys. *Calphad* **85**, 102702 (2024).
27. He, W., Zeng, C., Yang, W., Chen, W. & Ai, Y. Impact of different Cr contents on microstructural evolution and mechanical behaviour of CoCrxCuFeMnNiV high-entropy alloys. *J. Mater. Res. Technol.* **21**, 4577–4590 (2022).
28. Zhang, Y. et al. Microstructures and properties of high-entropy alloys. *Prog. Mater. Sci.* **61**, 1–93 (2014).
29. Yeh, J.-W. Alloy design strategies and future trends in high-entropy alloys. *Jom* **65**, 1759–1771 (2013).
30. Planck, M. *Lectures on the Theory of Thermal Radiation* (Leipzig, 1906).
31. Sheng, G. & Liu, C. T. Phase stability in high entropy alloys: formation of solid-solution phase or amorphous phase. *Prog. Nat. Sci. Mater. Int.* **21**, 433–446 (2011).
32. Takeuchi, A. & Inoue, A. Calculations of mixing enthalpy and mismatch entropy for ternary amorphous alloys. *Mater. Trans., JIM* **41**, 1372–1378 (2000).
33. Guo, S., Hu, Q., Ng, C. & Liu, C. More than entropy in high-entropy alloys: forming solid solutions or amorphous phase. *Intermetallics* **41**, 96–103 (2013).
34. Yang, X. & Zhang, Y. Prediction of high-entropy stabilized solid-solution in multi-component alloys. *Mater. Chem. Phys.* **132**, 233–238 (2012).
35. Senkov, O. & Miracle, D. A new thermodynamic parameter to predict formation of solid solution or intermetallic phases in high entropy alloys. *J. Alloy. Compd.* **658**, 603–607 (2016).
36. Troparevsky, M. C., Morris, J. R., Kent, P. R., Lupini, A. R. & Stocks, G. M. Criteria for predicting the formation of single-phase high-entropy alloys. *Phys. Rev. X* **5**, 011041 (2015).
37. Zhang, Y., Zhou, Y. J., Lin, J. P., Chen, G. L. & Liaw, P. K. Solid-solution phase formation rules for multi-component alloys. *Adv. Eng. Mater.* **10**, 534–538 (2008).
38. Poletti, M. G. & Battezzati, L. Electronic and thermodynamic criteria for the occurrence of high entropy alloys in metallic systems. *Acta Mater.* **75**, 297–306 (2014).
39. Dong, Y., Lu, Y., Jiang, L., Wang, T. & Li, T. Effects of electro-negativity on the stability of topologically close-packed phase in high entropy alloys. *Intermetallics* **52**, 105–109 (2014).
40. Guo, S., Ng, C., Lu, J. & Liu, C. T. Effect of valence electron concentration on stability of fcc or bcc phase in high entropy alloys. *J. Appl. Phys.* **109**, 103505 https://doi.org/10.1063/1.3587228 (2011).
41. Singh, A. K., Kumar, N., Dwivedi, A. & Subramaniam, A. A geometrical parameter for the formation of disordered solid

solutions in multi-component alloys. *Intermetallics* **53**, 112–119 (2014).
42. Martin, P. et al. Heaps: a user-friendly tool for the design and exploration of high-entropy alloys based on semi-empirical parameters. *Comput. Phys. Commun.* **278**, 108398 (2022).
43. Nordheim, L. Zur elektronentheorie der metalle. i. *Ann. der Phys.* **401**, 607–640 (1931).
44. Nordheim, L. Zur elektronentheorie der metalle. i. *Ann. der Phys.* **9**, 607–640 (1931).
45. Bellaiche, L. & Vanderbilt, D. Virtual crystal approximation revisited: application to dielectric and piezoelectric properties of perovskites. *Phys. Rev. B* **61**, 7877–7882 (2000).
46. Ramer, N. J. & Rappe, A. M. Virtual-crystal approximation that works: Locating a compositional phase boundary in $Pb(Zr_{1-x}Ti_x)O_3$. *Phys. Rev. B* **62**, R743–R746 (2000).
47. Li, T., Morris, J. W., Nagasako, N., Kuramoto, S. & Chrzan, D. C. "Ideal" engineering alloys. *Phys. Rev. Lett.* **98**, 105503 (2007).
48. Qi, L. & Chrzan, D. C. Tuning ideal tensile strengths and intrinsic ductility of bcc refractory alloys. *Phys. Rev. Lett.* **112**, 115503 (2014).
49. Mu, Y. et al. An ab initio and experimental studies of the structure, mechanical parameters and state density on the refractory high-entropy alloy systems. *J. Alloy. Compd.* **714**, 668–680 (2017).
50. Shi, W. et al. First-principles calculation of phase stability and elastic properties of Cr_xMONbTiV refractory high-entropy alloys. *AIP Adv.* **13**, 095222 (2023).
51. Chen, L., Hao, X., Wang, Y., Zhang, X. & Liu, H. First-principles calculation of the effect of ti content on the structure and properties of TiVNbMo refractory high-entropy alloy. *Mater. Res. Express* **7**, 106516 (2020).
52. Tian, F., Wang, D., Shen, J. & Wang, Y. An ab initio investgation of ideal tensile and shear strength of TiVNbMo high-entropy alloy. *Mater. Lett.* **166**, 271–275, https://doi.org/10.1016/j.matlet.2015.12.064 (2016).
53. Wang, Q., Li, Q., Ding, H. & Tian, F. Elastic properties of solid-solution refractory metal carbides with vacancy from virtual crystal approximation and supercell method. *Comput. Condens. Matter* **32**, e00721 (2022).
54. Wang, S. et al. Comparison of two calculation models for high entropy alloys: virtual crystal approximation and special quasi-random structure. *Mater. Lett.* **282**, 128754 (2021).
55. Soven, P. Coherent-potential model of substitutional disordered alloys. *Phys. Rev.* **156**, 809–813 (1967).
56. Gyorffy, B. Coherent-potential approximation for a nonoverlapping-muffin-tin-potential model of random substitutional alloys. *Phys. Rev. B* **5**, 2382 (1972).
57. Johnson, R. A. Alloy models with the embedded-atom method. *Phys. Rev. B* **39**, 12554–12559 (1989).
58. Ebert, H., Koedderitzsch, D. & Minar, J. Calculating condensed matter properties using the KKR-Green's function method-recent developments and applications. *Rep. Prog. Phys.* **74**, 096501 (2011).
59. Singh, P., Smirnov, A. V. & Johnson, D. D. Atomic short-range order and incipient long-range order in high-entropy alloys. *Phys. Rev. B* **91**, 224204 (2015).
60. Singh, P., Smirnov, A. V. & Johnson, D. D. Ta-Nb-Mo-W refractory high-entropy alloys: anomalous ordering behavior and its intriguing electronic origin. *Phys. Rev. Mater.* **2**, 055004 (2018).
61. Woodgate, C. D. & Staunton, J. B. Short-range order and compositional phase stability in refractory high-entropy alloys via first-principles theory and atomistic modeling: NbMoTa, NbMoTaW, and VNbMoTaW. *Phys. Rev. Mater.* **7**, 013801 (2023).
62. Woodgate, C. D., Marchant, G. A., Pártay, L. B. & Staunton, J. B. Structure, short-range order, and phase stability of the Al_xCrFeCoNi high-entropy alloy: insights from a perturbative, DFT-based analysis. *npj Comput. Mater.* **10**, 271 (2024).
63. Woodgate, C. D. & Staunton, J. B. Competition between phase ordering and phase segregation in the Ti_xNbMoTaW and Ti_xVNbMoTaW refractory high-entropy alloys. *J. Appl. Phys.* **135**, 135106 (2024).
64. Woodgate, C. D., Naguszewski, H. J., Redka, D. et al. Emergent b2 chemical orderings in the AlTiVNb and AlTiCrMo refractory high-entropy superalloys studied via first-principles theory and atomistic modelling. *J. Phys. Mater.* **8**, 045002 (2025).
65. Jarrell, M. & Krishnamurthy, H. R. Systematic and causal corrections to the coherent potential approximation. *Phys. Rev. B* **63**, 125102 (2001).
66. Rowlands, D. A., Staunton, J. B. & Györffy, B. L. Korringa-Kohn-Rostoker nonlocal coherent-potential approximation. *Phys. Rev. B* **67**, 115109 (2003).
67. Biava, D. A., Ghosh, S., Johnson, D. D., Shelton, W. A. & Smirnov, A. V. Systematic, multisite short-range-order corrections to the electronic structure of disordered alloys from first principles: the KKR nonlocal CPA from the dynamical cluster approximation. *Phys. Rev. B* **72**, 113105 (2005).
68. Mondal, W. R., Vidhyadhiraja, N. S., Berlijn, T., Moreno, J. & Jarrell, M. Localization of phonons in mass-disordered alloys: a typical medium dynamical cluster approach. *Phys. Rev. B* **96**, 014203 (2017).
69. Mondal, W. R., Berlijn, T., Jarrell, M. & Vidhyadhiraja, N. S. Phonon localization in binary alloys with diagonal and off-diagonal disorder: a cluster Green's function approach. *Phys. Rev. B* **99**, 134203 (2019).
70. Mondal, W. R. & Vidhyadhiraja, N. S. Effect of short-ranged spatial correlations on the anderson localization of phonons in mass-disordered systems. *Bull. Mater. Sci.* **43**, 314 (2020).
71. Mondal, W. R., Berlijn, T., Vidhyadhiraja, N. S. & Terletska, H. Typical medium cluster approach for multibranch phonon localization. *Phys. Rev. B* **113**, 064203 (2026).
72. Niu, C., Zaddach, A., Koch, C. & Irving, D. First principles exploration of near-equiatomic NiFeCrCo high entropy alloys. *J. Alloy. Compd.* **672**, 510–520 (2016).
73. Raghuraman, V., Wang, Y. & Widom, M. An investigation of high entropy alloy conductivity using first-principles calculations. *Appl. Phys. Lett.* **119**, 121903 (2021).
74. Tian, F., Varga, L. K., Chen, N., Delczeg, L. & Vitos, L. Ab initio investigation of high-entropy alloys of 3 d elements. *Phys. Rev. B Condens. Matter Mater. Phys.* **87**, 075144 (2013).
75. Woodgate, C. D. & Staunton, J. B. Compositional phase stability in medium-entropy and high-entropy Cantor-Wu alloys from an ab initio all-electron Landau-type theory and atomistic modeling. *Phys. Rev. B* **105**, 115124 (2022).
76. Woodgate, C. D. et al. Emergent b2 chemical orderings in the AlTiVNb and AlTiCrMo refractory high-entropy superalloys studied via first-principles theory and atomistic modelling. *J. Phys. Mater.* **8**, 045002 (2025).
77. Woodgate, C. D., Hedlund, D., Lewis, L. H. & Staunton, J. B. Interplay between magnetism and short-range order in medium- and high-entropy alloys: CrCoNi, CrFeCoNi, and CrMnFeCoNi. *Phys. Rev. Mater.* **7**, 053801 (2023).
78. Shenoy, L. et al. Collinear-spin machine learned interatomic potential for Fe_7Cr_2Ni alloy. *Phys. Rev. Mater.* **8**, 033804 (2024).
79. Pólya, G. & Read, R. C. *Combinatorial Enumeration of Groups, Graphs, and Chemical Compounds* (Springer, 2012).
80. Hart, G. L. & Forcade, R. W. Algorithm for generating derivative structures. *Phys. Rev. B* **77**, 224115 (2008).
81. Hart, G. L. & Forcade, R. W. Generating derivative structures from multilattices: algorithm and application to hcp alloys. *Phys. Rev. B* **80**, 014120 (2009).
82. van de Walle, A. & Ceder, G. Automating first-principles phase diagram calculations. *J. Phase Equilib.* **23**, 348 (2002).

83. van de Walle, A. et al. Efficient stochastic generation of special quasirandom structures. *Calphad* **42**, 13–18 (2013).
84. Ångqvist, M. et al. ICET – a python library for constructing and sampling alloy cluster expansions. *Adv. Theory Simul.* **2**, 1900015 (2019).
85. Zunger, A., Wei, S.-H., Ferreira, L. G. & Bernard, J. E. Special quasirandom structures. *Phys. Rev. Lett.* **65**, 353 (1990).
86. Wei, S.-H., Ferreira, L., Bernard, J. E. & Zunger, A. Electronic properties of random alloys: special quasirandom structures. *Phys. Rev. B* **42**, 9622 (1990).
87. Jiang, C., Wolverton, C., Sofo, J., Chen, L.-Q. & Liu, Z.-K. First-principles study of binary bcc alloys using special quasirandom structures. *Phys. Rev. B-Condens. Matter Mater. Phys.* **69**, 214202 (2004).
88. Troparevsky, M. C. et al. Beyond atomic sizes and Hume-Rothery rules: understanding and predicting high-entropy alloys. *Jom* **67**, 2350–2363 (2015).
89. Feng, R., Liaw, P. K., Gao, M. C. & Widom, M. First-principles prediction of high-entropy-alloy stability. *npj Comput. Mater.* **3**, 50 (2017).
90. Wang, S., Zhang, T., Hou, H. & Zhao, Y. The magnetic, electronic, and thermodynamic properties of high entropy alloy CrMnFeCoNi: a first-principles study. *Phys. Status Solidi* **255**, 1800306 (2018).
91. Roy, I., Ekuma, C. & Balasubramanian, G. Examining the thermodynamic stability of mixed principal element oxides in AlCoCrFeNi high-entropy alloy by first-principles. *Comput. Mater. Sci.* **213**, 111619 (2022).
92. Yang, S. & Zhong, Y. Ab initio modeling of fcc Fe-Co-Cr-Ni high entropy alloys with full composition range. *J. Phase Equilib. Diffus.* **42**, 656–672 (2021).
93. Kumar, N. & Waghmare, U. V. Entropic stabilization and descriptors of structural transformation in high entropy alloys. *Acta Mater.* **255**, 119077 (2023).
94. Rogal, L. et al. Computationally-driven engineering of sublattice ordering in a hexagonal AlHfScTiZr high entropy alloy. *Sci. Rep.* **7**, 2209 (2017).
95. Karabin, M. et al. Ab initio approaches to high-entropy alloys: a comparison of CPA, SQS, and supercell methods. *J. Mater. Sci.* **57**, 10677–10690 (2022).
96. Tian, L. Y. et al. Elastic constants of random solid solutions by sqs and cpa approaches: the case of fcc Ti-Al. *J. Phys. Condens. Matter* **27**, 315702 (2015).
97. Tian, F., Varga, L. K., Shen, J. & Vitos, L. Calculating elastic constants in high-entropy alloys using the coherent potential approximation: current issues and errors. *Comput. Mater. Sci.* **111**, 350–358 (2016).
98. Ghosh, S., Sotskov, V., Shapeev, A. V., Neugebauer, J. & Körmann, F. Short-range order and phase stability of CrCoNi explored with machine learning potentials. *Phys. Rev. Mater.* **6**, 113804 https://doi.org/10.1103/PhysRevMaterials.6.113804 (2022).
99. Ferrari, A., Körmann, F., Asta, M. & Neugebauer, J. Simulating short-range order in compositionally complex materials. *Nat. Comput. Sci.* **3**, 221–229 (2023).
100. Abrikosov, I., Ruban, A., Johansson, B. & Skriver, H. L. Total energy calculations of random alloys: Supercell, Connolly-Williams, and CPA methods. *Comput. Mater. Sci.* **10**, 302–305 (1998).
101. Tian, F. A review of solid-solution models of high-entropy alloys based on ab initio calculations. *Front. Mater.* **4**, 36 (2017).
102. Lejaeghere, K., Van Speybroeck, V., Van Oost, G. & Cottenier, S. Error estimates for solid-state density-functional theory predictions: an overview by means of the ground-state elemental crystals. *Crit. Rev. Solid State Mater. Sci.* **39**, 1–24 (2014).
103. Bartel, C. J., Weimer, A. W., Lany, S., Musgrave, C. B. & Holder, A. M. The role of decomposition reactions in assessing first-principles predictions of solid stability. *npj Comput. Mater.* **5**, 4 (2019).
104. Wang, A. et al. A framework for quantifying uncertainty in DFT energy corrections. *Sci. Rep.* **11**, 15496 (2021).
105. Car, R. & Parrinello, M. Unified approach for molecular dynamics and density-functional theory. *Phys. Rev. Lett.* **55**, 2471–2474 (1985).
106. Kresse, G. & Hafner, J. Ab initio molecular dynamics for liquid metals. *Phys. Rev. B* **47**, 558–561 (1993).
107. Payne, M. C., Teter, M. P., Allan, D. C., Arias, T. A. & Joannopoulos, J. D. Iterative minimization techniques for ab initio total-energy calculations: molecular dynamics and conjugate gradients. *Rev. Mod. Phys.* **64**, 1045–1097 (1992).
108. Zhou, W. et al. Amorphization evolution study of CrCoFeNiMn high entropy alloy for mechanical performance optimization by deep potential molecular dynamics. *npj Comput. Mater.* **11**, 69 (2025).
109. Ma, D., Grabowski, B., Körmann, F., Neugebauer, J. & Raabe, D. Ab initio thermodynamics of the CoCrFeMnNi high entropy alloy: importance of entropy contributions beyond the configurational one. *Acta Mater.* **100**, 90–97 (2015).
110. Chen, H. et al. Lattice distortion tuning resistivity invar effect in high-entropy alloys. *Phys. Rev. B* **111**, 094209 (2025).
111. Ding, J., Asta, M. & Ritchie, R. O. Melts of CrCoNi-based high-entropy alloys: atomic diffusion and electronic/atomic structure from ab initio simulation. *Appl. Phys. Lett.* **113**, 111902 (2018).
112. Widom, M., Huhn, W. P., Maiti, S. & Steurer, W. Hybrid Monte Carlo/molecular dynamics simulation of a refractory metal high entropy alloy. *Metall. Mater. Trans. A* **45**, 196–200 (2014).
113. Arnold, J. et al. Thermodynamics and phase stability of the AlTiCrMoW high-entropy alloy simulated using machine-learned interatomic potentials. *Phys. Rev. Mater.* **10**, 073605 (2026).
114. Sanchez, J. M., Ducastelle, F. & Gratias, D. Generalized cluster description of multicomponent systems. *Phys. A Stat. Mech. Appl.* **128**, 334–350 (1984).
115. Fernández-Caballero, A., Wróbel, J. S., Mummery, P. M. & Nguyen-Manh, D. Short-range order in high entropy alloys: theoretical formulation and application to Mo-Nb-Ta-V-W system. *J. Phase Equilib. Diffus.* **38**, 391–403 (2017).
116. Huhn, W. P. & Widom, M. Prediction of A2 to B2 phase transition in the high entropy alloy Mo Nb Ta W. *JOM* **65**, 1772–1779 (2013).
117. Nataraj, C. M., van de Walle, A. & Samanta, A. Temperature-dependent configurational entropy calculations for refractory high-entropy alloys. *J. Phase Equilib. Diffus.* **42**, 571–577 (2021).
118. Skilling, J. Nested sampling for general bayesian computation. *Bayesian Anal.* **1**, 833–859 (2006).
119. Pártay, L. B., Bartók, A. P. & Csányi, G. Efficient sampling of atomic configurational spaces. *J. Phys. Chem. B* **114**, 10502–10512 (2010).
120. Pártay, L. B. Nested sampling for materials. *Eur. Phys. J. B* **94**, 159 (2021).
121. Baldock, R. J. N., Pártay, L. B., Bartók, A. P., Payne, M. C. & Csányi, G. Determining pressure-temperature phase diagrams of materials. *Phys. Rev. B* **93**, 174108 (2016).
122. Unglert, N., Carbogno, C., Scheffler, M. & Rossi, M. Neural-network force field backed nested sampling: study of the silicon pressure-temperature phase diagram. *Phys. Rev. Mater.* **7**, 123804 (2023).
123. Naguszewski, H. J., Pártay, L. B., Quigley, D. & Woodgate, C. D. Brawl: simulating the thermodynamics and phase stability of multicomponent alloys using conventional and enhanced sampling techniques. *J. Open Source Softw.* **10**, 8346 (2025).
124. Daw, M. S. & Baskes, M. I. Embedded-atom method: derivation and application to impurities, surfaces, and other defects in metals. *Phys. Rev. B* **29**, 6443–6453 (1984).
125. Daw, M. S., Foiles, S. M. & Baskes, M. I. The embedded-atom method: a review of theory and applications. *Mater. Sci. Rep.* **9**, 251–310 (1993).
126. Finnis, M. W. & Sinclair, J. E. A simple empirical N-body potential for transition metals. *Philos. Mag. A* **50**, 45–55 https://doi.org/10.1080/01418618408244210 (1984).

127. Baskes, M. I. Application of the embedded-atom method to covalent materials: a semiempirical potential for silicon. *Phys. Rev. Lett.* **59**, 2666–2669 (1987).
128. Baskes, M. I. Modified embedded-atom potentials for cubic materials and impurities. *Phys. Rev. B* **46**, 2727–2742 (1992).
129. Lee, B.-J. & Baskes, M. I. Second nearest-neighbor modified embedded-atom-method potential. *Phys. Rev. B* **62**, 8564–8567 (2000).
130. Kim, E. H., Shin, Y.-H. & Lee, B.-J. A modified embedded-atom method interatomic potential for germanium. *Calphad* **32**, 34–42 (2008).
131. Foiles, S. M., Baskes, M. I. & Daw, M. S. Embedded-atom-method functions for the fcc metals Cu, Ag, Au, Ni, Pd, Pt, and their alloys. *Phys. Rev. B* **33**, 7983–7991 (1986).
132. Almandoz, E. et al. CrAlON CAE-PVD coatings for oxidation and wear protection of TZM alloys in FAST sintering applications. *Mater. Chem. Phys.* **208**, 189–197 (2018).
133. Tao, X. et al. Active screen plasma nitriding of a Si-alloyed FeCrNi medium entropy alloy: high interstitial absorption and an anomalous Si-induced decomposition mechanism in N-expanded austenite. *Appl. Surf. Sci.* **624**, 157137 (2023).
134. Gild, J. et al. High-entropy metal diborides: a new class of high-entropy materials and a new type of ultrahigh temperature ceramics. *Sci. Rep.* **6**, 37946 (2016).
135. Luo, T. et al. Mechanical and damping properties of the multi-layer graphenes enhanced CrMnFeCoNi high-entropy alloy composites produced by powder metallurgy. *Mater. Lett.* **293**, 129682 (2021).
136. Zhou, X. W., Wadley, H. N. G., Filhol, J.-S. & Neurock, M. N. Modified charge transfer–embedded atom method potential for metal/metal oxide systems. *Phys. Rev. B* **69**, 035402 (2004).
137. Lee, B.-J., Lee, T.-H. & Kim, S.-J. A modified embedded-atom method interatomic potential for the Fe-N system: a comparative study with the Fe-C system. *Acta Mater.* **54**, 4597–4607 (2006).
138. Kim, Y.-M. & Lee, B.-J. Modified embedded-atom method interatomic potentials for the Ti-C and Ti-N binary systems. *Acta Mater.* **56**, 3481–3489 (2008).
139. Stillinger, F. H. & Weber, T. A. Computer simulation of local order in condensed phases of silicon. *Phys. Rev. B* **31**, 5262–5271 (1985).
140. Vashishta, P., Kalia, R. K., Rino, J. P. & Ebbsjö, I. Interaction potential for SiO_2: a molecular-dynamics study of structural correlations. *Phys. Rev. B* **41**, 12197–12209 (1990).
141. Cruz-Chu, E. R., Aksimentiev, A. & Schulten, K. Water-silica force field for simulating nanodevices. *J. Phys. Chem. B* **110**, 21497–21508 (2006).
142. Abell, G. C. Empirical chemical pseudopotential theory of molecular and metallic bonding. *Phys. Rev. B* **31**, 6184–6196 (1985).
143. Tersoff, J. New empirical approach for the structure and energy of covalent systems. *Phys. Rev. B* **37**, 6991–7000 (1988).
144. Stuart, S. J., Tutein, A. B. & Harrison, J. A. A reactive potential for hydrocarbons with intermolecular interactions. *J. Chem. Phys.* **112**, 6472–6486 (2000).
145. van Duin, A. C. T., Dasgupta, S., Lorant, F. & Goddard, W. A. Reaxff: a reactive force field for hydrocarbons. *J. Phys. Chem. A* **105**, 9396–9409 (2001).
146. Yu, J., Sinnott, S. B. & Phillpot, S. R. Charge optimized many-body potential for the Si/SiO_2 system. *Phys. Rev. B* **75**, 085311 (2007).
147. Xiao, J.-K., Tan, H., Chen, J., Martini, A. & Zhang, C. Effect of carbon content on microstructure, hardness and wear resistance of CoCrFeMnNiCx high-entropy alloys. *J. Alloy. Compd.* **847**, 156533 (2020).
148. Xie, H., Ma, Z., Zhang, W., Zhao, H. & Ren, L. Strengthening effect of high-entropy alloys endowed by monolayer graphene. *Mater. Today Phys.* **27**, 100800 (2022).
149. Song, W.-X. & Zhao, S.-J. Development of the reaxff reactive force field for aluminum-molybdenum alloy. *J. Mater. Res.* **28**, 1155–1164 (2013).
150. Antony, A. C. et al. Charge optimized many body (COMB) potentials for Pt and Au. *J. Phys. Condens. Matter* **29**, 225901 (2017).
151. Bonn, D., Eggers, J., Indekeu, J., Meunier, J. & Rolley, E. Wetting and spreading. *Rev. Mod. Phys.* **81**, 739–805 (2009).
152. Kim, J. Review of nucleate pool boiling bubble heat transfer mechanisms. *Int. J. Multiph. Flow.* **35**, 1067–1076 (2009).
153. Liu, K. et al. Effects of phosphate additives on the wetting and corrosion resistance of high-chrome refractory materials to two slags. *Ceram. Int.* **49**, 8155–8164 (2023).
154. Webb, E. B., Grest, G. S. & Heine, D. R. Precursor film controlled wetting of Pb on Cu. *Phys. Rev. Lett.* **91**, 236102 (2003).
155. Guo, W., Ma, K., Wang, Q. & Xue, H. The wetting of Pb droplet on the solid Al surface can be promoted by ultrasonic vibration - molecular dynamics simulation. *Mater. Lett.* **264**, 127118 (2020).
156. Chen, J., Nokelainen, J., Barbiellini, B. & Yeddu, H. K. Nanoscale phenomena during wetting of copper on nickel-based superalloy: a molecular dynamics study. *Comput. Mater. Sci.* **230**, 112453 (2023).
157. Qu, J. et al. Molecular dynamics and first-principles calculations on the wetting behavior and mechanism of molten al on nickel-infiltrated steel: a cross-scale simulation. *Comput. Mater. Sci.* **233**, 112719 (2024).
158. Li, Y., Wang, H., Weng, L., Tu, B. & Lei, M. Wetting and spreading of AgCuTi on Fe substrate at high temperatures: a molecular dynamics study. *J. Mater. Res. Technol.* **27**, 5783–5790 (2023).
159. Ruan, M. et al. Preparation and anti-icing behavior of superhydrophobic surfaces on aluminum alloy substrates. *Langmuir* **29**, 8482–8491 (2013).
160. Zhao, Y. et al. High-entropy materials for water splitting: an atomic nanoengineering approach to sustainable hydrogen production. *Adv. Mater.* **37**, 2506117 (2025).
161. Nguyen, C. T., Barisik, M. & Kim, B. Wetting of chemically heterogeneous striped surfaces: molecular dynamics simulations. *AIP Adv.* **8**, 065003 (2018).
162. Wu, N., Zeng, L., Fu, T., Wang, Z. & Lu, C. Molecular dynamics study of rapid boiling of thin liquid water film on smooth copper surface under different wettability conditions. *Int. J. Heat. Mass Transf.* **147**, 118905 (2020).
163. Carrasco, J., Hodgson, A. & Michaelides, A. A molecular perspective of water at metal interfaces. *Nat. Mater.* **11**, 667–674 (2012).
164. Spohr, E. & Heinzinger, K. Molecular dynamics simulation of a water/metal interface. *Chem. Phys. Lett.* **123**, 218–221 (1986).
165. Heinzinger, K. & Spohr, E. Computer simulations of water-metal interfaces. *Electrochim. Acta* **34**, 1849–1856 (1989).
166. Siepmann, J. I. & Sprik, M. Influence of surface topology and electrostatic potential on water/electrode systems. *J. Chem. Phys.* **102**, 511–524 (1995).
167. Willard, A. P., Reed, S. K., Madden, P. A. & Chandler, D. Water at an electrochemical interface-a simulation study. *Faraday Discuss.* **141**, 423–441 (2009).
168. Fernandes, F., Campos, T., Cividanes, L., Simonetti, E. & Thim, G. Adsorbed water on iron surface by molecular dynamics. *Appl. Surf. Sci.* **362**, 70–78 (2016).
169. Martinez, J., Liang, T., Sinnott, S. B. & Phillpot, S. R. A third-generation charge optimized many body (COMB3) potential for nitrogen-containing organic molecules. *Comput. Mater. Sci.* **139**, 153–161 (2017).
170. Antony, A. C., Liang, T. & Sinnott, S. B. Nanoscale structure and dynamics of water on Pt and Cu surfaces from MD simulations. *Langmuir* **34**, 11905–11911 (2018).
171. Gim, S., Cho, K. J., Lim, H.-K. & Kim, H. Structure, dynamics, and wettability of water at metal interfaces. *Sci. Rep.* **9**, 14805 (2019).
172. Gim, S., Lim, H.-K. & Kim, H. Multiscale simulation method for quantitative prediction of surface wettability at the atomistic level. *J. Phys. Chem. Lett.* **9**, 1750–1758 (2018).

173. Natarajan, S. K. & Behler, J. Neural network molecular dynamics simulations of solid-liquid interfaces: water at low-index copper surfaces. *Phys. Chem. Chem. Phys.* **18**, 28704–28725 (2016).
174. Unke, O. T. et al. Machine learning force fields. *Chem. Rev.* **121**, 10142–10186 (2021).
175. Jain, A. et al. Commentary: The materials project: a materials genome approach to accelerating materials innovation. *APL Mater.* **1**, 011002 (2013).
176. Materials project trajectory (MPtrj) dataset. https://doi.org/10.6084/m9.figshare.23713842 (2024).
177. Choudhary, K. et al. The joint automated repository for various integrated simulations (JARVIS) for data-driven materials design. *npj Comput. Mater.* **6**, 173 (2020).
178. Scheidgen, M. et al. Nomad: a distributed web-based platform for managing materials science research data. *J. Open Source Softw.* **8**, 5388 (2023).
179. Rosen, A. S. et al. Machine learning the quantum-chemical properties of metal-organic frameworks for accelerated materials discovery. *Matter* **4**, 1578–1597 (2021).
180. Barros-Luque, L. et al. The open materials 2024 (OMat24) inorganic materials dataset and models. *Nat. Comput. Sci.* **6**, 642–652 https://doi.org/10.1038/s43588-026-00996-w (2026).
181. Tran, R. et al. The open catalyst 2022 (OC22) dataset and challenges for oxide electrocatalysts. *ACS Catal.* **13**, 3066–3084 (2023).
182. Behler, J. & Parrinello, M. Generalized neural-network representation of high-dimensional potential-energy surfaces. *Phys. Rev. Lett.* **98**, 146401 (2007).
183. Lechner, W. & Dellago, C. Accurate determination of crystal structures based on averaged local bond order parameters. *J. Chem. Phys.* **129**, 114707 (2008).
184. Bartók, A. P., Kondor, R. & Csányi, G. On representing chemical environments. *Phys. Rev. B* **87**, 184115 (2013).
185. Drautz, R. Atomic cluster expansion for accurate and transferable interatomic potentials. *Phys. Rev. B* **99**, 014104 (2019).
186. Bartók, A. P., Payne, M. C., Kondor, R. & Csányi, G. Gaussian approximation potentials: the accuracy of quantum mechanics, without the electrons. *Phys. Rev. Lett.* **104**, 136403 (2010).
187. Deringer, V. L. et al. Gaussian process regression for materials and molecules. *Chem. Rev.* **121**, 10073–10141 (2021).
188. Klawohn, S. et al. Gaussian approximation potentials: theory, software implementation and application examples. *J. Chem. Phys.* **159**, 174108 (2023).
189. Batzner, S. et al. E(3)-equivariant graph neural networks for data-efficient and accurate interatomic potentials. *Nat. Commun.* **13**, 2453 (2022).
190. Musaelian, A. et al. Learning local equivariant representations for large-scale atomistic dynamics. *Nat. Commun.* **14**, 579 (2023).
191. Kostiuchenko, T., Körmann, F., Neugebauer, J. & Shapeev, A. Impact of lattice relaxations on phase transitions in a high-entropy alloy studied by machine-learning potentials. *npj Comput. Mater.* **5**, 55 https://doi.org/10.1038/s41524-019-0195-y (2019).
192. Ghosh, S., Ueltzen, K., George, J., Neugebauer, J. & Körmann, F. Chemical ordering and magnetism in face-centered cubic CrCoNi alloy. *npj Comput. Mater.* **10**, 284 https://doi.org/10.1038/s41524-024-01439-8 (2024).
193. Choudhary, K. & DeCost, B. Atomistic line graph neural network for improved materials property predictions. *npj Comput. Mater.* **7**, 185 (2021).
194. Li, K., Choudhary, K., DeCost, B., Greenwood, M. & Hattrick-Simpers, J. Efficient first principles based modeling via machine learning: from simple representations to high entropy materials. *J. Mater. Chem. A* **12**, 12412–12422 (2024).
195. Batatia, I., Kovacs, D. P., Simm, G., Ortner, C. & Csányi, G. Mace: higher order equivariant message passing neural networks for fast and accurate force fields. *Adv. Neural Inf. Process. Syst.* **35**, 11423–11436 (2022).
196. Batatia, I. et al. The design space of E(3)-equivariant atom-centred interatomic potentials. *Nat. Mach. Intell.* **7**, 56–67 (2025).
197. Bernstein, N. From gap to ace to mace https://kimreview.org/commentaries/10-25950-67c762ea/ (2024).
198. Batatia, I. et al. A foundation model for atomistic materials chemistry. *J. Chem. Phys.* **163**, 184110 (2025).
199. Lopanitsyna, N., Fraux, G., Springer, M. A., De, S. & Ceriotti, M. Modeling high-entropy transition metal alloys with alchemical compression. *Phys. Rev. Mater.* **7**, 045802 (2023).
200. Mazitov, A. et al. Surface segregation in high-entropy alloys from alchemical machine learning. *J. Phys. Mater.* **7**, 025007 (2024).
201. Böselt, L., Thürlemann, M. & Riniker, S. Machine learning in QM/MM molecular dynamics simulations of condensed-phase systems. *J. Chem. Theory Comput.* **17**, 2641–2658 (2021).
202. Gastegger, M., Schütt, K. T. & Müller, K.-R. Machine learning of solvent effects on molecular spectra and reactions. *Chem. Sci.* **12**, 11473–11483 (2021).
203. Galvelis, R. et al. NNP/MM: accelerating molecular dynamics simulations with machine learning potentials and molecular mechanics. *J. Chem. Inf. Model.* **63**, 5701–5708 (2023).
204. Grassano, J. S. et al. Assessment of embedding schemes in a hybrid machine learning/classical potentials (ML/MM) approach. *J. Chem. Inf. Model.* **64**, 4047–4058 (2024).
205. Zinovjev, K. et al. emle-engine: A flexible electrostatic machine learning embedding package for multiscale molecular dynamics simulations. *J. Chem. Theory Comput.* **20**, 4514–4522 (2024).
206. Ghasemi, S. A., Hofstetter, A., Saha, S. & Goedecker, S. Interatomic potentials for ionic systems with density functional accuracy based on charge densities obtained by a neural network. *Phys. Rev. B* **92**, 045131 (2015).
207. Grisafi, A. & Ceriotti, M. Incorporating long-range physics in atomic-scale machine learning. *J. Chem. Phys.* **151**, 204105 (2019).
208. Ko, T. W., Finkler, J. A., Goedecker, S. & Behler, J. A fourth-generation high-dimensional neural network potential with accurate electrostatics including non-local charge transfer. *Nat. Commun.* **12**, 398 (2021).
209. Yang, M., Bonati, L., Polino, D. & Parrinello, M. Using metadynamics to build neural network potentials for reactive events: the case of urea decomposition in water. *Catal. Today* **387**, 143–149 (2022).
210. Singh, R., Sharma, A., Singh, P., Balasubramanian, G. & Johnson, D. D. Accelerating computational modeling and design of high-entropy alloys. *Nat. Comput. Sci.* **1**, 54–61 https://doi.org/10.1038/s43588-020-00006-7 (2021).
211. Young, W. M. & Elcock, E. W. Monte Carlo studies of vacancy migration in binary ordered alloys: I. *Proc. Phys. Soc.* **89**, 735–746 (1966).
212. Bortz, A. B., Kalos, M. H. & Lebowitz, J. L. A new algorithm for Monte Carlo simulation of ising spin systems. *J. Comput. Phys.* **17**, 10–18 (1975).
213. Battaile, C. C. The kinetic Monte Carlo method: foundation, implementation, and application. *Comput. Methods Appl. Mech. Eng.* **197**, 3386–3398 (2008).
214. Voter, A. F. Introduction to the kinetic Monte Carlo method. In *Radiation Effects in Solids*, vol.235 of *NATO Science Series* (eds Sickafus, K. E., Kotomin, E. A. & Uberuaga, B. P.) 1–23 (Springer, 2007).
215. Van der Ven, A., Ceder, G., Asta, M. & Tepesch, P. D. First-principles theory of ionic diffusion with nondilute carriers. *Phys. Rev. B* **64**, 184307 (2001).
216. Van der Ven, A., Yu, H.-C., Ceder, G. & Thornton, K. Vacancy mediated substitutional diffusion in binary crystalline solids. *Prog. Mater. Sci.* **55**, 61–105 (2010).

217. Béland, L. K., Brommer, P., El-Mellouhi, F., Joly, J.-F. & Mousseau, N. Kinetic activation-relaxation technique. *Phys. Rev. E* **84**, 046704 (2011).
218. Xu, H., Osetsky, Y. N. & Stoller, R. E. Simulating complex atomistic processes: on-the-fly kinetic monte carlo scheme with selective active volumes. *Phys. Rev. B* **84**, 132103 (2011).
219. Xing, B., Rupert, T. J., Pan, X. & Cao, P. Neural network kinetics for exploring diffusion multiplicity and chemical ordering in compositionally complex materials. *Nat. Commun.* **15**, 3941 (2024).
220. Osetsky, Y. N., Béland, L. K. & Stoller, R. E. Specific features of defect and mass transport in concentrated fcc alloys. *Acta Mater.* **115**, 364–371 (2016).
221. Osetsky, Y. N., Béland, L. K., Barashev, A. V. & Zhang, Y. On the existence and origin of sluggish diffusion in chemically disordered concentrated alloys. *Curr. Opin. Solid State Mater. Sci.* **22**, 65–74 (2018).
222. Zhao, S., Osetsky, Y. N. & Zhang, Y. Preferential diffusion in concentrated solid solution alloys: NiFe, NiCo and NiCoCr. *Acta Mater.* **128**, 391–399 (2017).
223. Osetsky, Y. N., Barashev, A. V., Béland, L. K. & Zhang, Y. Tunable chemical complexity to control atomic diffusion in alloys. *npj Comput. Mater.* **6**, 38 (2020).
224. Shen, Z. et al. Kinetic monte carlo simulation framework for chemical short range order formation kinetics in a multi principal element alloy. *Comput. Mater. Sci.* **198**, 110670 (2021).
225. Xing, B., Wang, X., Bowman, W. J. & Cao, P. Short range order localizing diffusion in multi principal element alloys. *Scr. Mater.* **210**, 114450 (2022).
226. Li, Y., Du, J.-P., Shinzato, S. & Ogata, S. Tunable interstitial and vacancy diffusivity by chemical ordering control in CrCoNi medium entropy alloy. *npj Comput. Mater.* **10**, 134 (2024).
227. Kaufman, L. & Bernstein, H. Computer calculation of phase diagrams with special reference to refractory metals (1970).
228. Chang, Y. A. et al. Phase diagram calculation: past, present and future. *Prog. Mater. Sci.* **49**, 313–345 (2004).
229. Zhang, C., Zhang, F., Chen, S. & Cao, W. Computational thermodynamics aided high-entropy alloy design. *JOM* **64**, 839–845 (2012).
230. Software, T.-C. High entropy alloys database. https://thermocalc.com/products/databases/high-entropy-alloys/ (2025).
231. Computherm. Panhea https://computherm.com/panhea (2025).
232. Chen, H.-L., Mao, H. & Chen, Q. Database development and Calphad calculations for high entropy alloys: challenges, strategies, and tips. *Mater. Chem. Phys.* **210**, 279–290 (2018).
233. Shi, R. & Luo, A. A. Applications of calphad modeling and databases in advanced lightweight metallic materials. *Calphad* **62**, 1–17 (2018).
234. Anamu, U. et al. Fundamental design strategies for advancing the development of high entropy alloys for thermo-mechanical application: a critical review. *J. Mater. Res. Technol.* **27**, 4833–4860 (2023).
235. Carrion Ständer, S., Barschkett, N. & Kabliman, E. Carousel: an open-source framework for high-throughput microstructure simulations. *Integrating Mater. Manuf. Innov.* **12**, 289–300 (2023).
236. de Araujo Santana, D. et al. High-throughput strategy to design high entropy alloys with an fcc matrix, l12 precipitates, and optimized yield stress. *Mater. Des.* **244**, 113173 (2024).
237. Talluri, G., Murty, B. & Maurya, R. The eutectic compositional space in Al-Cr-Fe-Ni system utilizing the high-throughput CALPHAD approach. *Scr. Mater.* **249**, 116178 (2024).
238. Zhu, S., Sarítürk, D. & Arróyave, R. Accelerating Calphad-based phase diagram predictions in complex alloys using universal machine learning potentials: opportunities and challenges. *Acta Mater.* **286**, 120747 (2025).
239. Li, K. et al. Exploring NiCrAlYSiTa multicomponent coatings: combining high-throughput synthesis and CALPHAD modeling. *Scr. Mater.* **242**, 115964 (2024).
240. Salloom, R., Baskes, M. I. & Srinivasan, S. G. Atomic level simulations of the phase stability and stacking fault energy of FeCoCrMnSi high entropy alloy. *Model. Simul. Mater. Sci. Eng.* **30**, 075002 (2022).
241. Meesa, M., Gupta, K. & Mangipudi, K. R. A molecular dynamics study of the influence of nucleation conditions on the phase selection in Fe50Mn30Cr10Co10 high entropy alloy. *Materialia* **20**, 101258 (2021).
242. Achmad, T. L., Wibowo, P. A. & Sukma, F. T. Design of high entropy superalloy fenicrcoal using molecular dynamics, computational thermodynamics, and machine learning. *J. Alloy. Compd.* **1010**, 177514 (2025).
243. Roy, A., Singh, P., Balasubramanian, G. & Johnson, D. D. Vacancy formation energies and migration barriers in multi-principal element alloys. *Acta Mater.* **226**, 117611 (2022).
244. Honarmandi, P., Duong, T. C., Ghoreishi, S. F., Allaire, D. & Arroyave, R. Bayesian uncertainty quantification and information fusion in CALPHAD-based thermodynamic modeling. *Acta Mater.* **164**, 636–647 (2019).
245. Honarmandi, P., Paulson, N. H., Arróyave, R. & Stan, M. Uncertainty quantification and propagation in CALPHAD modeling. *Model. Simul. Mater. Sci. Eng.* **27**, 034003 (2019).
246. Debski, R., Gasior, W., Gierlotka, W. & Debski, A. Uncertainty-aware design of high-entropy alloys via ensemble thermodynamic modeling and search space pruning. *Appl. Sci.* **15**, 8991 (2025).
247. Wertz, K. N., Miller, J. D. & Senkov, O. N. Toward multi-principal component alloy discovery: assessment of CALPHAD thermodynamic databases for prediction of novel ternary alloy systems. *J. Mater. Res.* **33**, 3204–3217 (2018).
248. Debski, R., Gasior, W., Gierlotka, W. & Debski, A. Uncertainty-aware prediction of mixing enthalpy in binary alloys with symmetry-augmented embeddings. *Symmetry* **17**, 1282 (2025).
249. Zhang, C. & Gao, M. C. CALPHAD modeling of high-entropy alloys. In *High-Entropy Alloys: Fundamentals and Applications* (eds Gao, M. C., Yeh, J.-W., Liaw, P. K. & Zhang, Y.) 399–444 (Springer, 2016).
250. Spitaler, T. & Romaner, L. Assessed uncertainty in the Ti-W phase diagram combining experimental and ab-initio data. *Calphad* **91**, 102872 (2025).
251. Gao, W., Miles, P. R., Smith, R. C. & Oates, W. S. The maximum entropy method for data fusion and uncertainty quantification in multifunctional materials and structures. *J. Intell. Mater. Syst. Struct.* **33**, 1182–1197 (2022).
252. Zhu, S., Sarítürk, D. & Arróyave, R. Machine learning potentials for alloys: a detailed workflow to predict phase diagrams and benchmark accuracy. *npj Comput. Mater.* **11**, 340 (2025).
253. Sulley, G. A., Raush, J., Montemore, M. M. & Hamm, J. Accelerating high-entropy alloy discovery: efficient exploration via active learning. *Scr. Mater.* **249**, 116180 (2024).
254. Sundar, A., Tan, X., Hu, S. & Gao, M. C. Calphad-based bayesian optimization to accelerate alloy discovery for high-temperature applications. *J. Mater. Res.* **40**, 112–122 (2025).
255. Hastings, T. et al. Accelerated multi-objective alloy discovery through efficient Bayesian methods: application to the fcc high entropy alloy space. *Acta Mater.* **297**, 121173 (2025).
256. Shen, C. The synergy of machine learning and CALPHAD: revitalizing traditional approaches. *Comput. Mater. Sci.* **258**, 113970 (2025).
257. Khatamsaz, D., Attari, V. & Arróyave, R. Microstructure-aware Bayesian materials design. *Acta Mater.* **303**, 121587 (2025).
258. Muhammad, A., Iorio, L., Quadrini, F., Chiavazzo, E. & Fasano, M. Molecular dynamics analysis of plastic crystals as solid-solid phase-change materials for thermal energy storage. *J. Energy Storage* **125**, 116978 (2025).
259. Muhammad, A. et al. From nanoscale to printed products: multiscale modeling and experimental characterization of graphene-enhanced

polylactic acid composites for 3d printing. *Compos. Part B: Eng.* **298**, 112354 (2025).
260. Kukshal, V., Patnaik, A. & Bhat, I. Corrosion and thermal behaviour of AlCr1.5CuFeNi2Tix high-entropy alloys. *Mater. Today. Proc.* **5**, 17073–17079 (2018).
261. Fan, Z., Wang, H., Wu, Y., Liu, X. & Lu, Z. Thermoelectric high-entropy alloys with low lattice thermal conductivity. *Rsc Adv.* **6**, 52164–52170 (2016).
262. Liu, F., Liu, Y., Jiang, X. Z. & Xia, J. Exploring thermophysical properties of CoCrFeNiCu high entropy alloy via molecular dynamics simulations. *Heliyon* **10**, e36064 (2024).
263. Caro, M., Béland, L. K., Samolyuk, G. D., Stoller, R. E. & Caro, A. Lattice thermal conductivity of multi-component alloys. *J. Alloy. Compd.* **648**, 408–413 (2015).
264. Cheng, C., Ma, S. & Wang, S. The role of phonon anharmonicity on the structural stability and phonon heat transport of $CrFeCoNiCu_x$ high-entropy alloys at finite temperatures. *J. Alloy. Compd.* **935**, 168003 (2023).
265. Mu, S., Pei, Z., Liu, X. & Stocks, G. M. Electronic transport and phonon properties of maximally disordered alloys: from binaries to high-entropy alloys. *J. Mater. Res.* **33**, 2857–2880 (2018).
266. Ma, R. et al. Machine learning-assisted exploration of thermally conductive polymers based on high-throughput molecular dynamics simulations. *Mater. Today Phys.* **28**, 100850 (2022).
267. Vasilev, A., Lorenz, T. & Breitkopf, C. Prediction of thermal conductivities of rubbers by MD simulations-new insights. *Polymers* **14**, 2046 (2022).
268. Babaei, H., Keblinski, P. & Khodadadi, J. M. Equilibrium molecular dynamics determination of thermal conductivity for multi-component systems. *J. Appl. Phys.* **112**, 054310 (2012).
269. Dong, H. et al. Interpretation of apparent thermal conductivity in finite systems from equilibrium molecular dynamics simulations. *Phys. Rev. B* **103**, 035417 (2021).
270. Muraleedharan, M. G., Sundaram, D. S., Henry, A. & Yang, V. Thermal conductivity calculation of nano-suspensions using Green–Kubo relations with reduced artificial correlations. *J. Phys. Condens. Matter* **29**, 155302 (2017).
271. Dong, H., Fan, Z., Shi, L., Harju, A. & Ala-Nissila, T. Equivalence of the equilibrium and the nonequilibrium molecular dynamics methods for thermal conductivity calculations: from bulk to nanowire silicon. *Phys. Rev. B* **97**, 094305 (2018).
272. Gu, X., Fan, Z. & Bao, H. Thermal conductivity prediction by atomistic simulation methods: recent advances and detailed comparison. *J. Appl. Phys.* **130**, 210902 (2021).
273. Khadem, M. H. & Wemhoff, A. P. Comparison of Green–Kubo and nemd heat flux formulations for thermal conductivity prediction using the Tersoff potential. *Comput. Mater. Sci.* **69**, 428–434 (2013).
274. McGaughey, A. J. & Kaviany, M. Phonon transport in molecular dynamics simulations: formulation and thermal conductivity prediction. *Adv. Heat. Transf.* **39**, 169–255 (2006).
275. Dongre, B., Wang, T. & Madsen, G. K. Comparison of the Green–Kubo and homogeneous non-equilibrium molecular dynamics methods for calculating thermal conductivity. *Model. Simul. Mater. Sci. Eng.* **25**, 054001 (2017).
276. Bernardi, S., Todd, B. & Searles, D. J. Thermostating highly confined fluids. *J. Chem. Phys.* **132**, 244706 (2010).
277. Braun, E., Moosavi, S. M. & Smit, B. Anomalous effects of velocity rescaling algorithms: the flying ice cube effect revisited. *J. Chem. theory Comput.* **14**, 5262–5272 (2018).
278. Akiner, T., Kocer, E., Mason, J. K. & Erturk, H. Green–Kubo assessments of thermal transport in nanocolloids based on interfacial effects. *Mater. Today Commun.* **20**, 100533 (2019).
279. Iida, S. & Tomoshi, K. Free energy and kinetic rate calculation via non-equilibrium molecular simulation: application to biomolecules. *Biophys. Rev.* **14**, 1303–1314 (2022).
280. Arkundato, A., Syarifah, R. D., Rohman, L., Maulina, W. et al. Thermal conductivity of liquid lead for the fast nuclear reactor coolant, calculated by the Green-Kubo method using molecular dynamics simulation. *J. Penelit. Pendidik. IPA* **9**, 10776–10782 (2023).
281. Chen, J., Zhang, G. & Li, B. How to improve the accuracy of equilibrium molecular dynamics for computation of thermal conductivity? *Phys. Lett. A* **374**, 2392–2396 (2010).
282. Stevens, R. J., Zhigilei, L. V. & Norris, P. M. Effects of temperature and disorder on thermal boundary conductance at solid–solid interfaces: nonequilibrium molecular dynamics simulations. *Int. J. Heat. Mass Transf.* **50**, 3977–3989 (2007).
283. Fan, Z. et al. Force and heat current formulas for many-body potentials in molecular dynamics simulations with applications to thermal conductivity calculations. *Phys. Rev. B* **92**, 094301 (2015).
284. Sellan, D. P., Landry, E. S., Turney, J. E., McGaughey, A. J. H. & Amon, C. H. Size effects in molecular dynamics thermal conductivity predictions. *Phys. Rev. B* **81**, 214305 (2010).
285. Schelling, P. K., Phillpot, S. R. & Keblinski, P. Comparison of atomic-level simulation methods for computing thermal conductivity. *Phys. Rev. B* **65**, 144306 (2002).
286. Müller-Plathe, F. A simple nonequilibrium molecular dynamics method for calculating the thermal conductivity. *J. Chem. Phys.* **106**, 6082–6085 (1997).
287. Ikeshoji, T. & Hafskjold, B. Non-equilibrium molecular dynamics calculation of heat conduction in liquid and through liquid-gas interface. *Mol. Phys.* **81**, 251–261 (1994).
288. Green, M. S. Markoff random processes and the statistical mechanics of time-dependent phenomena. ii. Irreversible processes in fluids. *J. Chem. Phys.* **22**, 398–413 (1954).
289. Kubo, R. Statistical-mechanical theory of irreversible processes. i. General theory and simple applications to magnetic and conduction problems. *J. Phys. Soc. Jpn.* **12**, 570–586 (1957).
290. Ferreira de Souza, N., Mercier Franco, L. F. & Coasne, B. Consistency of equilibrium and nonequilibrium molecular dynamics to assess thermal conductivity. *J. Chem. Eng. Data* **71**, 1022–1032 (2026).
291. Wang, Z. & Ruan, X. On the domain size effect of thermal conductivities from equilibrium and nonequilibrium molecular dynamics simulations. *J. Appl. Phys.* **121**, 044301 (2017).
292. Nejatolahi, M., Golneshan, A. A., Kamali, R. & Sabbaghi, S. Nonequilibrium versus equilibrium molecular dynamics for calculating the thermal conductivity of nanofluids. *J. Therm. Anal. Calorim.* **144**, 1467–1481 (2021).
293. Merabia, S. & Termentzidis, K. Thermal conductance at the interface between crystals using equilibrium and nonequilibrium molecular dynamics. *Phys. Rev. B* **86**, 094303 (2012).
294. Seyf, H. R. et al. Rethinking phonons: the issue of disorder. *npj Comput. Mater.* **3**, 49 (2017).
295. Lory, P.-F. et al. Impact of structural complexity and disorder on lattice dynamics and thermal conductivity in the o-$Al_{13}Co_4$ phase. *Phys. Rev. B* **102**, 024303 (2020).
296. Zhang, Y., Osetsky, Y. N. & Weber, W. J. Tunable chemical disorder in concentrated alloys: defect physics and radiation performance. *Chem. Rev.* **122**, 789–829 (2021).
297. Zhang, Y. et al. Influence of chemical disorder on energy dissipation and defect evolution in advanced alloys. *J. Mater. Res.* **31**, 2363–2375 (2016).
298. Sun, Z., Shi, C., Gao, L., Lin, S. & Li, W. Thermal physical properties of high entropy alloy $Al_{0.3}CoCrFeNi$ at elevated temperatures. *J. Alloy. Compd.* **901**, 163554 (2022).
299. Al Hasan, M. A. et al. Effects of aluminum content on thermoelectric performance of AlxCoCrFeNi high-entropy alloys. *J. Alloy. Compd.* **883**, 160811 (2021).
300. Wang, H. et al. Exceptionally low thermal conductivity in distorted high entropy alloy. *Mater. Res. Lett.* **13**, 24–34 (2025).

301. Körmann, F., Ikeda, Y., Grabowski, B. & Sluiter, M. H. Phonon broadening in high entropy alloys. *npj Comput. Mater.* **3**, 36 (2017).
302. Sood, A. et al. Direct visualization of thermal conductivity suppression due to enhanced phonon scattering near individual grain boundaries. *Nano Lett.* **18**, 3466–3472 (2018).
303. Lund, F. & Scheihing-Hitschfeld, B. The scattering of phonons by infinitely long quantum dislocations segments and the generation of thermal transport anisotropy in a solid threaded by many parallel dislocations. *Nanomaterials* **10**, 1711 (2020).
304. Gurunathan, R., Hanus, R., Dylla, M., Katre, A. & Snyder, G. J. Analytical models of phonon–point-defect scattering. *Phys. Rev. Appl.* **13**, 034011 (2020).
305. Lim, M. et al. Influence of mass and charge disorder on the phonon thermal conductivity of entropy stabilized oxides determined by molecular dynamics simulations. *J. Appl. Phys.* **125**, 055105 (2019).
306. Orhan, O. K., Hendy, M. & Ponga, M. Electronic effects on the radiation damage in high-entropy alloys. *Acta Mater.* **244**, 118511 (2023).
307. Turner, S. R. et al. Phonon behavior in a random solid solution: a lattice dynamics study on the high-entropy alloy fecocrmnni. *Nat. Commun.* **13**, 7509 (2022).
308. Mora-Barzaga, G., Urbassek, H. M., Deluigi, O. R., Pasinetti, P. M. & Bringa, E. M. Chemical short-range order increases the phonon heat conductivity in a refractory high-entropy alloy. *Sci. Rep.* **14**, 20628 (2024).
309. Lee, J. I., Oh, H. S. & Park, E. S. Manipulation of $\sigma y/\kappa$ ratio in single phase fcc solid-solutions. *Appl. Phys. Lett.* **109**, 061906 (2016).
310. Singh, P. et al. Alloying effects on the transport properties of refractory high-entropy alloys. *Acta Mater.* **276**, 120032 (2024).
311. Zhang, J., Zhang, H., Xiong, J., Chen, S. & Zhang, G. Tuning lattice thermal conductivity in NbMoTaW refractory high-entropy alloys: insights from molecular dynamics using machine learning potential. *J. Appl. Phys.* **136**, 155106 (2024).
312. Zhang, J. et al. Anomalous component-dependent lattice thermal conductivity in MoWTaTiZr refractory high-entropy alloys. *Iscience* **28**, 112100 (2025).
313. Wang, R. et al. Molecular dynamics simulation of effects of Al on the evolution of displacement cascades in AlxCoCrFeNi high entropy alloys. *J. Nucl. Mater.* **577**, 154342 (2023).
314. Abs da Cruz, C., Katcho, N. A., Mingo, N. & Veiga, R. G. Thermal conductivity of nanocrystalline sige alloys using molecular dynamics simulations. *J. Appl. Phys.* **114**, (2013).
315. Kirkwood, J. G. & Buff, F. P. The statistical mechanical theory of surface tension. *J. Chem. Phys.* **17**, 338–343 (1949).
316. Leroy, F. & Müller-Plathe, F. Dry-surface simulation method for the determination of the work of adhesion of solid-liquid interfaces. *Langmuir* **31**, 8335–8345 (2015).
317. Leroy, F., Liu, S. & Zhang, J. Parametrizing nonbonded interactions from wetting experiments via the work of adhesion: example of water on graphene surfaces. *J. Phys. Chem. C.* **119**, 28470–28481 (2015).
318. Berendsen, H. J. C. *Simulating the Physical World: Hierarchical Modeling from Quantum Mechanics to Fluid Dynamics* (Cambridge University Press, 2007).
319. Daivis, P. J. & Evans, D. J. Comparison of constant pressure and constant volume nonequilibrium simulations of sheared model decane. *J. Chem. Phys.* **100**, 541–547 (1994).
320. Galliéro, G., Boned, C. & Baylaucq, A. Molecular dynamics study of the lennard-jones fluid viscosity: application to real fluids. *Ind. Eng. Chem. Res.* **44**, 6963–6972 (2005).
321. Zhang, Y., Otani, A. & Maginn, E. J. Reliable viscosity calculation from equilibrium molecular dynamics simulations: a time decomposition method. *J. Chem. Theory Comput.* **11**, 3537–3546 https://doi.org/10.1021/acs.jctc.5b00351 (2015).
322. Hess, B. Determining the shear viscosity of model liquids from molecular dynamics simulations. *J. Chem. Phys.* **116**, 209–217 (2002).
323. Bocquet, L. & Barrat, J.-L. On the Green-Kubo relationship for the liquid-solid friction coefficient. *J. Chem. Phys.* **139**, 044704 (2013).
324. Herrero, C., Omori, T., Yamaguchi, Y. & Joly, L. Shear force measurement of the hydrodynamic wall position in molecular dynamics. *J. Chem. Phys.* **151**, 041103 (2019).
325. Cox, R. G. The dynamics of the spreading of liquids on a solid surface. Part 1. Viscous flow. *J. Fluid Mech.* **168**, 169–194 (1986).
326. Ren, W. & E, W. Boundary conditions for the moving contact line problem. *Phys. Fluids* **19**, 022101 (2007).
327. Benhassine, M., Saiz, E., Tomsia, A. P. & De Coninck, J. Nonreactive spreading at high-temperature revisited for metal systems via molecular dynamics. *Langmuir* **25**, 11450–11458 (2009).
328. Fernández-Toledano, J. C., Blake, T. D., De Coninck, J. & Kanduc, M. Hidden microscopic life of the moving contact line of a waterlike liquid. *Phys. Rev. Fluids* **5**, 104004 (2020).
329. Wynblatt, P. & Chatain, D. Modeling grain boundary and surface segregation in multicomponent high-entropy alloys. *Phys. Rev. Mater.* **3**, 054004 (2019).
330. Ferrari, A. & Körmann, F. Surface segregation in Cr-Mn-Fe-Co-Ni high entropy alloys. *Appl. Surf. Sci.* **533**, 147471 (2020).
331. Li, L., Kamachali, R. D., Li, Z. & Zhang, Z. Grain boundary energy effect on grain boundary segregation in an equiatomic high-entropy alloy. *Phys. Rev. Mater.* **4**, 053603 (2020).
332. Swartz, E. T. & Pohl, R. O. Thermal boundary resistance. *Rev. Mod. Phys.* **61**, 605–668 (1989).
333. Tarulli, F. et al. Role of surface oxidation in enhancing heat transfer across graphene–water interface via thermal boundary resistance modulation. *Int. Commun. Heat. Mass Transf.* **172**, 110364 (2026).
334. Stanley, C. Thermal boundary resistance: a review of molecular dynamics simulations and other computational methods. *Phys. Status Solidi* **260**, 2300095 (2023).
335. Jabbari, F., Rajabpour, A., Saedodin, S. & Wongwises, S. Effect of water/carbon interaction strength on interfacial thermal resistance and the surrounding molecular nanolayer of CNT and graphene flake. *J. Mol. Liq.* **282**, 197–204 (2019).
336. Sun, Z. H. et al. Tensile mechanical properties of CoCrFeNiTiAl high entropy alloy via molecular dynamics simulations. *Intermetallics* **142**, 107444 (2022).
337. Liu, J. Molecular dynamic study of temperature dependence of mechanical properties and plastic inception of CoCrCuFeNi high-entropy alloy. *Phys. Lett. A* **384**, 126516 (2020).
338. Chen, L. et al. Exploration of V–Cr–Fe–Co–Ni high-entropy alloys with high yield strength: a combination of machine learning and molecular dynamics simulation. *Comput. Mater. Sci.* **217**, 111888 (2023).
339. Wang, Q., Guo, J., Chen, W. & Tian, Y. Molecular dynamics simulations of tensile properties for FeNiCrCoCu high-entropy alloy. *Mater. Today Commun.* **38**, 108187 (2024).
340. Cao, Y., Liu, J., Zhou, S. & Xu, Y. Mechanical properties and microstructural evolution of $FeNiCrCoCu_x$ high-entropy alloys: a molecular dynamics simulation. *Solid State Commun.* **359**, 115011 (2023).
341. Nettey-Oppong, E. E., Mensah, E. E., Effah, E., Asare, E. & Nartey, M. A. Mechanical properties and deformation behavior of equiatomic CoCrFeMnNi high-entropy alloy foam: a molecular dynamics study. *Solid State Commun.* **371**, 115236 (2023).
342. Ya-zhou, L. et al. Molecular dynamics simulation of phase transition and crack propagation in metastable high entropy alloy. *Mater. Today Commun.* **33**, 104642 (2022).
343. Liu, P., Xiang, H., Li, H. & Peng, X. Enhancement mechanism of fracture-resistance of CrMnFeCoNi high-entropy alloys: a molecular dynamics study. *Adv. Powder Technol.* **33**, 103603 (2022).
344. Baruah, S. K., Chatterjee, S., Acharya, A. & Wang, G. J. Averaging molecular dynamics simulations to study the slow-strain rate

behavior of metals. Preprint at https://arxiv.org/abs/2603.07321 (2026).
345. Mayahi, R. An investigation concerning generalized stacking fault behavior of $AlCo_xCrFeNi$ ($0.25 \leq x \leq 2$) high entropy alloys: insights from first-principles study. *J. Alloy. Compd.* **818**, 152928 https://doi.org/10.1016/j.jallcom.2019.152928 (2020).
346. Kudrnovsky`, J., Drchal, V., Máca, F., Turek, I. & Khmelevskyi, S. Electron transport in high-entropy alloys: $Al_xCrFeCoNi$ as a case study. *Phys. Rev. B* **100**, 014441 (2019).
347. Mu, S. et al. Uncovering electron scattering mechanisms in NiFeCoCrMn derived concentrated solid solution and high entropy alloys. *npj Comput. Mater.* **5**, 1 (2019).
348. Zuo, T. et al. Tailoring magnetic behavior of CoFeMnNiX (X = Al, Cr, Ga, and Sn) high entropy alloys by metal doping. *Acta Mater.* **130**, 10–18 (2017).
349. Wei, P. et al. Understanding magnetic behaviors of $FeCoNiSi_{0.2}M_{0.2}$ (M = Cr, Mn) high entropy alloys via first-principle calculation. *J. Magn. Magn. Mater.* **519**, 167432 (2021).
350. Senkov, O., Wilks, G., Miracle, D., Chuang, C. & Liaw, P. Refractory high-entropy alloys. *Intermetallics* **18**, 1758–1765 (2010).
351. Gorr, B. et al. Microstructure evolution in a new refractory high-entropy alloy W-Mo-Cr-Ti-Al. *Metall. Mater. Trans. A* **47**, 961–970 https://doi.org/10.1007/s11661-015-3246-0 (2016).
352. Gubaev, K. et al. Finite-temperature interplay of structural stability, chemical complexity, and elastic properties of bcc multicomponent alloys from ab initio trained machine-learning potentials. *Phys. Rev. Mater.* **5**, 073801 https://doi.org/10.1103/PhysRevMaterials.5.073801 (2021).
353. Gubaev, K. et al. Performance of two complementary machine-learned potentials in modelling chemically complex systems. *npj Comput. Mater.* **9**, 129 https://doi.org/10.1038/s41524-023-01073-w (2023).
354. Maxson, T., Soyemi, A., Zhang, X., Chen, B. W. J. & Szilvási, T. Ms25: materials science-focused benchmark data set for machine learning interatomic potentials. *J. Chem. Inf. Model.* **65**, 8097–8112 https://doi.org/10.1021/acs.jcim.5c01262 (2025).
355. Wang, H., Zhang, L., Han, J. & E, W. Deepmd-kit: a deep learning package for many-body potential energy representation and molecular dynamics. *Comput. Phys. Commun.* **228**, 178–184 (2018).
356. Gurrutxaga-Lerma, B. & Arnold, J. E. Predictive dislocation mobility in high-entropy alloys without driven molecular dynamics: a quantum statistical approach. *Phys. Rev. B* **114**, 034116 (2026).
357. Kuehmann, C. J. & Olson, G. B. Computational materials design and engineering. *Mater. Sci. Technol.* **25**, 472–478 https://doi.org/10.1179/174328408X371967 (2009).
358. Haase, C., Tang, F., Wilms, M. B., Weisheit, A. & Hallstedt, B. Combining thermodynamic modeling and 3d printing of elemental powder blends for high-throughput investigation of high-entropy alloys - towards rapid alloy screening and design. *Mater. Sci. Eng. A* **688**, 180–189 (2017).
359. Lu, P. et al. Computational materials design of a corrosion resistant high entropy alloy for harsh environments. *Scr. Mater.* **153**, 19–22 (2018).
360. Pei, Z., Yin, J., Liaw, P. K. & Raabe, D. Toward the design of ultrahigh-entropy alloys via mining six million texts. *Nat. Commun.* **14**, 54 https://doi.org/10.1038/s41467-022-35766-5 (2023).
361. Vela, B., Khatamsaz, D., Acemi, C., Karaman, I. & Arróyave, R. Data-augmented modeling for yield strength of refractory high entropy alloys: a bayesian approach. *Acta Mater.* **261**, 119351 (2023).
362. Villanueva, W., Boettinger, W., McFadden, G. & Warren, J. A diffuse-interface model of reactive wetting with intermetallic formation. *Acta Mater.* **60**, 3799–3814 (2012).
363. Villanueva, W., Boettinger, W., Warren, J. & Amberg, G. Effect of phase change and solute diffusion on spreading on a dissolving substrate. *Acta Mater.* **57**, 6022–6036 (2009).
364. Bonny, G., Pasianot, R., Castin, N. & Malerba, L. Ternary Fe-Cu-Ni many-body potential to model reactor pressure vessel steels: first validation by simulated thermal annealing. *Philos. Mag.* **89**, 3531–3546 (2009).
365. Bonny, G., Terentyev, D., Pasianot, R. C., Poncé, S. & Bakaev, A. Interatomic potential to study plasticity in stainless steels: the FeNiCr model alloy. *Model. Simul. Mater. Sci. Eng.* **19**, 085008 https://doi.org/10.1088/0965-0393/19/8/085008 (2011).
366. Varvenne, C., Luque, A., Nöhring, W. G. & Curtin, W. A. Average-atom interatomic potential for random alloys. *Phys. Rev. B* **93**, 104201 (2016).
367. Banerjee, T., Sharma, A., Picak, S., Lattemann, M. & Singh, P. An atomistic study connecting underlying dislocation behavior with superior mechanical properties of NiCoCr medium entropy alloy. *Mater. Today Commun.* **44**, 112065 (2025).
368. Ko, W.-S., Grabowski, B. & Neugebauer, J. Development and application of a Ni-Ti interatomic potential with high predictive accuracy of the martensitic phase transition. *Phys. Rev. B* **92**, 134107 https://doi.org/10.1103/PhysRevB.92.134107 (2015).
369. Kim, Y.-K., Kim, H.-K., Jung, W.-S. & Lee, B.-J. Development and application of Ni-Ti and Ni-Al-Ti 2nn-meam interatomic potentials for Ni-base superalloys. *Comput. Mater. Sci.* **139**, 225–233 (2017).
370. Laplanche, G. et al. Elastic moduli and thermal expansion coefficients of medium-entropy subsystems of the CrMnFeCoNi high-entropy alloy. *J. Alloy. Compd.* **746**, 244–255 (2018).
371. Bag, P., Su, Y.-C., Kuo, Y.-K., Lai, Y.-C. & Wu, S.-K. Physical properties of face-centered cubic structured high-entropy alloys: effects of NiCo, NiFe, and NiCoFe alloying with Mn, Cr, and Pd. *Phys. Rev. Mater.* **5**, 085003 https://doi.org/10.1103/PhysRevMaterials.5.085003 (2021).
372. Zhang, J., Zhang, H., Xiong, J., Chen, S. & Zhang, G. Theoretical insights into the lattice thermal conductivity and thermal expansion of CoNiFe medium-entropy alloys. *Mater. Adv.* **5**, 3998–4005 (2024).
373. Liang, A., Goodelman, D. C., Hodge, A. M., Farkas, D. & Branicio, P. S. $CoFeNiTi_x$ and $CrFeNiTi_x$ high entropy alloy thin films microstructure formation. *Acta Mater.* **257**, 119163 (2023).
374. Farkas, D. & Caro, A. Model interatomic potentials and lattice strain in a high-entropy alloy. *J. Mater. Res.* **33**, 3218–3225 (2018).
375. Farkas, D. & Caro, A. Model interatomic potentials for Fe-Ni-Cr-Co-Al high-entropy alloys. *J. Mater. Res.* **35**, 3031–3040 (2020).
376. Bhattacharjee, P. et al. Microstructure and texture evolution during annealing of equiatomic CoCrFeMnNi high-entropy alloy. *J. Alloy. Compd.* **587**, 544–552 (2014).
377. Choi, W.-M., Jo, Y. H., Sohn, S. S., Lee, S. & Lee, B.-J. Understanding the physical metallurgy of the CoCrFeMnNi high-entropy alloy: an atomistic simulation study. *npj Comput. Mater.* **4**, 1 (2018).

Acknowledgements

The Authors are grateful with Francesco Maria Bellussi and Marina Provenzano for their preliminary literature review.

Author contributions

M.P., M.G.K., F.T., J.E.A., B.G.-L. and D.M. analysed the literature and prepared the first draft of the review. L.B., G.G.F., R.P., B.G.-L. and M.F., together with the other authors, reviewed and finalised the manuscript. M.F. conceptualized and coordinated the review work. All authors have read and approved the final manuscript.

Competing interests

The authors declare no competing interests.

Additional information

Correspondence and requests for materials should be addressed to Gonzalo García Fuentes, Radu Piticescu, Beñat Gurrutxaga-Lerma or Matteo Fasano.

Reprints and permissions information is available at http://www.nature.com/reprints

Publisher's note Springer Nature remains neutral with regard to jurisdictional claims in published maps and institutional affiliations.

Open Access This article is licensed under a Creative Commons Attribution 4.0 International License, which permits use, sharing, adaptation, distribution and reproduction in any medium or format, as long as you give appropriate credit to the original author(s) and the source, provide a link to the Creative Commons licence, and indicate if changes were made. The images or other third party material in this article are included in the article's Creative Commons licence, unless indicated otherwise in a credit line to the material. If material is not included in the article's Creative Commons licence and your intended use is not permitted by statutory regulation or exceeds the permitted use, you will need to obtain permission directly from the copyright holder. To view a copy of this licence, visit http://creativecommons.org/licenses/by/4.0/.

© The Author(s) 2026

This Article in Press is shared early to give you faster access to new research. It is citable and carries a permanent DOI. The final edited version will replace it automatically.